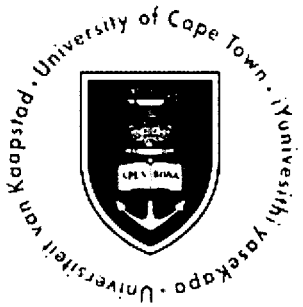

A Comparison of the HI and CO Velocity Dispersions of Nearby Galaxies

Keoikantse Moses Mogotsi

May 2012

A project submitted in partial fulfilment of the requirements for the degree M.Sc. in the Department of Astronomy, as part of the National Astrophysics and Space Science Programme
UNIVERSITY OF CAPE TOWN

Supervisor: Prof. W.J.G. de Blok

Abstract

Velocity dispersions are used to determine the stability of galactic disks against gravitational collapse to form stars, in some star formation recipes, in studies of gas dynamics, and to determine how much turbulence there is in the interstellar medium. Atomic hydrogen (HI) dispersions have been used in the studies of star formation and large-scale turbulence, despite stars forming in molecular clouds and the inner regions of galaxies being dominated by molecular gas. Carbon monoxide (CO) has been used as a tracer for molecular gas. In this work HI and CO dispersions were determined for a sample of nearby galaxies and they were compared to determine what the relationship between HI and molecular gas dispersions is. The dispersions were higher than expected from thermal effects, and HI had on average 1.5 ± 0.18 times greater velocity dispersion than CO, which corresponds to a $7.2 \pm 1.3\,\mathrm{km\,s^{-1}}$ velocity dispersion difference. The HI and CO dispersions and dispersion ratios were found to correlate with star formation at high star formation rate densities $\Sigma_{\mathrm{SFR}} \geq 10^{-2.6}\,\mathrm{M_\odot\,yr^{-1}\,kpc^{-2}}$.

Acknowledgements

I would like to thank my supervisor for all the help and support during my Masters. This work was funded by the South African Research Chair Initiative (SARChI) and the National Astrophysics and Space Science Program, both initiatives funded by the National Research Foundation. I would like to thank the Department of Science and Technology for their support of the Square Kilometer Array and Astrophysics research and studies in the country. I would like to thank F. Walter (and the THINGS collaboration) and A. Leroy (and the HERACLES collaboration) for their success in completing their great surveys and allowing me access to their high quality data. I would also like to thank B. Warren, R. Ianjamasimanana, P. Amram, R. Braun, N. Pereto, G. Angus and L. Staveley-Smith for useful discussions about my thesis work. I would like to thank NASA: the SINGS and GALEX-Nearby Galaxy Survey for making their data public. Lastly, I would like to acknowledge Kosma von Maltitz and Wendy Williams for providing this great latex template.

Plagiarism Declaration

I, Keoikantse Moses Mogotsi, know the meaning of plagiarism and declare that all of the work in the document, save for that which is properly acknowledged, is my own.

Contents

Chapter 1

Introduction

1.1 Radio Observations and Velocity dispersions

The simplest optical observations are photometric observations and they provide intensity, flux and position measurements of astronomical objects/targets. Points of intensity (or other parameter) plotted against spatial position are called pixels. Spectroscopic instruments can be added to measure the flux and wavelength of incoming radiation from emission or absorption lines. Due to the Doppler effect, the wavelength (or frequency) can be used to determine the velocity of the source of these spectral lines. Radio observations provide both flux and frequency information, the frequencies are then converted to velocities. This means no additional instrumentation or observations are required to obtain both the velocity, and spatial intensity of target sources. Points of intensity plotted against spatial position and velocity (or frequency) are sometimes called voxels. Plots of the intensity versus velocity at particular positions are called velocity profiles. The width of the spectral line seen in these velocity profiles can be described by the full width half maximum (FWHM) or the velocity dispersion (σ). The full width half maximum is the width of the spectral line profile at half of the maximum intensity. For a single idealized source of emission whose particles have a Maxwellian velocity distribution, a Gaussian velocity profile can describe the velocity profile of the emission line and the velocity dispersion is the standard deviation of this Gaussian. This is only true if the line is sufficiently optically thin. FWHM and σ are related by $\sigma = \mathrm{FWHM}/2\sqrt{2\ln(2)}$. In this project we use radio observations to study the velocity dispersions of neutral atomic hydrogen (HI) and carbon monoxide (CO) in external galaxies.

1.2 Gas in Galaxies

1.2.1 Atomic Hydrogen

Most of the baryonic material in the universe is in the form of the simplest element in its simplest form: neutral atomic hydrogen (HI). HI is detected in the universe through

its forbidden 21cm hyperfine spin-flip electronic transition, which was predicted by van de Hulst (1945). This transition was first detected by Ewen and Purcel (1951) and confirmed by Muller and Oort (1951). Due to the sheer amount of atomic hydrogen in the universe this line is easily detectable and has been the line of choice for large amounts of work on the atomic gas in the universe. It has been the foundation for studies of the dynamics of galaxies, the interstellar medium and star formation; hence ever-better HI observations of galaxies have been made to try and learn more about these areas of study.

The early observations were done with single dish radio telescopes but technological advances led to the use of interferometry. Interferometers are multiple dish arrays that can be spaced to create large baselines therefore making it possible to reach high resolutions. Technological advances also led to improvements in the sensitivity of detectors. From early galaxy surveys such as Bosma (1981*a*) the benefits of HI were seen, as it extends further out than the stellar components of the galaxies. Due to the nature of the radio observations the velocity information is a part of normal HI observations so the dynamics of the neutral atomic gas can easily be determined. In optical astronomy, additional spectroscopic observations need to be made to determine velocities. The resolution of the early HI observations were still far behind the optical observations; nevertheless dynamics were determined and rotation curves calculated (e.g. Bosma 1981*b*). Better and better instruments were made due to technological advances, and the quality of observed data increased. Many galaxies have been observed in the HI, e.g. Bosma (1981*a*), Brinks and Bajaja (1986), Wevers et al. (1986), Begeman (1987), Cayatte et al. (1990), Puche and Carignan (1991), Braun (1995), Staveley-Smith et al. (1997), Walter and Brinks (1999), Walter and Brinks (2001), Kim et al. (1999), de Blok and Walter (2000), van der Hulst et al. (2001), Verheijen and Sancisi (2002), Walter et al. (2002), Swaters et al. (2002). High spatial resolution HI nearby galaxy observations by Braun et al. (1995), Walter and Brinks (1999), de Blok and Walter (2000), Walter et al. (2008) were made with some of the best modern interferometers: The Very Large Array (VLA) and the Australian Compact Array (ATCA). Observations like those made it possible to study the atomic gas and its dynamics in nearby galaxies at sub-kpc scales (e.g de Blok et al. 2008).

1.2.2 Molecular Gas

Gas densities in interstellar clouds are high enough to prevent ionizing radiation from reaching the interior of the clouds. These conditions are suitable for the formation of molecules in these clouds (Eddington 1937). The high abundance of hydrogen in the universe means that the largest component of molecular gas should be molecular hydrogen (H_2). The presence of H_2 in the interstellar medium was predicted by Eddington (1937), Strömgren (1939) and Gold (1961). The molecule was first detected by Carruthers (1970) by a uv-spectrometer on a rocket. It forms mainly via grain chemistry ($H + H \rightarrow H_2$, with dust as a catalyst), though there are also mechanisms in the gas phase (e.g. $H^{-1} + H \rightarrow H_2 + e$) (Glover 2002).

Many other more complex molecules have been detected in the ISM and they are postulated to form via reactions in either phase.

The formation of molecules is counteracted by photodissociation (dissociation of molecules by photons), predissociation (dissociation of molecules before they reach their final state) (Snow and McCall 2006), and collisional dissociation (dissociation of molecules via collisions with other species) (Shull and Beckwith 1982). The typical wavelength regimes for detecting lines of simple molecules are electronic lines in the ultraviolet and visible, vibrational in the infrared, and rotational lines in the radio and infrared (Snow and McCall 2006).

Molecular gas is found in the dense, cold environments of galaxies and can even dominate over the atomic gas in the inner regions of spiral galaxies. Molecular gas forms clumps/aggregates called giant molecular clouds (GMCs), and inside these is where stars are observed to form. The diameters of molecular clouds in our galaxy range from 10pc-100 pc (Sanders et al. 1985). Molecular gas is a good tracer of regions where thermal pressure is low enough to allow for stars to form (i.e. regions where the temperature is low enough to allow for gravitational collapse) (Krumholz et al. 2011). Since stars and molecular gas are found in the same locations, understanding molecular gas is important to the understanding of how stars form and of the ISM in these dense regions. Molecular hydrogen which forms the largest component of the molecular gas is hard to detect because of the low temperatures of the clouds and its lack of a permanent dipole moment. Its electronic absorption lines occur in the UV (Gould and Saltpeter 1963); its emission lines are very weak and occur from the UV to far infrared (Burton et al. 1992). Its lack of a permanent dipole moment means that its pure vibration-rotational absorption lines are very weak (Gould and Saltpeter 1963). Its rotational lines require excitation temperatures above 1000 K (Burton et al. 1992), and molecular clouds are too cold to reach these excitation temperatures of lines.

Carbon Monoxide (CO, $^{12}C^{16}O$) has been found to be a tracer of H_2 (Lebrun et al. 1983, Bloemen et al. 1984). It has a dipole moment and is much easier to detect than H_2. It was first detected by Smith and Stecher (1971) in the ultraviolet. There are many pathways that are important for the formation of CO, and most of them lead to these reactions :
$C^+ - OH \rightarrow CO^+ + H$;
$CO^+ - H_2 \rightarrow HCO^+ + H$;
then $HCO^+ - e \rightarrow CO + H$ (Snow and McCall 2006). There are believed to be transitions between the domination of C^+, C, and CO which occur in diffuse and translucent molecular clouds (van Dishoeck and Black 1988, Jannuzi et al. 1988, Snow and McCall 2006). The gamma ray flux of molecular clouds was instrumental in determining that CO could trace the molecular gas. It was also used in the early attempts to determine the H_2/CO ratio (e.g. Bloemen et al. 1984, Bloemen et al. 1986, Dame and Thaddeus 1985). Other methods to compare CO and H_2 were to match up the velocities of millimeter CO observations with those found from H_2 absorption line observations (e.g. Knapp and Jura 1976, Kopp et

al. 1996 and Liszt 1997). CO was found to be the easiest molecule to use as a tracer of molecular hydrogen. But it is not a perfect indicator of the presence of H_2; and the relationship between CO and H_2 is not as simple as has been assumed for many analyses over the past few decades. Complications arise because C is not always in the form of CO in molecular clouds (the other common form of C is C^+). CO is not as effective at self-shielding from UV radiation as H_2 is, therefore the transition C^+/CO can occur much deeper into molecular clouds than HI/H_2 transition (Wolfire et al. 2010). Models predict the C^+ layer in and around molecular clouds (van Dishoek and Black 1988, Tielens and Hollenbach 1985*a*, Tielens and Hollenbach 1985*b*, Sternberg and Dalgarno 1995). Gernier et al. (2005) detected a large fraction of "dark" molecular gas (devoid of CO emission) in the Milky Way. From early on it was believed that the CO-to-H_2 conversion factor (X_{CO}) is dependent on metallicity, density and temperature of the molecular clouds (Dickman et al. 1986). Models by Maloney and Black (1988) indicated that the conversion factor is strongly dependent on metallicity. Strong evidence for a correlation between metallicity of the host galaxy and conversion factor was found (e.g. Wilson 1995, who found the correlation in Local Group galaxies). Models by Shetty et al. (2011) have also shown that X_{CO} tends to decrease as CO velocity dispersion increases ($X_{CO} \propto \sigma^{-0.5}$). The fraction of C in the form of C^+ compared to CO in molecular clouds/H_2 gas is strongly dependent on the metallicity, the amount of "dark" molecular gas increases with decreasing metallicity (Wolfire et al. 2010). Therefore low metallicity galaxies will have much lower fractions of CO in H_2 regions than higher metallicity galaxies (Krumholz et al. 2011). But even though it is not a perfect tracer, the presence of CO infers the presence of H_2 and it can still act as a good estimator of the H_2 content of galaxies, especially in normal spirals with average to high metallicities.

There were many early surveys of CO in nearby galaxies (e.g. Rickard et al. 1975, Solomon and Zafra 1975, Solomon and Sage 1988, Young and Knezek 1989, Heckman 1989, Young and Scoville 1991, Sage 1993, Braine et al. 1993, Young et al. 1995). The Five Colleges Radio Astronomy Observatory Extragalactic CO Survey (FCRAO survey, Young et al. 1995), provided a large survey of nearby galaxies in CO emission. The CO(1-0) line (from the J=1-0 rotational transition) was the primary line observed and M_{H_2}/M_{HI} one of the major topics of study. The CO(1-0) distribution was shown to follow that of CO(2-1) in Milky Way studies by Israel et al. (1984) and Sakamoto et al. (1995). Braine et al. (1993) compared the two in 81 galaxy centers, found a (2-1)/(1-0) line ratio of 0.89 ± 0.06 and confirmed that CO(2-1) also traces H_2. Further CO surveys and observations were made by e.g. Casoli et al. (1998), Fukui et al. (1999), Engargiola et al. (2003), Walter et al. (2001), Sakamoto et al. (1999). The Berkeley Illinois Maryland Association Survey of Nearby Galaxies (BIMA SONG, Helfer et al. 2003) was the next major advance in CO observations of nearby galaxies. It mapped CO emission in 44 nearby galaxies at 6" resolution. Major advances in detector technology have allowed higher sensitivity observations. The use of interferometers has led to increased resolutions. The most recently completed nearby galaxy

surveys have been done by Kuno et al. (2007), Leroy et al. (2009) and Wilson et al. (2011); and there are many surveys currently running on interferometers such as CARMA (Combined Array for Research in Millimeter-wave Astronomy) and SMA (SubMillimeter Array) and advanced detectors on single-dish telescopes like JCMT (James Clerk Maxwell Telescope) and the IRAM (Institut de Radioastronomie Millimétrique) 30m Telescope. With the completion of ALMA (Atacama Large Millimetre Array), many new groundbreaking studies will be done.

1.3 Star-Formation

The Star Formation Rate (SFR) in nearby galaxies has been observed to correlate with the total gas density (e.g. Kenney and Young 1988, Kennicutt 1989, Kennicutt 1998), but the relationship is poorly understood (Leroy et al. 2008). A star formation law is meant to relate the star formation rate of a particular region in a galaxy to local conditions in that area. In other words it is used to quantitatively relate the gas to the SFR. Schmidt (1959) proposed that there is a power law relation between the gas volume density and star formation rate. But it is much easier to determine the gas surface density, because the intensity of the HI emission can be used to determine the gas surface density, whereas there is no direct observable that is easily converted to a volume density. The most widely used star formation law is the Schmidt law :

$$\Sigma_{SFR} = A\Sigma_{gas}^{N}, \tag{1.1}$$

which is a simple law that relates the gas surface density Σ_{gas} to star formation surface density Σ_{SFR} (where Σ_{SFR} =SFR per unit area). Kennicutt (1998) was able to show that the law holds over a range of $\sim 10^5$ in gas surface density and $\sim 10^6$ in star formation rate per unit area for normal disk galaxies and starburst galaxies; and found it to be :

$$\Sigma_{SFR} = (2.5\pm0.7) \times 10^{-4}(\frac{\Sigma_{gas}}{1\mathrm{M}_{\odot}\mathrm{pc}^{-2}})^{1.4\pm0.15}\mathrm{M}_{\odot}\mathrm{yr}^{-1}\mathrm{kpc}^{-2}. \tag{1.2}$$

Hα and far-infrared (FIR) fluxes were used to determine the SFR to determine the parameters in this relationship. The SFR can be determined in many ways and there are many different tracers (e.g. the ones commonly used in nearby galaxy studies: Hα, far-ultraviolet (FUV), FIR, 24μm dust emission). The Kennicutt-Schmidt law is an empirical law, and its exact parameters depend on the tracers that are used to determine the SFR as well as the ISM phase used to determine the gas density. There have also been attempts to relate the law to the actual physics of the gas and disk. In one the law can be thought of as the case where the disk free-fall timescale is fixed, assuming the stars form at a timescale equal to the free-fall timescale in the gas disk (Madore 1977, Leroy et al. 2008). More complex laws, incorporating variable disk free-fall times and the pressure of the gas and ISM, also exist. In one case the disk free-fall time depends on hydrostatic equilibrium rather than being fixed

(Leroy et al. 2008). Using work from Krumholz and McKee (2005) and Elmegreen (1989) the star formation efficiency ($SFE \equiv \Sigma_{SFR}/\Sigma_{gas}$) is then :

$$SFE \propto \frac{\Sigma_{gas}}{\sigma_{gas}}(1 + \frac{\Sigma_*}{\Sigma_{gas}} + \frac{\sigma_g}{\sigma_{*,z}}) \tag{1.3}$$

(Leroy et al. 2008), where σ_g,$\sigma_{*,z}$,Σ_{gas},Σ_* are the gas and stellar velocity dispersions and the gas and stellar surface densities respectively. Some forms incorporate the pressure P_h:

$$P_h \approx \frac{\pi}{2} G\Sigma_{gas}(\Sigma_{gas} + \frac{\sigma_g}{\sigma_{*,z}}\Sigma_*) \tag{1.4}$$

(Elmegreen 1989). Some of these more complicated laws require the velocity dispersion of the gas to determine the rate of star formation.

Another aspect of the star formation law is the star formation threshold. It is used to describe how stable gas is against collapse which leads to star formation. Early attempts at determining such thresholds include those by Skillman (1987), who postulated and found evidence (Skillman 1988) that OB star formation in irregular galaxies requires HI surface densities above 10^{21} atoms cm^{-2}. One measure of criticality is the Toomre criterion (Toomre 1964); which for a thin gas disk is $Q_{gas}(R) = \frac{c_s \kappa}{\pi G \Sigma_{gas}}$, where κ is the epicyclic frequency, R the radius, c_s the sound speed and Σ_{gas} the gas surface density. The gas disk is considered unstable against pressure or rotational support when Q <1 (Safronov 1960, Toomre 1964). The epicyclic frequency is defined as $\kappa = 1.41\frac{v(r_{gal})}{r_{gal}}(1 + \frac{d\log(v(r_{gal}))}{d\log(r_{gal})})^{0.5}$,
where $v_{r_{gal}}$ is the rotational velocity at the distance r_{gal} from the center of the galaxy (Kennicutt 1989, Leroy et al. 2008). Most studies use the velocity dispersion (σ) instead of the sound speed (c_s) (Schaye 2004). The two are related as follows: $\sigma = c_s\gamma^{1/2}$, where γ is the adiabatic index and ratio of specific heats (ratio of specific heat at constant pressure to specific heat at constant volume). Normally a value of $\gamma = 5/3$ (specific heat ratio of monatomic gas) is used, but it is not accurate when the gas is mostly molecular and when velocity dispersions are turbulence dominated (Schaye 2004). The form that is most typically used is

$$Q_{gas}(R) = \frac{\sigma_{gas}\kappa}{\pi G \Sigma_{gas}}. \tag{1.5}$$

In his study, Kennicutt (1989) introduced α, which is the ratio of the gas density to critical gas density (Σ_c) : $\alpha = \Sigma_{gas}/\Sigma_c$. Formulations of more general instability parameters combining the gas and stellar components have also been made (e.g. Wang and Silk 1994, Bertin 1996, Rafikov 2001, Leroy et al. 2008, Romeo and Wiegert 2011). A commonly used one is the so-called Wang and Silk approximation :

$$Q_{total}^{-1} \approx Q_{gas}^{-1} + Q_*^{-1}, \tag{1.6}$$

where Q_{gas} and Q_* are the gas and stellar Q parameters (Wang and Silk 1994, Bertin 1996,

Bertin and Lin 1996). Leroy et al. (2008) use

$$Q_* = \frac{\sigma_{*,r}\kappa}{\pi G \Sigma_*} \tag{1.7}$$

as the stability parameter for a collisionless stellar disk. Combined with the gas disk stability parameter they find :

$$\frac{1}{Q_{stars+gas}} = \frac{2}{Q_{stars}}\frac{q}{1+q^2} + \frac{2}{Q_{gas}}R\frac{q}{1+q^2R^2} > 1, \tag{1.8}$$

where $q = \frac{k\sigma_{*,r}}{\kappa}$, k is the instability wavenumber and $R = \sigma_g/\sigma_{*,r}$ (Leroy et al. 2008).

Kennicutt (1989,1998) and Martin and Kennicutt (2001) argued that when the gas disk is unstable against collapse, widespread star formation will occur. However the applicability of the Q parameter to star formation thresholds is still under debate and the approximations for the total stability of the gas disk are being improved (e.g. Romeo and Wiegert 2011). Complex models of the effective Q have been derived and analysed (e.g. Elmegreen 1995, Jog 1996, Shen and Lou 2003). Elmegreen (1999) asked why $Q < 1$ should correspond to star formation in a supersonically turbulent medium that has many processes that can affect star formation. Some observations have failed to show clear correlations between Q_{gas} and star formation (e.g. Thornley and Wilson 1995, Meurer et al. 1996, Ferguson et al. 1998, Wong and Blitz 2002). Wong and Blitz (2002) argued that Q_{gas} is more an indicator of gas fraction rather than an indication of where star formation will occur. Wong and Blitz (2002) suggested that perhaps a better Q parameter (one that properly takes into account the effect of stars and gas) should be used in order to determine instability. This could then be a better indication of where the star formation will occur. However, the Toomre parameter continues to be used as the best measure of the instability.

One other complication is that the velocity dispersion is required to determine the Q parameter. Most studies assume that it is independent of radius (e.g. Kennicutt 1989, Ferguson et al. 1998, Hunter et al. 1998, Martin and Kennicutt 2001, Leroy et al. 2008). Normally the mean HI velocity dispersion is used as the gas dispersion (e.g. Leroy et al. 2008). Values ranging from 6 to 9 $\mathrm{km\,s^{-1}}$ are commonly used (e.g. Kennicutt 1989, Ferguson et al. 1998, Hunter et al. 1998, Martin and Kennicutt 2001, Leroy et al. 2008). But Bigiel et al. (2008) found that there is a clearer relation between the molecular gas surface density and the star formation rate density than in the case for HI. Schruba et al. (2011) confirmed the correlation with the molecular gas. There is a better correlation between SFR and H_2 than HI in the inner molecular-dominated regions of galaxies; after stacking the correlation with H_2 continues into the HI-dominated regime until no more CO can be detected (Schruba et al. 2011). The correlation with HI improves in the outer regions and in the regions where there is no detectable H_2 there is some correlation with HI (Bigiel et al. 2010). But just as the stacking by Schruba et al. (2011) showed, there could be molecular gas (that correlates

with SFR much more than HI does) present in these outer regions that is yet to be detected by current instruments. In the inner parts of galaxies molecular gas dominates over the atomic gas, therefore a better understanding of how HI velocity dispersions are related to the molecular gas dispersions would be important in formulating better star formation laws. It is also important to note that Schruba et al. (2011) found variations in the SFR-to-CO relation among galaxies. They found trends similar to those found by Young et al. (1996), with low-mass, low-metallicity galaxies having higher SFR-to-H_2 ratios than high mass galaxies. Therefore such properties may have an effect on the relationship between HI and CO gas properties.

1.4 Turbulence

Turbulence can be thought of as the stochastic scale-dependent behaviour of spatial correlations between some of the variables that describe flows or fluid motions (McKee and Ostriker 2007). The turbulence of the gas in galaxies is important because the observed velocity dispersions of HI emission lines have greater values than those expected from purely thermal effects (Agertz et al. 2009, e.g. Tamburro et al. 2009). The earliest notions of a turbulent ISM were in the theory by von Weizsäcker (1951). Von Hoerner (1951) found observational evidence that gas in the Orion Nebula was turbulent. The early work on large-scale turbulence was not well received and turbulence was only believed to be important on small scales. Work by Larson (1981) indicated that the ISM, specifically molecular clouds, may be dominated by turbulent/irregular motions. The observed velocity dispersions of molecular clouds were greater than the velocity dispersions due to thermal broadening. He found a power-law correlation between the velocity dispersion (σ) of molecular clouds and their sizes (l) :

$$\sigma \propto l^q, \tag{1.9}$$

with the spectral index $q \sim 0.38$. This coefficient (q) was similar to the Kolmogorov scaling law (Frisch 1995). Low et al. (1984) observed interstellar cirrus with similar complex structure as the clouds seen on earth. Other complex structures were seen in other interstellar regions. This led to turbulence becoming widely accepted as an important process in galactic and extragalactic media. Solomon et al. (1987) used more homogenous data to find $q \sim 0.5$ for GMCs. Passot et al. (1988) determined that this is what is predicted for Burgers turbulence (Burgers 1974, Passot et al. 1988) there. The turbulence velocity spectrum obeys a power law

$$E(k) \propto k^{-\beta_\nu} \tag{1.10}$$

(where $E(k)$ is the turbulence velocity spectrum and k the wavenumber), with $-\beta_\nu$ as the exponent of the power law (Roman-Duval et al. 2011). Kolmogorov turbulence is a form of turbulence turbulence where $\beta_\nu = 5/3$ (Frisch 1995, Roman-Duval et al. 2011), whereas Burgers turbulence is a form of turbulence where $\beta_\nu = 2$ (Burgers 1974, Passot et al. 1988,

Roman-Duval et al. 2011). A lot of work has been done to try and understand the role of turbulence in the ISM and to more accurately model it. Due to the complex nature of the interactions and their supersonic motions - compressibility and intermittency effects are considered in many models. Intermittency is when fluctuations occur sporadically (spatially and temporally) in the turbulent flow (Roman-Duval et al. 2011). Within the Milky Way it has been observed that the same scaling coefficients of turbulence fit molecular gas of different scales and GMCs; and turbulence is driven on large scales within or external to GMCs (McKee and Ostriker 2007).

The causes of turbulence in the interstellar medium (ISM) are not well understood (Burkert 2006). Large scale turbulent motions are believed to be from: stars (supernovae, stellar winds, etc.), galactic rotation, gaseous self-gravity, and fluid instabilities (Elmegreen and Scalo 2004; Mac Low and Klessen 2004). The observed velocity dispersion (σ_{eff}) can be thought to consist of a thermal component (v_t) and a turbulence component (σ_t), with

$$\sigma_{eff}^2 = v_t^2 + \sigma_t^2 \tag{1.11}$$

(Agertz et al. 2008). The velocity dispersion due to turbulence is made up of a radial (σ_r), angular (σ_ϕ) and vertical (σ_z) component; or a planar (σ_{xy}) and vertical component (σ_z). Therefore the components being observed will depend on the inclination of the galaxy. Theory and simulations show that the velocity dispersion is expected to be anisotropic, with $\sigma_r > \sigma_\phi > \sigma_z$ and $\sigma_{xy} \sim 2\sigma_z$ (Agertz et al. 2009). In large-scale galactic turbulence studies only the HI is modelled in its multiphase form (see Agertz et al. 2008; Piontek and Ostriker 2004). Large-scale turbulence simulations of the galaxies were done by groups such as Wada et al. (2002), Dib et al. (2006), Wada and Norman (2007), Hennebelle and Audit (2007) and Agertz et al. (2009) to name a few. Large-scale galactic turbulence studies and simulations all turn to measurements of HI dispersions when constraining models or identifying what the levels of turbulence are in galaxies; in regions where molecular gas would dominate over the atomic the interactions between it and the HI and their impact on the overall turbulence in those regions are not taken into consideration. The gas cooling usually does not reach the sub-100K levels found in molecular gas. Only small scale giant molecular cloud simulations or molecular gas dynamics studies are at the low temperatures where actual molecular gas is predominantly found.

1.5 Velocity Dispersion Observations

Gas dispersions are useful in determining the amount of turbulence, upper limits on the thermal temperature the of gas, the stability of the gaseous disk, the scale height of the gas disk and the opacity of the disk. This makes dispersion observations very important in turbulence, star formation, ISM and gas/disk dynamics studies. Due to HI being the domi-

nant gas/baryonic component of galaxies its velocity dispersion has been used for dynamical studies of galaxies. Since most molecular gas is found in molecular clouds, dispersion studies of the molecular gas have been focused on the dispersions of molecular clouds. Sensitivity and velocity resolution are the main factors that have determined whether good dispersion studies can be conducted.

The McKee and Ostriker (1977) models form the basis for our current understanding of the atomic and ionized gas in the ISM. Atomic hydrogen is considered to exist in two phases: the warm neutral medium is expected to be about 8000 K and the cold neutral medium about $\sim 50 - 100$ K (McKee and Ostriker 1977, Wolfire et al. 2005). In most HI observations it is hard to separate the cold and warm HI components, so both components are treated as a single component. Molecular clouds have temperatures of $\sim 10-50$ K (Snow and McCall 2006). The estimated dispersion due to thermal broadening can be calculated by $\sigma_{thermal} = (k\mathrm{T}/\mathrm{M_{mol}m_H})^{0.5}$, where T is the temperature, M_{mol} is the atomic mass of the molecule/atom in atomic mass units, k is Boltzmann's constant and m_H is the mass of hydrogen. The expected dispersions from thermal broadening are: warm HI: $\sim 8\,\mathrm{km\,s^{-1}}$ (T ~ 8000 K), cold HI: $\sim 0.8\,\mathrm{km\,s^{-1}}$ (T ~ 80 K) and for CO (at T ~ 10 K): $\sim 0.05\,\mathrm{km\,s^{-1}}$.

Observational work by van der Kruit and Shostack (1984) and Murray et al. (1990) found HI velocity dispersions of $6 - 12\,\mathrm{km\,s^{-1}}$. Kamphuis and Sancisi (1993) studied NGC6946 and found dispersions ranging from $13\,\mathrm{km\,s^{-1}}$ (in the inner regions) to $6\,\mathrm{km\,s^{-1}}$ (in the outer regions of the galaxy). Petric and Rupen (2007) performed high resolution and high sensitivity observations of NGC1058 to study the HI velocity dispersions. They found that even though single Gaussian fits were not good fits for the velocity profiles they were still able to track the width of the velocity profiles very well. NGC1058 is ideal for vertical velocity dispersion studies because it is a nearby (10 Mpc, Ferguson et. al. 1998) galaxy, therefore high spatial resolution can be reached. It has a low inclination (4°-11°, Lewis 1987, van der Kruit and Shostak 1984)- so the effects of galactic rotation are minimal. They found velocity dispersions ranging from 4 to $14\,\mathrm{km\,s^{-1}}$ and found that the σ_v (vertical velocity dispersion) values declined with radius. They did not find a strong correlation with star formation.
Tamburro et al. (2009) used high resolution HI data from the THINGS survey by Walter et al. (2008) to study HI velocity dispersions; they found that within $\mathrm{r_{25}}$ (the isophotal radius at which the average surface brightness is $25\,\mathrm{mag\,arcsec^{-2}}$) the velocity dispersions were greater than the thermal value ($\sim 8\,\mathrm{km\,s^{-1}}$) and at $\mathrm{r_{25}}$ were $\sim 10\,\mathrm{km\,s^{-1}}$, dropping to lower values outside that. At the outermost radii the velocity dispersions dropped to $\sim 5 \perp 2\,\mathrm{km\,s^{-1}}$.

The velocity dispersion of the molecular gas is not as well quantified as the atomic. Matters are complicated by the molecular gas congregating in dense molecular clouds; and the gas behaviour within the clouds is generally isolated from the cloud-cloud interactions. When observing entire galaxies, the effects of cloud-cloud dispersions and dispersions of

gas within clouds all affect the observed dispersion. Another factor which occurs at all scales is the effect of photodissociation regions - gas is heated and dissociated due to UV (and sometimes X-ray) radiation, the extra input of energy into the gas could result in a broadening of velocity profiles. At tens of parsec and sub-parsec scales it is only the internal velocity dispersions of the molecular clouds that are measured. When multiple GMCs and giant molecular associations (GMAs) lie within a single resolution element (scales of 200 pc above), then all three components are detectable and contribute to the observed dispersion. But the cloud-cloud dispersion is expected to be the dominant component. Therefore scales are very important when interpreting molecular gas dispersions.

Larson (1981) compiled galactic observations of molecular clouds and found that they had velocity dispersions ranging from 0.3 to 10 $\mathrm{km\,s^{-1}}$; which is greater than the internal dispersion expected for molecular clouds at 10K ($\sigma \approx 0.32$ $\mathrm{km\,s^{-1}}$). The large range and scale-dependence of internal dispersions was confirmed in other works (e.g. Solomon et al. 1987, Wong et al. 2011). Bollatto et al. (2008) also found this for extragalactic clouds; they found a similar range of dispersions as Larson (1981). At larger scales Jog and Ostriker (1988), Gammie et al. (1991) and Thomasson et al. (1991) found average dispersions of 3-7 $\mathrm{km\,s^{-1}}$ from their models. Tasker and Tan (2009) performed complex 3D models with 8 pc resolutions and cooling down to 300K, and they found 10 $\mathrm{km\,s^{-1}}$ dispersions. Stark (1984) found molecular cloud-cloud dispersions of $7.8 \pm 0.6\,\mathrm{km\,s^{-1}}$ for clouds within 3kpc of the Sun, whereas Clemens (1985) found a value of $3\,\mathrm{km\,s^{-1}}$, which was argued by Stark and Brand (1989) to be the internal velocity dispersions. A few measurements of molecular gas velocity dispersions in other galaxies have also been made: e.g M33 was observed in CO($J = 2 - 1$) and found to have $\sigma = 5 \pm 1\,\mathrm{km\,s^{-1}}$ by Wilson and Scoville (1990). Combes and Becquaert (1997) used CO($J = 1 - 0$) and CO($J = 2 - 1$) to study NGC 628 and NGC 3938 and found dispersions of $\sigma = 6\,\mathrm{km\,s^{-1}}$. NGC 6946 was found to have dispersions of $8.9\,\mathrm{km\,s^{-1}}$ in CO($J = 1 - 0$) and $6\,\mathrm{km\,s^{-1}}$ in CO($J = 3 - 2$) by Walsh et al. (2002).

In many previous studies attempts were made at separating the cloud-cloud dispersions and internal cloud velocity dispersions in measured dispersions. The following is the approach used by Wilson et al. (2011), in their attempt to do this. In order to determine the cloud-cloud dispersion one can consider

$$\sigma_{obs}^2 = \sigma_{c-c}^2 + {\sigma_{internal}}^2 \tag{1.12}$$

(Wilson et al. 2011). The mass weighted internal velocity dispersion can be described by:

$$\int m\sigma_{int}^2 dN / \int m dN, \tag{1.13}$$

assuming a cloud mass function of $dN/d, \propto m^{-\alpha}$, where m is the cloud mass, N is the number of clouds and α is the spectral index. Using the relation $M \propto \sigma_{int}^4$ (Henriksen and

Turner 1984), calibration by Solomon et al. (1987) and assuming that $\alpha \neq 2$ the internal velocity dispersion can be described by:

$$\sigma_{int}{}^2 = 0.0224 \frac{2-\alpha}{2.5-\alpha} \frac{M_{high}^{2.5-\alpha} - M_{low}^{2.5-\alpha}}{M_{high}^{2-\alpha} - M_{low}^{2-\alpha}}, \tag{1.14}$$

where M_{high} and M_{low} are the maximum and minimum cloud masses (Wilson et al. 2011). But this relation relies on many assumptions and can only be used to estimate the internal velocity dispersion. The real nature of the different components can be complicated and is not necessarily the same across different molecular clouds. The observed dispersions can however be used as upper limits on the cloud-cloud dispersions, and this avoids having to rely on the above-mentioned assumptions.

Fukui et al. (2009) used the HI and CO($J = 1 - 0$) (from the Second NANTEN CO Survey) observations of the LMC to study how CO and HI are related to each other. They were able to resolve individual clouds and to study the CO dispersions of the molecular clouds and the dispersions of their associated HI clouds. In their selected sample they found $\sigma_{HI} \sim 4\sigma_{CO}$ with a mean CO halfpower linewidth of $4.6\,\mathrm{km\,s^{-1}}$ and a mean HI halfpower linewidth of $14.1\,\mathrm{km\,s^{-1}}$ (Fukui et al. 2009). Wilson et al. (2011) performed a detailed analysis on CO dispersions in 12 nearby galaxies using data from the JCMT Nearby Galaxy Survey. They studied the CO($J = 3 - 2$) line and were able to reach 1σ sensitivities of $\sim 19\,\mathrm{mK}$ and velocity resolutions of $\sim 0.43\,\mathrm{km\,s^{-1}}$. They determine the CO dispersions using the second moment definition : $\sigma_v = \sqrt{\Sigma T(v-\bar{v})^2/\Sigma T}$ (where v is the velocity and T the brightness temperature). They took averages of the measured dispersions in each galaxy with threshold cutoffs to try and remove seemingly high and unphysical dispersions, this was done to prevent biasing of the averages. Observed dispersions ranged from 4.1 to $20\,\mathrm{km\,s^{-1}}$. This is much higher than the expected dispersion from thermal temperatures of $10-30\,\mathrm{K}$ characteristic of molecular gas. The cloud-cloud dispersions were determined using the above formula, and were found to range from $2.7 - 20\,\mathrm{km\,s^{-1}}$. Average CO dispersions were $\sigma \sim 7.1\,\mathrm{km\,s^{-1}}$, and cloud-cloud dispersions $\sigma_{COc-c} \sim 6.1\ \mathrm{km\,s^{-1}}$. They also analysed HI dispersions from the THINGS HI survey by Walter et al. (2008). By using the second moment maps from these they found that $\sigma_{HI} \sim 2\sigma_{CO}$ (Wilson et al. 2011).

Using primarily HI dispersions from the THINGS survey (Walter et al. 2008), Tamburro et al. (2009) determined the kinetic energy of the ISM : $\mathrm{E}_k = \frac{3}{2} m\sigma^2$. They determined the total gas kinetic energy by

$$\mathrm{E_k} = \frac{3}{2}(\Sigma_{\mathrm{HI}}\sigma_{\mathrm{HI}}^2 + \Sigma_{\mathrm{H2}}\sigma_{\mathrm{H2}}^2), \tag{1.15}$$

but primarily consider

$$\mathrm{E_k} = \frac{3}{2}(\Sigma_{\mathrm{HI}}\sigma_{\mathrm{HI}}^2). \tag{1.16}$$

They determined dispersions by using the moment definition :

$$\sigma^2 = \frac{1}{\Sigma_{HI}} \sum (v_i - \bar{v})^2 S_i. \tag{1.17}$$

here E_k is the kinetic energy, Σ_{HI} and Σ_{H2} are the HI and H_2 surface densities, and S_i is the intensity. In some of their galaxies they found that the Gaussian σ was about 2-3 $\mathrm{km\,s^{-1}}$ lower than their second moment values. They found that within $r \lesssim r_{25}$ (radius of active star-formation) the kinetic energy is proportional to the supernova input rate into the ISM (this was also confirmed for cases where CO emission was high and taken into account in the kinetic energy calculations). They therefore concluded that the supernova feedback in high star-formation regions is sufficient to account for the high velocity dispersions in HI and molecular gas. In the outer regions they find $\sigma_{HI} \sim 6\,\mathrm{km\,s^{-1}}$, and find that the star formation rate is too low to account for these dispersions, but magneto-rotational instabilities (MRI) or thermal broadening could account for them (Tamburro et al. 2009).

Therefore accurate studies of HI and CO dispersions, how they relate to each other and star formation will be very important. These studies will enable us to better constrain the HI and CO dispersions in galaxies, determine what the differences between them are and if they depend on the position in the galaxy or any other properties of the galaxies. The studies will help us to understand how much turbulence there is in both ISM constituents. Dispersions are used in determining star formation thresholds; these studies will enable us to relate atomic to molecular gas star formation thresholds. They will also enable us to determine whether star formation and velocity dispersions are correlated.

1.6 Aims

Velocity dispersions are important for determining the kinetic temperature of gas, kinetic energy, level of turbulence, distribution of gas, the stability of the gas disk in galaxies and star formation thresholds. In the inner parts of galaxies where the majority of star formation occurs, there is a high amount of molecular gas and it is the dominant component of the gas dynamics. Yet only HI velocity dispersions have been used to determine the star formation thresholds and disk stability in these regions. No high sensitivity studies of the relations between HI and CO dispersions have been made, and the relations between CO dispersions and star formation has not been extensively studied.

The aim is to determine whether there is a difference between HI and CO velocity dispersions in nearby galaxies, and to study the relationship between dispersions and the star formation rate.

Chapter 2

Data Selection, Reduction and Analaysis

2.1 Procedure

The aim is to study the differences in HI and CO velocity dispersions. Therefore we performed pixel-by-pixel comparisons of the HI and CO velocity dispersions in different galaxies. This was done by fitting velocity profiles to all the voxels in the HI and CO data cubes, the fitted dispersions were then analysed and compared to each other. The average dispersion difference and ratio between HI and CO was determined. Maps were made of the dispersions and they were compared to the star formation rate density and other properties of the galaxies. Radial trends of these were analysed as well. Sixteen galaxies were analysed. They were chosen on the basis that they all have high quality HI and CO data from the surveys described in Sec.2.2 and Sec. 2.3; the galaxies are listed in Tables 2.1 and 2.2. The reduction method is described in Sec.2.4.

2.2 THINGS

The HI Nearby Galaxy Survey (THINGS) (Walter et al. 2008) is a 21 cm HI survey done with the Very Large Array (VLA) (of the National Radio Astronomy Observatory, NRAO). It produced high quality HI observations of 34 nearby galaxies, with high spectral ($\leq 5.2\,\mathrm{km\,s^{-1}}$) and spatial ($\sim 6$") resolution (Walter et al. 2008). The galaxies are a wide variety of spirals, dwarfs and irregulars; some quiescent and some interacting; a range of star formation rates (0.008 to 6.05 $\mathrm{M_\odot\,yr^{-1}}$) and metallicities (7.54 to 9.12 $[12 + \log(\mathrm{O/H})]$). The survey aimed to allow better studies of the ISM, especially with regards to star formation and galactic gas dynamics. The high sensitivity, spatial and velocity resolutions required for these HI extragalactic studies were only possible with the VLA, and a homogenous sensitivity (column density: $\sim 4 \times 10^{19}\,\mathrm{cm^{-2}}$ at 30") was reached for the sample (Walter et al. 2008). A large

part of the sample was drawn from the Spitzer Infrared Nearby Galaxies Survey (SINGS, Kennicut et al. 2003), and part of the sample is also in the GALEX Nearby Galaxy Survey (GALEX-NGS, Bianchi et al.(2003)). This means that multiwavelength studies can be used to perform further analysis on the galaxies and their properties.

The VLA B, C and D array configurations were used to obtain the high $\sim 6"$ angular resolutions and uniform sensitivities. This final resolution is matched with the 24μm SINGS resolutions ($\sim 6"$) , and the GALEX NGS NUV (near ultraviolet) resolution ($\sim 5"$). The galaxies were observed with velocity resolutions of either $5.2\,\mathrm{km\,s^{-1}}$, $2.6\,\mathrm{km\,s^{-1}}$ or $1.3\,\mathrm{km\,s^{-1}}$. This was essential in order to spectrally resolve the HI emission line. Natural weighted and robust weighted data cubes were created for each of the galaxies. Naturally weighted cubes provide the highest surface brightness sensitivity, whereas robust weighted cubes have well behaved synthesized beams at higher resolutions. More details on the data reduction can be found in Walter et al.(2008).

2.3 HERACLES

The Heterodyne Receiver Array CO Line Extragalactic Survey (HERACLES) is a CO emission line survey of 45 nearby spiral, irregular and dwarf galaxies (Leroy et al. 2009). It was done using the multipixel Heterodyne Receiver Array (HERA, Schuster et al. 2004) on the 30m IRAM telescope. This type of receiver array has allowed for more complete studies and inventories of CO in nearby galaxies due to its ability to more efficiently map large portions of the sky compared to the old single-pixel receivers. The CO $J = 2 \rightarrow 1$ rotational transition emission line was mapped at 230 GHz (Leroy et al. 2009). It was the first CO survey to cover large regions of so many nearby galaxies at such high spatial resolution (up to 13") and sensitivity. Its main goals were to allow for the quantification of the relationship between the neutral gas, molecular gas and the star formation (Leroy et al. 2009). Part of the sample is in the THINGS, SINGS and GALEX-NGS surveys; and this was important for achieving goals of studying star formation and the relationship between the atomic and molecular gas.

Unlike previous surveys, the full optical disks of the galaxies were observed and fully sampled. On the fly mapping mode was used and HERA was used with the Wideband Line Multiple Autocorrelator (WILMA) backend attached. This resulted in a high velocity resolution of $2.6\,\mathrm{km\,s^{-1}}$. The data reduction is outlined in Leroy et al.(2009). The $2.6\,\mathrm{km\,s^{-1}}$ resolution was smoothed to $5.2\,\mathrm{s^{-1}}$ (and $10\,\mathrm{km\,s^{-1}}$ in some cases) by Hanning smoothing: this reduced the noise levels in the data cubes.

2.4 Data Reduction Method

The naturally weighted THINGS HI data cubes were used along with the Hanning smoothed HERACLES CO data cubes; these were used because they had the lowest noise (and therefore highest sensitivities).

GIPSY was used for fitting and preparation of the data cubes. The HI cubes were smoothed to 13" so that a pixel-by-pixel comparison could be made to the CO cubes. The THINGS observations used heliocentric velocities, while the HERACLES observations used Local Standard of Rest velocities (LSR). The CO velocities were all adjusted to heliocentric using $V_{hel} = V_{LSR} - V_{correction}$ with $V_{correction} = V_{\odot}\cos(\gamma)$; where $V_{\odot}$ is the relative solar velocity between LSR and heliocentric velocities, and γ is the projection angle between the galaxy and the apex of solar motion. The corrections were determined by using $V_{\odot} = 19.5$ $\mathrm{km\,s^{-1}}$ (toward RA:$17^h\,55^m\,36^s$, Dec:$+29^\circ\,56'\,41''$ J(2000), Delhaye 1965). This correction is only necessary when directly comparing the HI and CO velocity profiles. The dispersions are not affected by this because the correction results in a constant velocity shift.

The CO cubes were reprojected to the same sky projection as the THINGS data using the task REPROJ. The profiles in the HI cubes and the adjusted CO cubes were then fitted using the GIPSY task XGAUFIT. XGAUFIT is a task for fitting velocity profiles of data cubes. The user supplies a data cube, and can then choose the type of function to fit the profiles, the number of components and the spatial or velocity region to fit profiles in. The user has the option to supply initial guesses for the fits and to control the maximum number of iterations for fitting. There are also options to fix certain parameters or to reject parameters below or above chosen values.

Gaussian, up to third-order Gaussian-Hermite (h_3) and up to fourth-order Gaussian-Hermite ($h_3.h_4$) fits were made to HI and CO data velocity profiles. The third-order Gaussian-Hermite (h_3) will from hereon be referred to as Hermite h_3 and fourth-order Gaussian-Hermite ($h_3.h_4$) will from hereon be referred to as Hermite h_4. The additional h_3 and h_4 parameters in the Hermite fits introduce non-zero skewness and kurtosis, which can describe asymmetries and peaks that are more flattened or sharper than that of a standard Gaussian. Hermite h_4 fits had both h_3 and h_4 parameters determined, but here they will be referred to as Hermite h_4 fits.
The h_3 parameter measures asymmetric deviations and is related to the skewness (ξ_1) by: $\xi_1 \approx 4\sqrt{3}h_3$; therefore it only has an effect on the measured mean velocity compared to a normal Gaussian. The dispersions measured from a Hermite h_3 fit are directly comparable and equivalent to those from a Gaussian fit.
The h_4 parameter measures deviations in the breadth or sharpness of the peak and is related to the kurtosis (ξ_2) by: $\xi_2 \approx 3 + 8\sqrt{6}h_4$. It affects the dispersion and amplitude that would be measured by a normal Gaussian, therefore the dispersions measured using Hermite h_4

fits are not quite equivalent to those measured from a Gaussian fit : $\sigma_{h4} \approx \sigma_{gauss}(1+\sqrt{6}h_4)$ (where σ_{gauss} is what the dispersion would be if the function was purely Gaussian).
Intensity weighted mean velocities, dispersions, amplitudes, reduced χ^2 and other parameters were all extracted from the outputs of the fits. The main parameter required for the analysis was the dispersion. The Gaussian fitted velocity dispersion is defined as:

$$\sigma = (\frac{\Sigma_i S_i \times (v - \langle v \rangle)^2}{\Sigma_i S_i}), \tag{2.1}$$

where S is the integrated flux, v the measured velocity and $\langle v \rangle$ the Gaussian-weighted mean velocity. These velocity dispersions are independent of the velocity corrections. The Gaussian velocity dispersions were used in all the analysis (see Chap.4 for further discussion regarding this) but fits using Gaussian Hermite h_3 and Hermite h_3,h_4 were also made to compare with the Gaussian fits and to determine which function is the most appropriate for fitting the velocity profiles and determining their velocity dispersions. Hermite h_3 fits are particularly important to compare with because in the studies of the HI dynamics of the THINGS galaxies (de Blok et al. 2008), they were determined to produce the preferred velocity fields for the THINGS galaxies.

A 3σ noise cutoff was was initially applied to the fitted maximum amplitudes; with the σ values used taken from the THINGS paper (Walter et al. 2008) and HERACLES (Leroy et al. 2009) data release for the Hanning smoothed cubes (A. Leroy, priv. comm.) (see Table 2.1). For some of the galaxies no noise values or velocity resolution values were quoted for the CO data, therefore we calculated them from the Hanning smoothed data cubes. The task STAT was used to determine the noise values over the entire mapped area of each galaxy for every channel. The noise values were then plotted against the channel number and a linear trend was found to exist where the noise increased with decreasing channel number. Channels with signal from the target galaxy were removed (a very stringent approach was used where a large range of channels near the obvious galaxy signal were removed). An example of the result is shown in Figure 2.1. A linear fit was made to the noise values and the extrapolated noise value at the median channel number was used as the noise value of the data cube; this approach was tested using galaxies whose noise was given and the method worked for them as well. Effectively the noise value of the central channel is used as the noise for the galaxies with no quoted CO noise values. The noise values (from Walter et al. 2008 and Leroy et al. 2009 or calculated above) for each of the galaxies are given in Table 2.1.

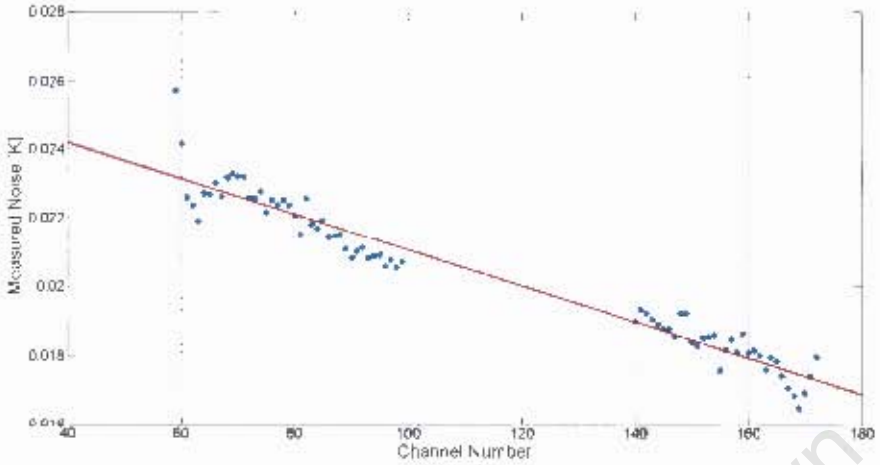

Figure 2.1: Plot of the measured noise in the channels of the NGC 628 CO Hanning-Smoothed data cube, with the red line being a linear fit to the noise

During the fitting it was realised that the 3σ noise cutoff was insufficient for removing the majority of the noise in the cubes. Therefore a 4σ cutoff was used. The observations were also limited by their velocity resolutions. Fitted dispersions that are below the velocity resolution (V_{res}) cannot be trusted as being real. XGAUFIT filtering was used to exclude all fits with dispersions below the velocity resolution of the galaxy. Exceptions were made for NGC 7331 (the CO velocity resolution of the NGC 7331 data is 10 km s $^{-1}$, but a value of 5.2 km s^{-1} was used for the cutoff) and NGC 4214 (the HI velocity resolution was actually 1.3 km s^{-1} but a cutoff of 2.6 km s $^{-1}$ was used). This was done to make the analysis simpler and faster. In the case of NGC 7331 it was to allow us to have more data to work with. The distribution of NGC 7331 dispersions values between $5.2 - 10$ km s^{-1} did not match the distributions we saw in other galaxies below the 5.2 km s^{-1} cut-offs. This indicated that the NGC 7331 dispersions values between $5.2 - 10$ km s $^{-1}$ are not affected by the same velocity resolution problems as the ones below the cut-offs. NGC 4214 did not have any HI dispersions below 5.2km s $^{-1}$ where there was CO emission, therefore our choice of cut-off had no effect on the analysis of this galaxy. Fits were also restricted to have the peak of the profiles to lie within the velocity range covered by the data.

Once the CO and HI data cubes were fitted, the dispersion and dispersion error parameters were extracted from the XGAUFIT output parameters. Maps were made of these, and pixel-by-pixel comparisons were made between the HI and CO dispersions. Dispersion difference maps ($\sigma_{CO} - \sigma_{HI}$) and dispersion ratio ($\sigma_{HI}/\sigma_{CO}$) maps were made for each of the galaxies. This was done by taking each map and subtracting (or dividing) dispersion values of pixels (from different maps) that correspond to the same spatial positions. The 16 galaxies belonging to both surveys were analysed in this way and their noise values and velocity resolutions are listed in Table 2.1. Their other properties that were used in further

Table 2.1: Noise and velocity resolution of the HI and CO cubes of the galaxies analysed. The HI values were taken from Walter et al.(2008).

Name	HI Noise [mJy]/beam	CO Noise [mK]	HI V_{res} [km s^{-1}]	CO V_{res} [km s^{-1}]
NGC 628	0.60	21	2.6	5.2
NGC 925	0.57	16	2.6	5.2
NGC 2403	0.38	19	5.2	5.2
NGC 2841	0.35	16	5.2	5.2
NGC 2903	0.41	21	5.2	5.2
NGC 2976	0.36	20	5.2	5.2
NGC 3077	0.75	17	2.6	5.2
NGC 3184	0.36	17	2.6	5.2
NGC 3198	0.33	17	5.2	5.2
NGC 3351	0.35	19	5.2	5.2
NGC 4214	0.69	19	1.3	5.2
NGC 4736	0.33	21	5.2	5.2
NGC 5055	0.36	26	5.2	5.2
NGC 5194	0.39	18	5.2	5.2
NGC 6946	0.55	25	2.6	5.2
NGC 7331	0.44	13	5.2	10

analysis are shown in Table 2.2, which is drawn from Table 1 in Walter et al.(2008).

Table 2.2: The properties of the galaxies in the sample, taken from Walter et al.(2008)

Name	Distance [Mpc]	Inclination [°]	Position Angle [°]
NGC 628	7.3	7	20
NGC 925	9.2	66	28
NGC 2403	3.2	63	124
NGC 2841	14.1	74	153
NGC 2903	8.9	65	204
NGC 2976	3.6	65	335
NGC 3077	3.8	46	45
NGC 3184	11.1	16	179
NGC 3198	13.8	72	215
NGC 3351	10.1	41	192
NGC 4214	2.9	44	65
NGC 4736	4.7	41	296
NGC 5055	10.1	59	102
NGC 5194	8.0	42	172
NGC 6946	5.9	33	243
NGC 7331	14.7	76	168

Chapter 3

Results : Dispersions and Star Formation

3.1 Dispersions

Pixel by pixel dispersion differences ($\sigma_{CO} - \sigma_{HI}$) and dispersion ratios (σ_{HI}/σ_{CO}) were calculated for each of the galaxies. Analysis was only done for pixels where there is $> 4\sigma$ emission and the dispersion is greater than the velocity resolution in both HI and CO. NGC 7331 has a CO velocity resolution of $10\,\mathrm{km\,s^{-1}}$ but a dispersion cut-off of $5.2\,\mathrm{km\,s^{-1}}$ was applied to its pixels (see Sec 2.4). All the dispersions quoted are Gaussian fitted dispersions unless explicitly stated otherwise (see Chapt.4 for further discussion about this). Examples of the distributions of σ_{CO}, σ_{HI}, $\sigma_{CO} - \sigma_{HI}$ and σ_{HI}/σ_{CO} are shown in Figures 3.1 and 3.2. Figures for all our galaxies are in the Appendix. The dispersions were binned into $1\,\mathrm{km\,s^{-1}}$ bins, and the dispersion ratios into 0.2 sized bins. In these plots the resolution elements were calculated by: Resolution Elements = (Number of Pixels) (Number of Pixels per single Resolution Element). Number of Pixels in a single resolution element was calculated by: $(\pi(\mathrm{Res})^2)$ $((\mathrm{Pixel\ Scale})^2)$; where Res is the resolution (13" in our case) and Pixel Scale is the angular size of each pixel (in arcsec/pixel).

In order to study the spatial distribution of HI and CO dispersion values and to determine whether the differences in dispersion are constant throughout the disks of galaxies, maps were created of the pixel-by-pixel dispersion difference ($\sigma_{CO} - \sigma_{HI}$) and of σ_{HI} and σ_{CO} individually. Examples of these maps are shown in Figures 3.3 and 3.4; maps of the rest of the galaxies can be found in the Appendix. The pixel-by-pixel dispersion ratio (σ_{CO}/σ_{HI}) was also calculated and maps were made (see Figures 3.3 and 3.4 for examples of these and the Appendix) for σ_{CO}/σ_{HI} maps for all the galaxies.

The histograms indicate that HI and CO dispersion distributions peak at certain values (mostly in a unimodal or bimodal form). Inspection by eye indicates that the dispersions

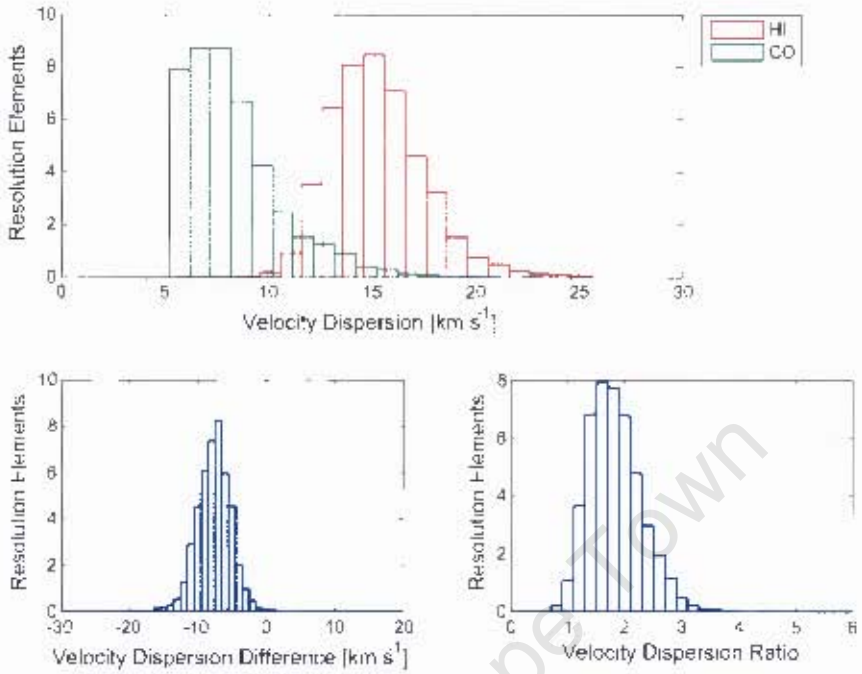

Figure 3.1: (Top) Distributions of the HI and CO dispersions for NGC 3184. Lower left and right figures are histograms of the dispersion difference $\sigma_{CO} - \sigma_{HI}$ and dispersion ratio σ_{HI}/σ_{CO} distributions in NGC 3184.

in many of the galaxies follow Gaussian-like distributions. Figures 3.5 and 3.6 show the distributions of HI and CO dispersions in all the galaxies in our sample. The σ_{CO} plots reveal incomplete (cut-off) distributions, whereas the σ_{HI} distributions are not as affected by the dispersion cut-off. It should be noted that many of the pixels that were removed due to the dispersion cut-off have $> 4\sigma$ emission. Most of the σ_{CO} distribution peaks occur close to the dispersion cut-off (e.g. Figures 3.1 and 3.5), but in a few cases clear σ_{CO} distribution peaks do not seem to occur above the dispersion cut-off (e.g NGC 4736, Figure 3.2 and 3.5). The σ_{HI} distributions however show clear peaks well above the dispersion cut-off and there are very few pixels with dispersions near the dispersion cut-off values (see Figure 3.6). Figure 3.2 shows that the σ_{HI} and σ_{CO} distributions from the same galaxy can be very different. Modes of the dispersion distributions were calculated and are shown in Table 3.1.

Maps of σ_{CO} and σ_{HI} were made to study the molecular and atomic gas dispersions throughout the inner disks of galaxies. Figures 3.3 and 3.4 display the CO and HI dispersion maps of representative galaxies. The central regions of galaxies have very high dispersions and dispersion values decrease further away from these regions. The high dispersion seen in

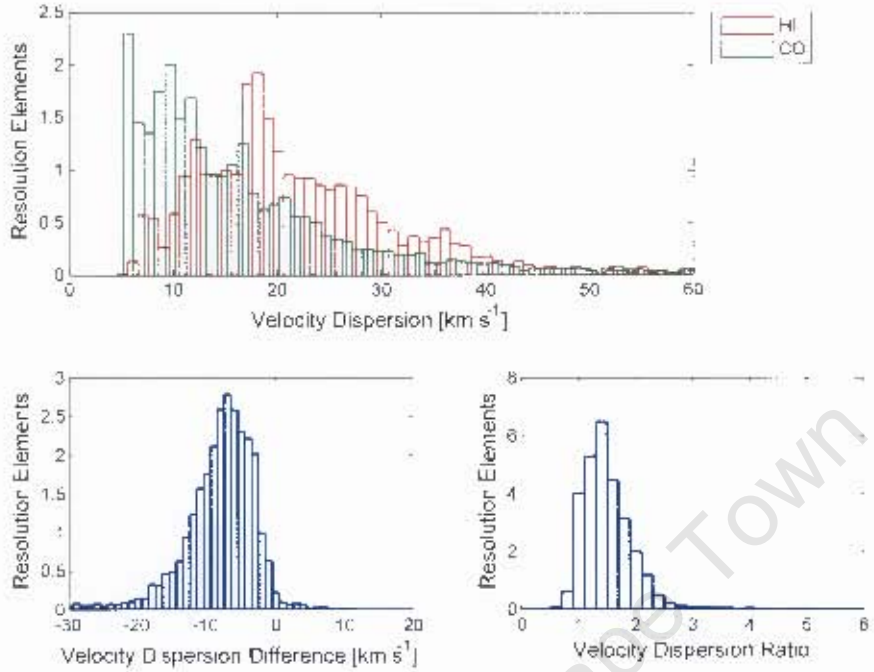

Figure 3.2: (Top) Distributions of the HI and CO dispersions for NGC 4736. Lower left and right figures are histograms of the dispersion difference $\sigma_{CO} - \sigma_{HI}$ and dispersion ratio σ_{HI}/σ_{CO} distributions in NGC 4736.

the central regions could be exaggerated because of rotation. Some high dispersion structures are also found in the outer areas of the galaxies. The size of structures is larger than seen in the $\sigma_{CO} - \sigma_{HI}$ maps, and the structures also seem smoother. Figure 3.11 shows distributions of CO velocity dispersions values of the galaxies that were analyzed in the sample. The CO velocity dispersion ranges from $\sim$ 5 to $\sim$ 25 km s^{-1}; with modes ranging ranging from 6 to 15 km s^{-1}. Most of the galaxies have mean values below 10 km s^{-1}. NGC 5055, NGC 6946, NGC 3077, NGC 925, NGC 2903, NGC 5194 and NGC 3198 have many pixels with $\sigma_{CO} > 9$ km s^{-1}. The σ_{HI} values range from 8 to 30 km s^{-1}, with modes ranging from 11 to 23 km s^{-1}. Unlike the CO dispersions, the HI velocity dispersion distributions decline before the imposed HI velocity resolution cut-offs.

Plots of dispersion differences and dispersion ratio distributions for all the galaxies in the sample are shown in Figures 3.7 and 3.8. The $\sigma_{CO} - \sigma_{HI}$ values range from -20 to 0 km s^{-1} and σ_{HI}/σ_{CO} from 0.5 to 3.5 (see Figure 3.7 and 3.8). We fitted Gaussian functions to the dispersion differences and dispersion ratios and determined the mean values from these fits. The mean values for each of the galaxies are listed in Table 3.2, these are accompanied by the 1σ confidence interval for the fitted mean. The fits can be compared by the sum of the squared residuals that are also found in Table 3.2. These were calculated by taking the sum

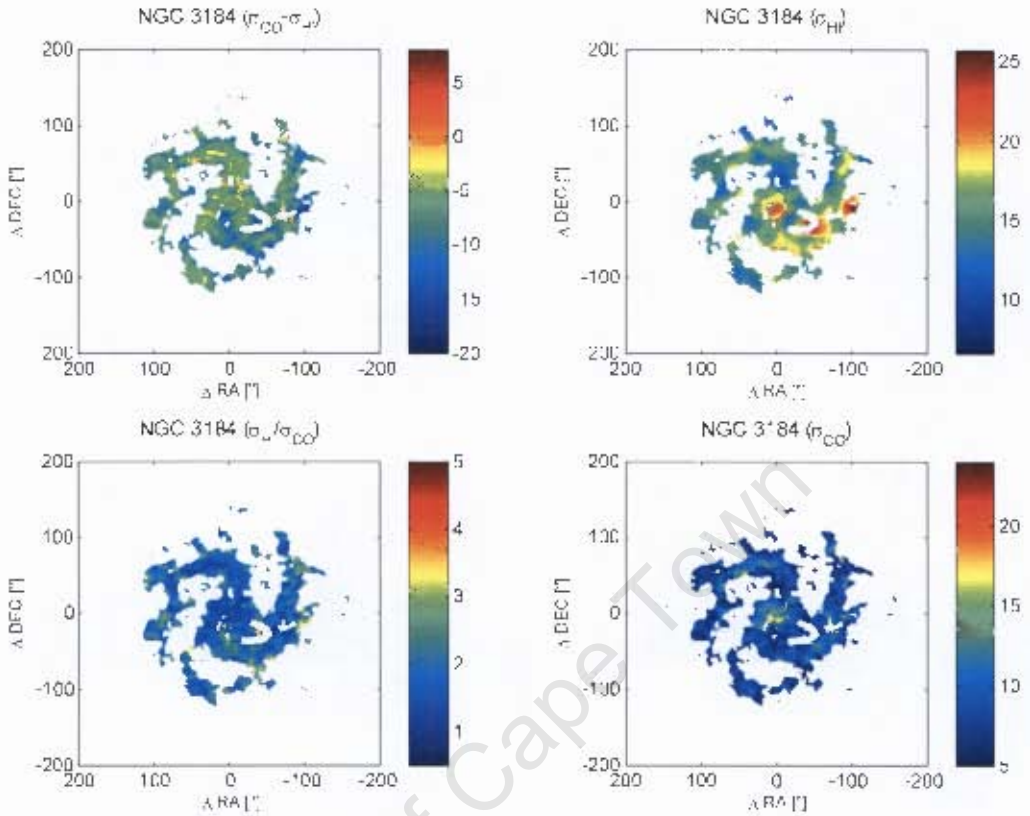

Figure 3.3: Dispersion difference ($\sigma_{CO} - \sigma_{HI}$) (top left), dispersion ratio (σ_{HI}/σ_{CO}) (bottom left), CO dispersion (bottom right) and HI dispersion (top right) maps of NGC 3184. The colourmap values of the dispersion plots are in units of $\mathrm{km\,s^{-1}}$.

of the squared residuals between the fit and data (with the y-axis normalized to fraction of total pixels instead of resolution elements in Figures 3.3,3.4 3.5-3.8). Care should be taken when interpreting fits from NGC 3077, NGC 925 and NGC 4214. This is partly because not many pixels were above the noise threshold for these galaxies and the CO emission regions are very patchy and small, covering very few resolution elements. The mean $\sigma_{CO} - \sigma_{HI}$ value is $7.2 \pm 1.3\,\mathrm{km\,s^{-1}}$; and mean dispersion ratio* σ_{HI}/σ_{CO} is $1.54 \pm 0.18\,\mathrm{km\,s^{-1}}$. The reported errors in these means are the standard deviations of the fitted mean values for the galaxies.

Dispersion ratios are very useful because unlike the differences they are more independent of the absolute values of the dispersions. A rich substructure in $\sigma_{CO} - \sigma_{HI}$ is prominent in the maps, with values that are not uniform across galactic disks. This is mirrored in the σ_{HI}/σ_{CO} maps. The scale of differences between the HI and CO depends on the galaxy. In every galaxy there are small regions where the apparent CO dispersions are higher than the

*This was calculated for all the galaxies excluding NGC 3077 and NGC 2841, because of the relatively large 1σ confidence values of their fitted means see Table 3.2

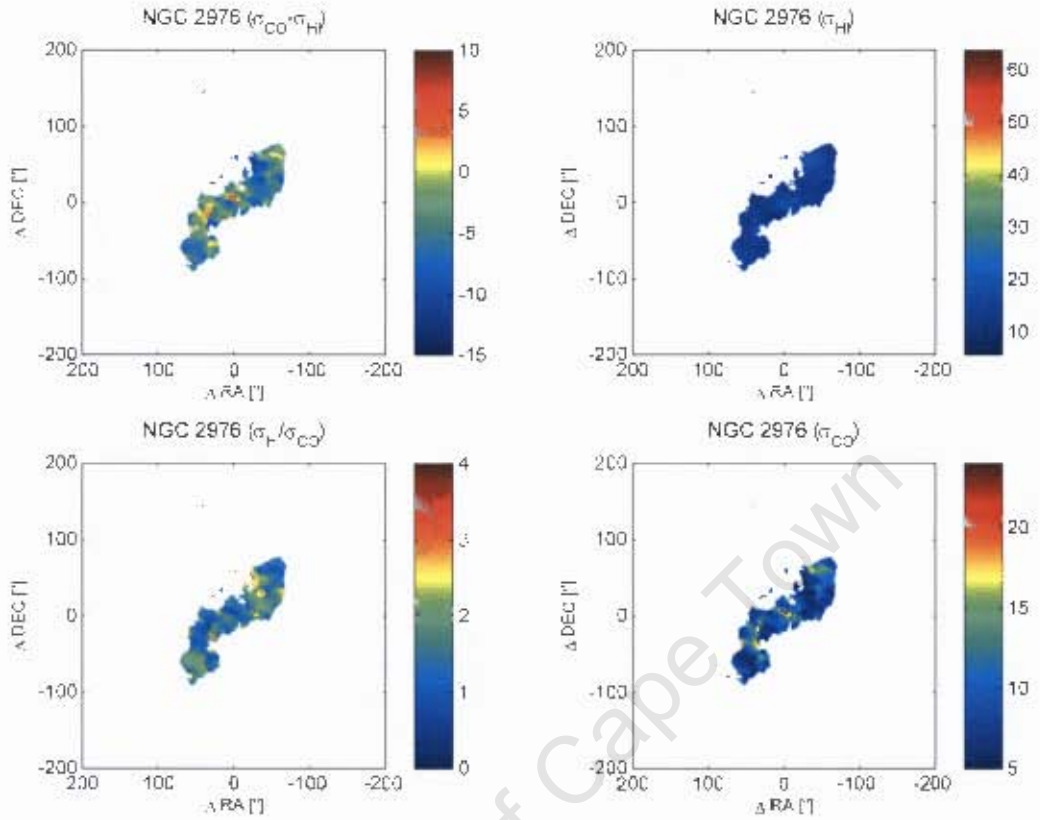

Figure 3.4: Dispersion difference ($\sigma_{CO}-\sigma_{HI}$) (top left), dispersion ratio (σ_{HI}/σ_{CO}) (bottom left), CO dispersion (bottom right) and HI dispersion (top right) maps of NGC 2976. The colourmap values of the dispersion plots are in units of km s^{-1}.

HI dispersions. In the centers of some of the galaxies (NGC 5055, NGC 6946, NGC 2903, and NGC 7331, see Chapter 5 and Appendix) there are extended regions where the CO dispersions are apparently higher than the HI dispersions. These regions have surprisingly low σ_{HI}/σ_{CO} ratios. Part of the explanation for the high dispersion in these regions could be due to the steep gradient in rotation velocity in the beam due to steep rotation curves in the central regions of the galaxies. The rotation curves of our galaxies were determined in de Blok et al. 2008. If a single beam incorporates regions with a steep rotation curve the velocity gradient will lead to an apparent broadening of the velocity profiles. When a single beam incorporates regions with large velocity differences due to rotation the observed velocity profiles in the beam will be very broad. This broadness is thus not related to intrinsic dispersion of the gas. NGC 5055 and NGC 6946 have extended structures around their central regions with very negative $\sigma_{CO} - \sigma_{HI}$ values (compared to the rest of their disks). These structures also show up in the σ_{HI}/σ_{CO} maps.

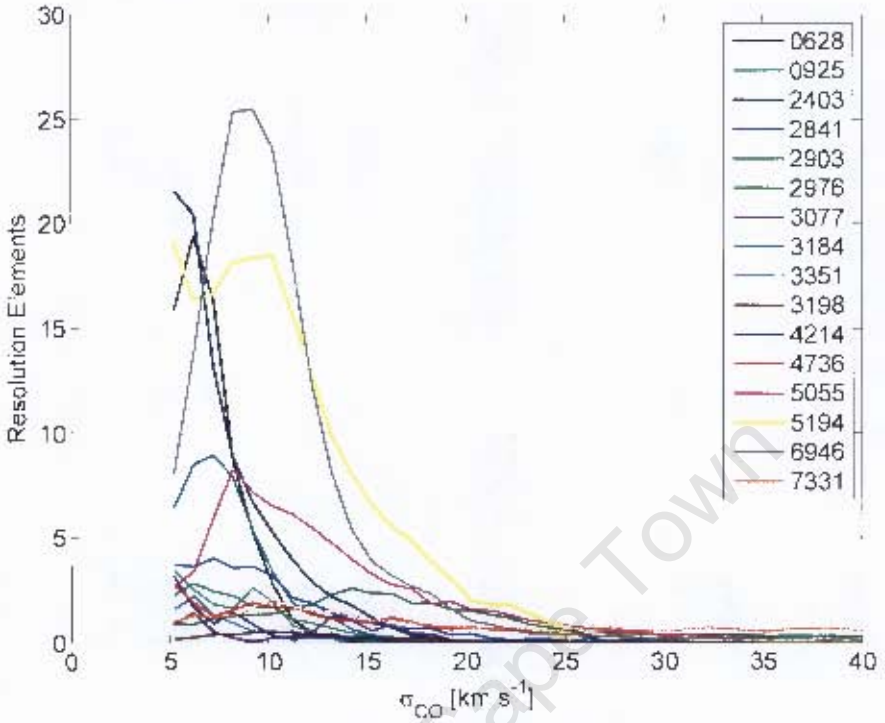

Figure 3.5: Distributions of the CO dispersions (σ_{CO}) of the galaxies. The plots are colour-coded and NGC numbers of the galaxies are in the legend. There is a cut-off at 5.2 km s^{-1} because the velocity resolution of the CO observations of the galaxies (except for NGC 7331, see Sec 2.4) is 5.2 km s^{-1}.

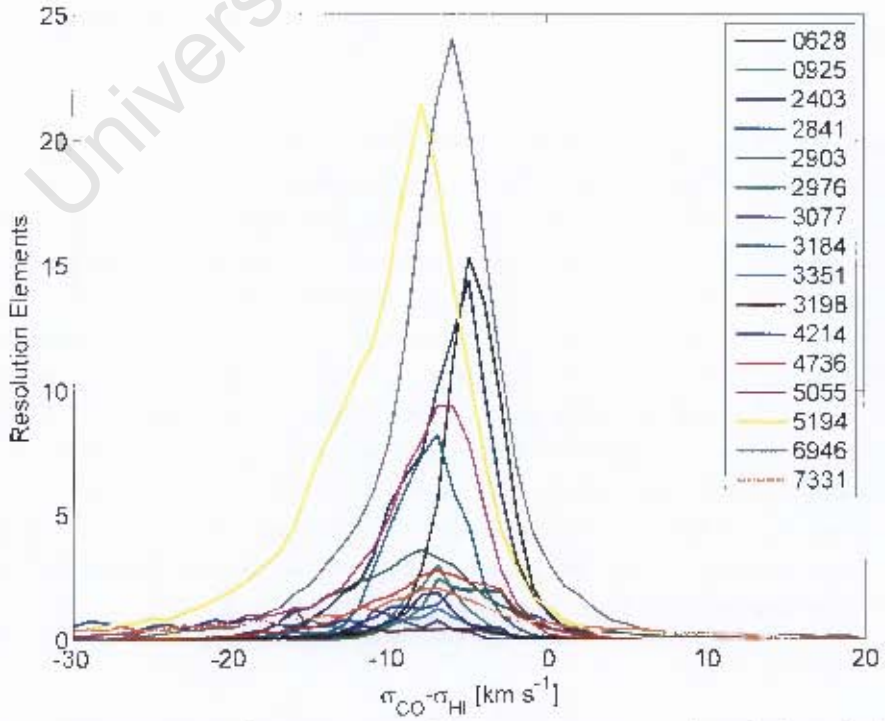

Figure 3.7: Distributions of the dispersion differences $\sigma_{CO} - \sigma_{HI}$ values of the galaxies. The lines are colour-coded and NGC numbers of the galaxies are in the legend.

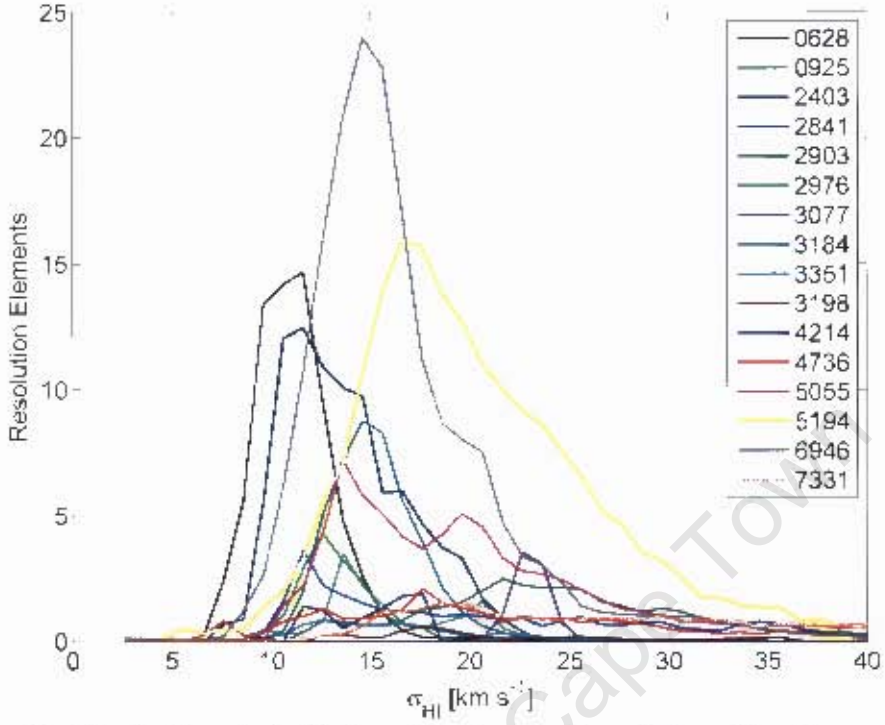

Figure 3.6: Distributions of the HI dispersions (σ_{HI}) of the galaxies. The plots are colour-coded and NGC numbers of the galaxies are in the legend. There are velocity cut-offs at 2.6 km s^{-1} and 5.2 km s^{-1} due to the velocity resolutions of the observations.

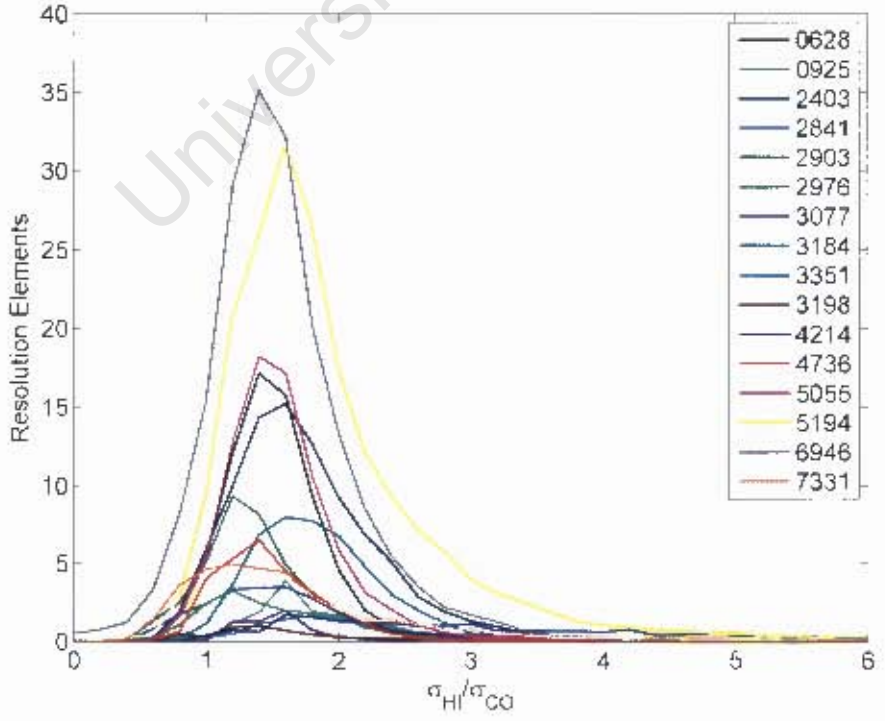

Figure 3.8: Distributions of the dispersion ratios σ_{HI}/σ_{CO} of the galaxies. The lines are colour-coded and NGC numbers of the galaxies are in the legend.

Table 3.1: The modes of the HI and CO velocity dispersions

Name	Mode of CO velocity dispersion [km s^{-1}]	Mode of HI velocity dispersion [km s^{-1}]
NGC 628	6	11
NGC 925	6	14
NGC 2403	6	12
NGC 2841	8	12
NGC 2903	15	22
NGC 2976	6	13
NGC 3077	14	23
NGC 3184	8	15
NGC 3198	11	18
NGC 3351	7	13
NGC 4214	6	18
NGC 4736	6	18
NGC 5055	9	14
NGC 5194	10	18
NGC 6946	9	15
NGC 7731	11	19

3.2 Radial Trends in Dispersion and Star Formation

Star formation rate density (Σ_{SFR}) maps of the galaxies (except NGC 2903) were obtained from A. Leroy (priv. comm.). Details of the maps are described in Leroy et al (2009). In short, GALEX FUV and Spitzer 24 μm maps were used to determine the Σ_{SFR} maps:

$$\Sigma_{SFR} = (8.1 \times 10^{-2} I_{FUV} + 3.2 \times 10^{-3} I_{24\mu m}) \cos i \quad (3.1)$$

(equation D1 in Leroy et al. 2008); where I_{FUV} is the FUV flux, $I_{24\mu m}$ is the Spitzer 24μm, and i is the inclination. These Σ_{SFR} maps were reprojected to the same projection as the CO and HI cubes used in the analysis to allow comparisons with the dispersion maps.

Radial trends in σ_{CO}, σ_{HI} and Σ_{SFR} were then studied. The task ELLINT was used to average the dispersions and Σ_{SFR} in elliptical annuli. We used 13" sized annuli. Position angles and inclinations from Walter et al. (2008) (their Table 1) were used to define the ellipses for each of the galaxies. The r_{25} (the isophotal radius at which the average surface brightness is 25 mag arcsec^{-2}) values were also taken from Walter et al. (2008). Radial profiles of the σ_{CO}, σ_{HI} and Σ_{SFR} were produced and representative plots are in Figures 3.9 and 3.10; the radial plots for all the galaxies are found in the Appendix. As before, only areas where there is both CO and HI emission above a 4σ level were used.

We find that the dispersions decrease with radius, which is in agreement with Tamburro et al. (2009). This trend is evident in most of the galaxies (e.g. NGC 6946, Figure 3.10), but

Table 3.2: The Gaussian weighted mean dispersion difference ($\sigma_{CO} - \sigma_{HI}$) and dispersion ratio ($\sigma_{HI}/\sigma_{CO}$) for each of the galaxies. The 1σ confidence regions are included as the error in the fitted means.

Name	Mean $\sigma_{CO} - \sigma_{HI}$ [km s^{-1}]	Sum of the Squared Residuals	Mean σ_{HI}/σ_{CO}	Sum of the Squared Residuals.
NGC 628	-4.6 ($\pm$0.1)	0.0005	1.47 ($\pm$0.01)	0.0005
NGC 925	-7.2 ($\pm$0.1)	0.0082	1.68 ($\pm$0.03)	0.0013
NGC 2403	-6.0 ($\pm$0.1)	0.0031	1.62 ($\pm$0.01)	0.0019
NGC 2841	-8.2 ($\pm$0.7)	0.0060	1.49 ($\pm$0.04)	0.0061
NGC 2903	-8.6 ($\pm$0.1)	0.0006	1.30 ($\pm$0.01)	0.0037
NGC 2976	-5.2 ($\pm$0.1)	0.0018	1.39 ($\pm$0.03)	0.0067
NGC 3077	-11.5 ($\pm$0.6)	0.028	1.50 ($\pm$0.03)	0.021
NGC 3184	-7.6 ($\pm$0.1)	0.0005	1.76 ($\pm$0.01)	0.0015
NGC 3198	-8.0 ($\pm$0.2)	0.0035	1.39 ($\pm$0.03)	0.0083
NGC 3351	-8.1 ($\pm$0.2)	0.0048	1.86 ($\pm$0.02)	0.0019
NGC 4214	-7.6 ($\pm$0.1)	0.0066	1.87 ($\pm$0.02)	0.0048
NGC 4736	-7.0 ($\pm$0.1)	0.0012	1.40 ($\pm$0.01)	0.0039
NGC 5055	-7.1 ($\pm$0.1)	0.0022	1.49 ($\pm$0.01)	0.0013
NGC 5194	-8.7 ($\pm$0.1)	0.0021	1.63 ($\pm$0.02)	0.0034
NGC 6946	-6.2 ($\pm$0.1)	0.0014	1.46 ($\pm$0.01)	0.0017
NGC 7731	-8.9 ($\pm$0.4)	0.0023	1.33 ($\pm$0.03)	0.0038

not so clear in a few galaxies (e.g. NGC0628, Figure 3.9). The star formation rate density also declines with radius as expected. In the regions with both HI and CO detections it seems that the $\sigma_{\rm CO}$ is better correlated with $\Sigma_{\rm SFR}$ than $\sigma_{\rm HI}$, but quantification and verification of this was not done in the thesis. The HI velocity dispersion has greater fluctuations than CO velocity dispersion, which declines more smoothly. When the $\sigma_{\rm CO}$ radial trend flattens out - the $\Sigma_{\rm SFR}$ seems to do so as well in many of the galaxies. The velocity dispersions show an exponential decrease as does the star formation rate density.

3.3 Star Formation

In order to study the relationship between dispersions and star formation rate density, the $\Sigma_{\rm SFR}$ pixels were binned into logarithmic bins of size 0.02 dex. The mean σ_{HI}, σ_{CO} and σ_{HI}/σ_{CO} in each bin were calculated. Plots of the results are shown in Figures 3.11, 3.13 and 3.15. The uncertainties in the plots were defined by determining the average of the dispersion (or σ_{HI}/σ_{CO}) uncertainties in each $\Sigma_{\rm SFR}$ bin. The dispersion uncertainties of the individual pixel dispersions were the outputs from XGAUFIT.

There is a large variation in σ_{HI} between the galaxies: there is much less variation in σ_{CO}. Figures 3.11, 3.13 and 3.15 all show evidence for the existence of three regimes. At low $\Sigma_{\rm SFR}$ values ($\Sigma_{\rm SFR} \leq 10^{-2.6}\,{\rm M}_\odot\ {\rm yr}^{-1}\ {\rm kpc}^{-2}$), σ_{CO} values are low ($\leq$10 km s^{-1}) and there is no clear correlation between σ_{CO} and $\Sigma_{\rm SFR}$. The σ_{HI} also seems to show no correlation, but

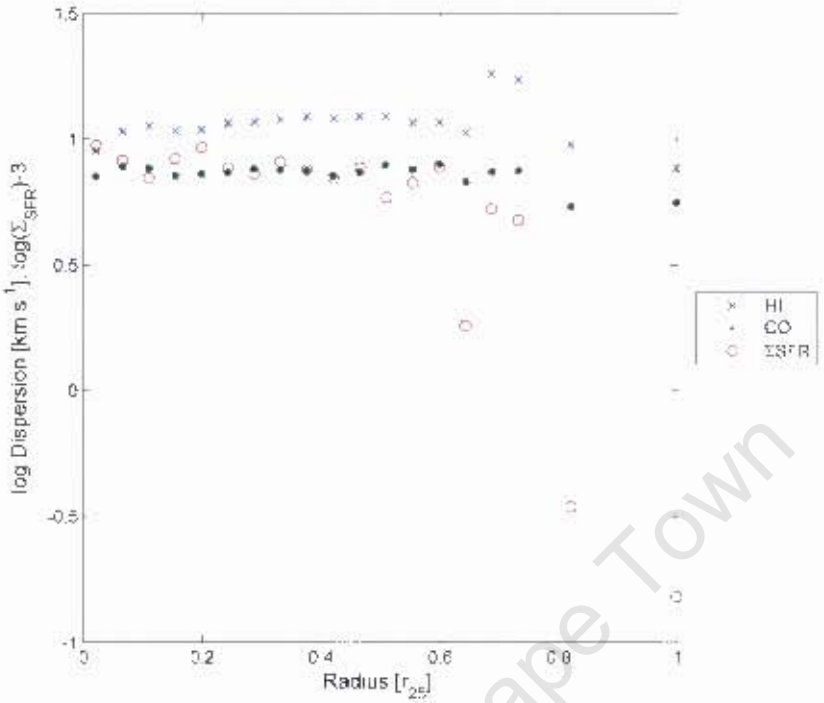

Figure 3.9: The radially smoothed CO and HI dispersions and the star formation rate density versus radius (in units of r_{25}) in NGC 628. Log dispersions are plotted and log star formation rate density −3 is plotted (with Σ_{SFR} in the units : [$M_\odot$ Myr^{-1} kpc^{-2}]).

there is a lot more scatter. There is also no clear correlation between σ_{HI}/σ_{CO} and Σ_{SFR} in this regime. The large variations between galaxies could be due to the large variations seen in σ_{HI}. Between $10^{-3.6} \leq \Sigma_{SFR} \leq 10^{-1.5}$ (units: $M_\odot$ yr^{-1} kpc^{-2}) there is a much clearer correlation. σ_{CO} and σ_{HI} increase with increasing $\log \Sigma_{SFR}$ in a more linear manner than in the lower regime. The σ_{CO} curves rise more steeply than σ_{HI}. The σ_{HI}/σ_{CO} ratio also declines linearly in this regime. And the relation between Σ_{SFR} and σ_{HI}/σ_{CO} is much tighter than relations with HI and CO dispersions. The trends in this regime are clearly shown in Figures 3.12, 3.14 and 3.16. NGC 3077 stands out in Figure 3.16, because its curve remains constant over most of the regime being discussed then has a sharp drop at at higher Σ_{SFR} values. For $\Sigma_{SFR} > 10^{-1.5} M_\odot$ yr^{-1} kpc^{-2} the correlations are not as strong as in the lower Σ_{SFR} regime, and the gradients are also generally higher. There are however large variations between the galaxies. All $\Sigma_{SFR} < 10^{-4} M_\odot$ yr^{-1} kpc^{-2} values were not used in the preceding analysis because the uncertainty in these values was too high.

In order to determine whether the trends extend out to regions where there is no detectable CO and also to see whether the overall HI trends are different from those of HI in the regions with detected CO, we studied the dispersion-SFR relationship over the entire

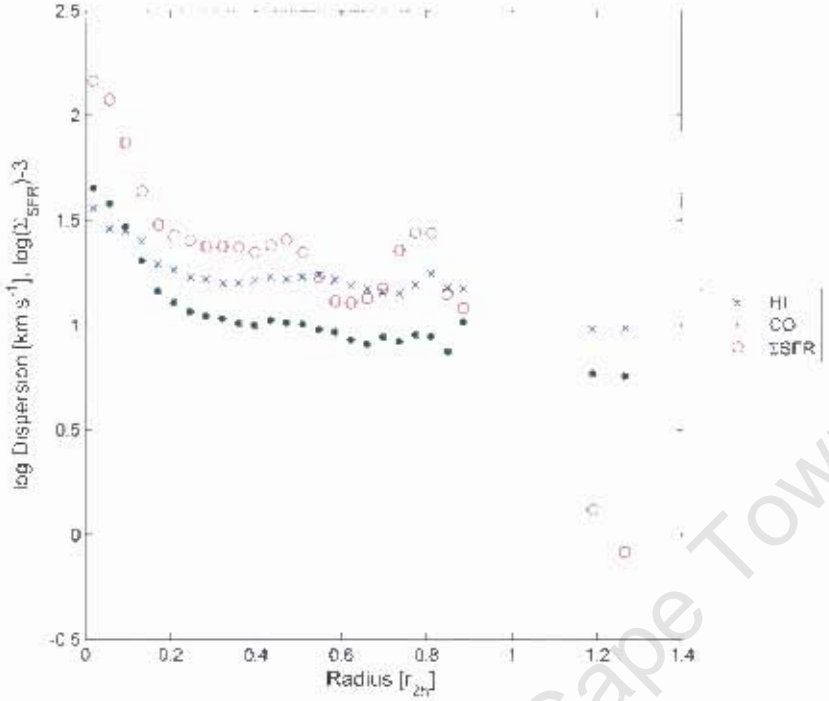

Figure 3.10: The radially smoothed CO and HI dispersions and the star formation rate density versus radius (in units of r_{25}) in NGC 6946. Log dispersions are plotted and log star formation rate density −3 is plotted (with Σ_{SFR} in the units : [$M_\odot$ Myr^{-1} kpc^{-2}]).

star-forming disk. Dispersion maps of HI were made for entire disks of the galaxies, and then a similar procedure to the one described previously was applied to these dispersions. Figure 3.17 shows that the correlation between HI velocity dispersion and Σ_{SFR} exists over the entire star-forming disk. The correlation exists at all values of Σ_{SFR} and the $\Sigma_{SFR} \geq 10^{-2.6}$ $M_\odot$ yr^{-1} kpc^{-2} threshold mentioned previously is not as clear as in seen the previous figures. There does however appear to be a gradient change at the threshold values mentioned previously ($\Sigma_{SFR} = 10^{-2.6}$ and $10^{-1.5}$ $M_\odot$ yr^{-1} kpc^{-2}). For $\Sigma_{SFR} \geq 10^{-2}$ $M_\odot$ yr^{-1} kpc^{-2} NGC 2841's curve shows very erratic behaviour (see Figure 3.17). This behaviour does not occur in the other plots, which indicates that the erratic behaviour of the curve may be due to low S/N pixels or pixels from the central region whose dispersions are not a true indication of the widths of their velocity profiles.

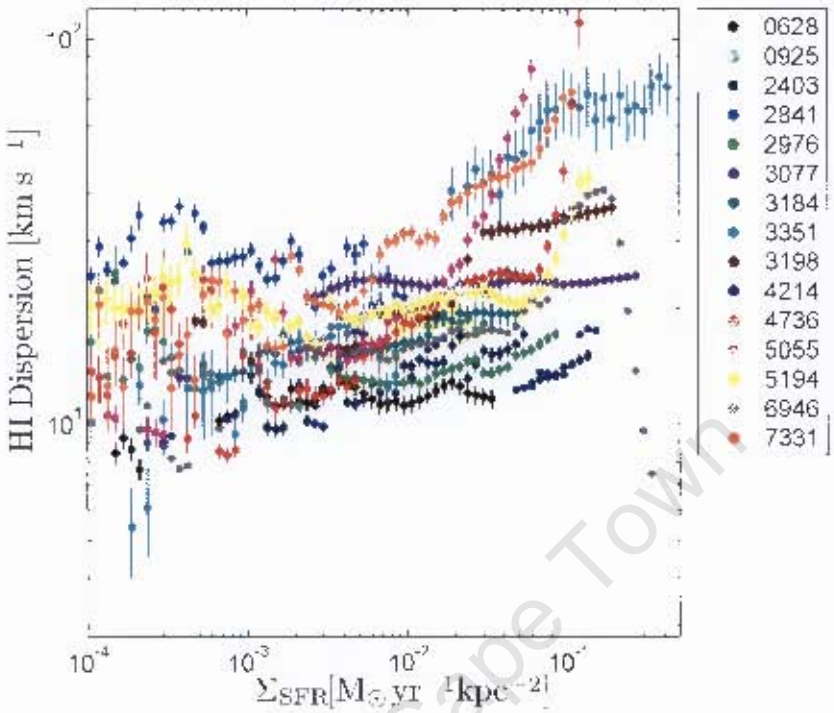

Figure 3.11: Plot of the averaged HI dispersions versus the star formation rate density for each of the galaxies. Each colour corresponds to an individual galaxy, and the NGC numbers of the galaxies are shown in the legend.

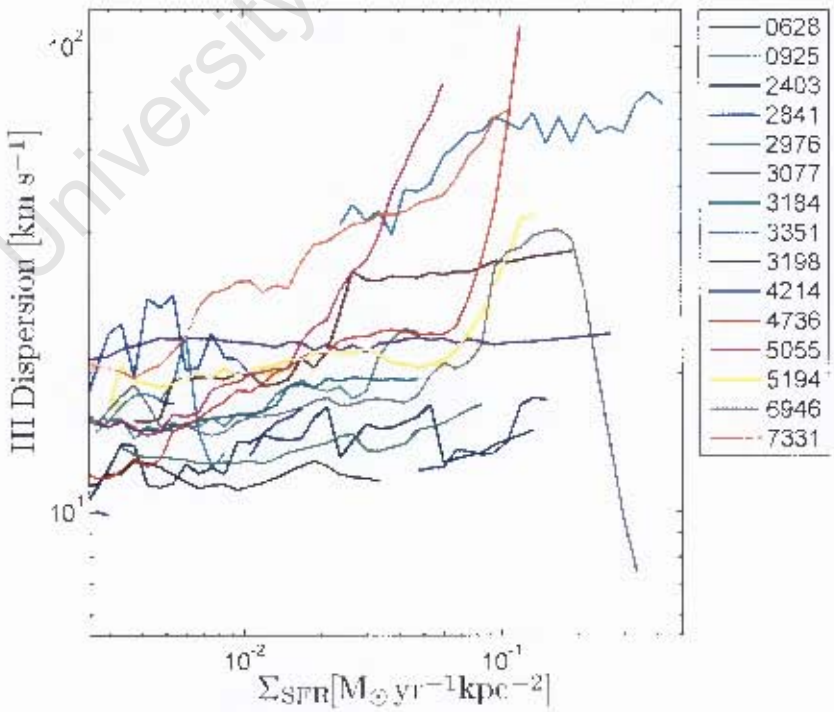

Figure 3.12: The averaged HI dispersions versus the star formation rate density for each of the galaxies. This is the part of Figure 3.11 that covers the Σ_{SFR} range where a steady decrease in σ_{HI}/σ_{CO} is clear. Each colour corresponds to an individual galaxy, and the NGC numbers of the galaxies are shown in the legend. The errorbars are shown in Figure 3.11 and were omitted here to make the plot clearer.

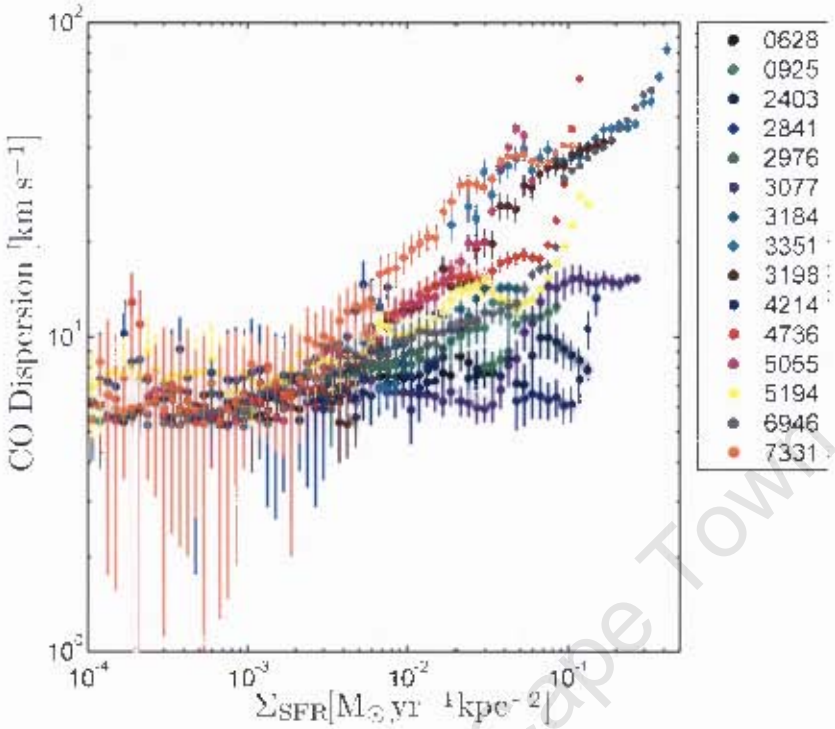

Figure 3.13: The averaged CO dispersions versus the star formation rate density for each of the galaxies. Each colour corresponds to an individual galaxy, and the NGC numbers of the galaxies are shown in the legend.

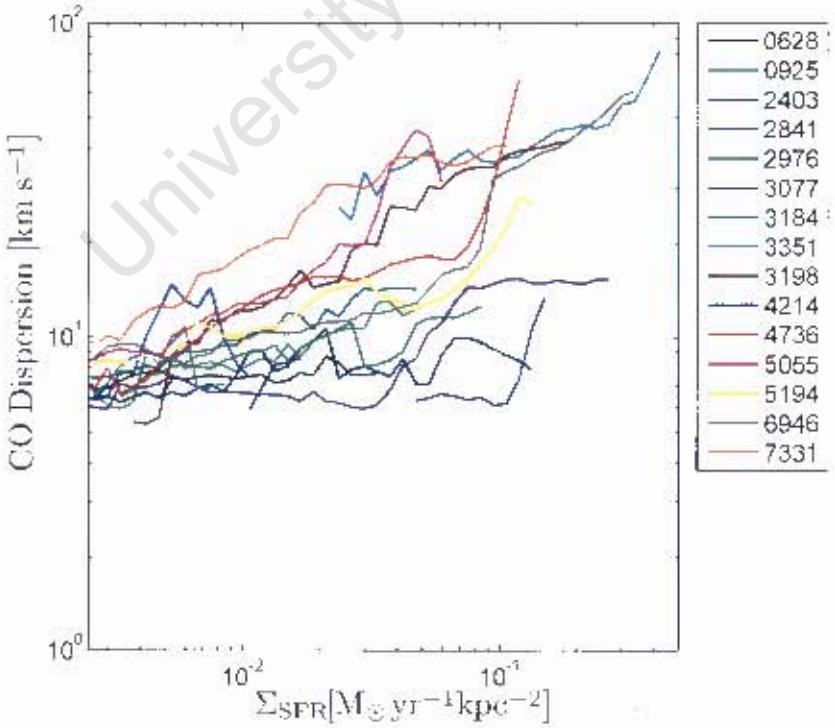

Figure 3.14: The averaged CO dispersions versus the star formation rate density for each of the galaxies. This is the part of Figure 3.13 that covers the Σ_{SFR} range where a steady decrease in σ_{HI}/σ_{CO} is clear. Each colour corresponds to an individual galaxy, and the NGC numbers of the galaxies are shown in the legend. The errorbars are shown in Figure 3.13 and were omitted here to make the plot clearer.

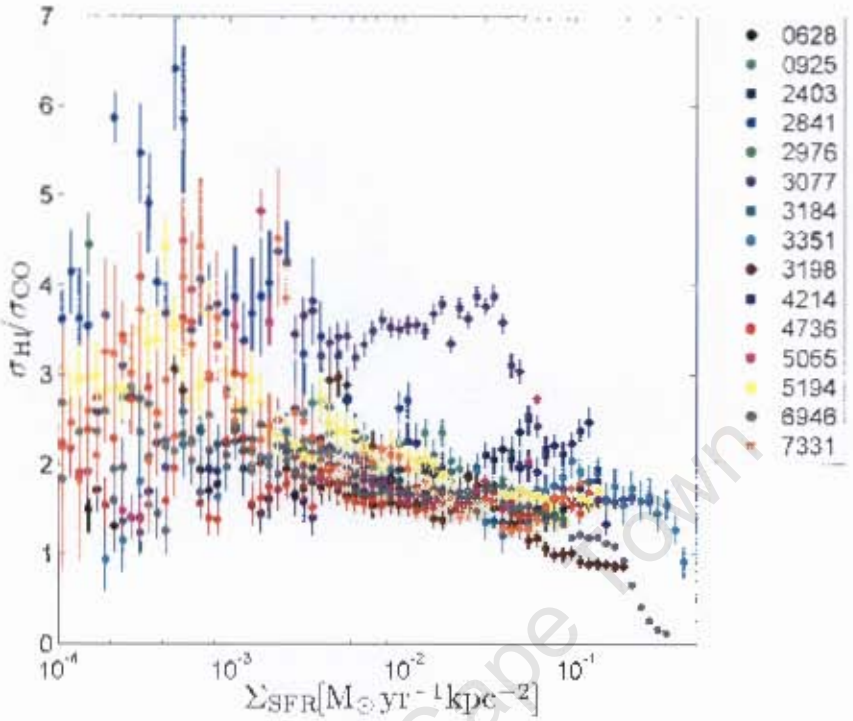

Figure 3.15: Plot of the averaged dispersions ratio versus the star formation rate density for each of the galaxies. Each colour corresponds to an individual galaxy, and the NGC numbers of the galaxies are shown in the legend.

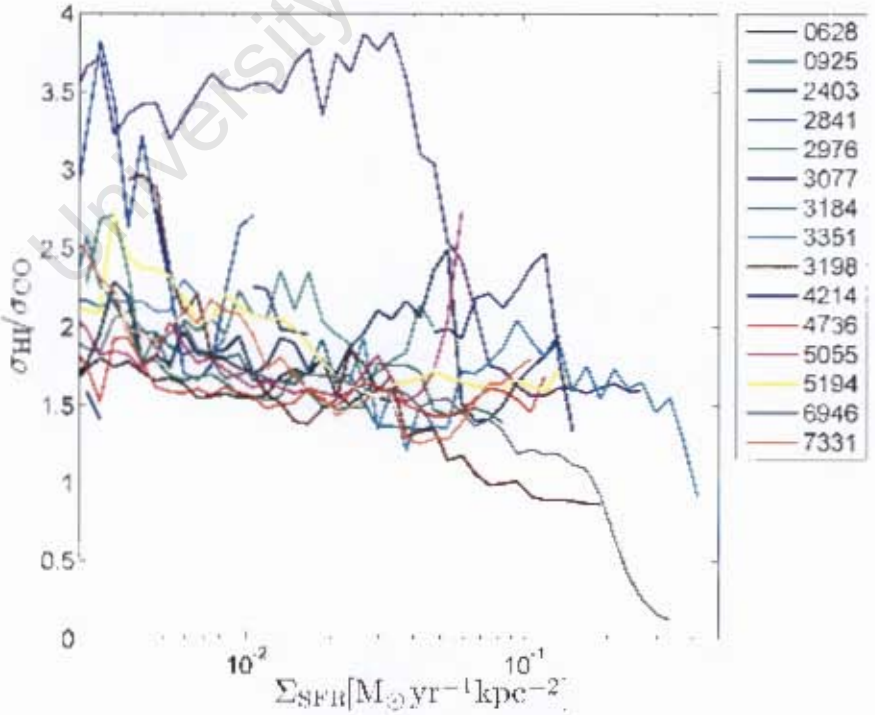

Figure 3.16: The averaged dispersions ratio versus the star formation rate density for each of the galaxies. This is the part of Figure 3.15 that covers the Σ_{SFR} range where a steady decrease in σ_{HI}/σ_{CO} is clear. Each colour corresponds to an individual galaxy, and the NGC numbers of the galaxies are shown in the legend. The errorbars are shown in Figure 3.15 and were omitted here to make the plot clearer.

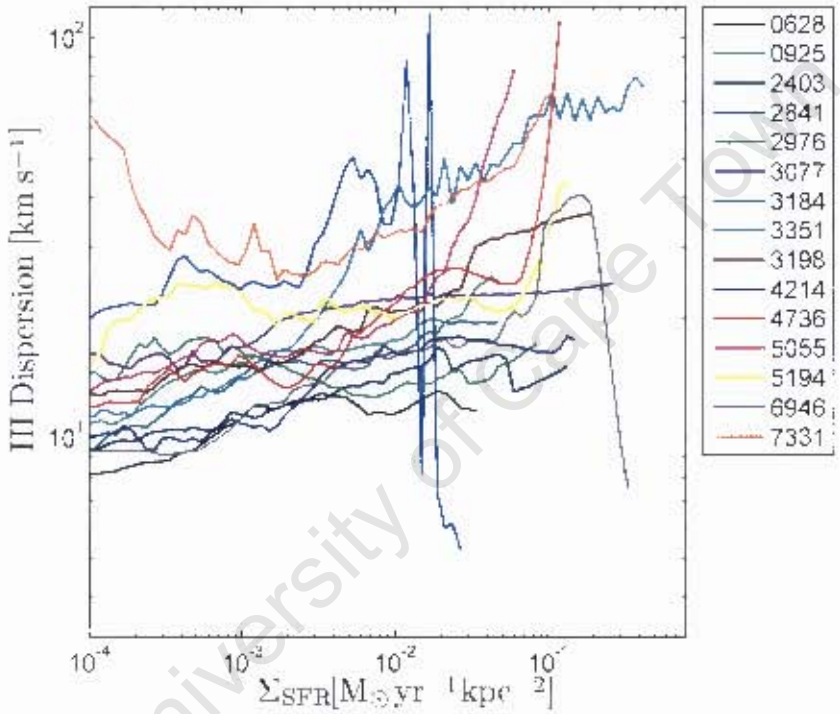

Figure 3.17: Plot of the averaged HI dispersions versus the star formation rate density for each of the galaxies. This is of all the pixels in the galaxy where HI emission is higher that the 4σ noise cut-off, dispersion greater than the velocity resolution and with star formation rate density above $10^{-4}\,M_\odot\,yr^{-1}\,kpc^{-2}$.

Chapter 4

Results : Profiles, Inclination and Distance effects

4.1 Velocity Profiles

In the preceding chapters, the dispersions used have been from Gaussian distribution fits to the data. In this chapter we quantify how well Gaussian distributions fit the data compared to Hermite fits. The HI and CO velocity profile shapes and the Gaussian and Hermite fits were analysed in seven of the galaxies (NGC 628, NGC 2403, NGC 3184, NGC 3077, NGC 5055, NGC 6946) in order to determine the fitting function that is used for the entire sample.

The large majority of velocity profiles in the galaxies can be represented by the plots in Figures 4.3 and 4.2. In this it is clearly evident that the shapes of the HI and CO velocity profiles are mostly Gaussian. On inspection the Gaussian and Hermite h_3 both fit the velocity profiles well (quantification of the goodness-of-fits is found in Sec.4.2). However, in some regions the profiles appear to be very asymmetric and non-Gaussian in shape. Examples of profiles from these regions are shown in Figure 4.3. In these regions both Gaussian and Hermite h_3 fits struggle to fit the data, but they at least seem to capture the widths of the profiles well. The Hermite h_3 fits are better than the Gaussian ones in these regions.

4.2 Different Fitting Functions

The reduced χ^2 of the fits and the uncertainties in the fitted dispersions were used to assess the suitability of Gaussian, Hermite h_3 and Hermite h_4 functions for use in the velocity profile fitting and determining of velocity dispersions suitable for this work. The relative dispersion

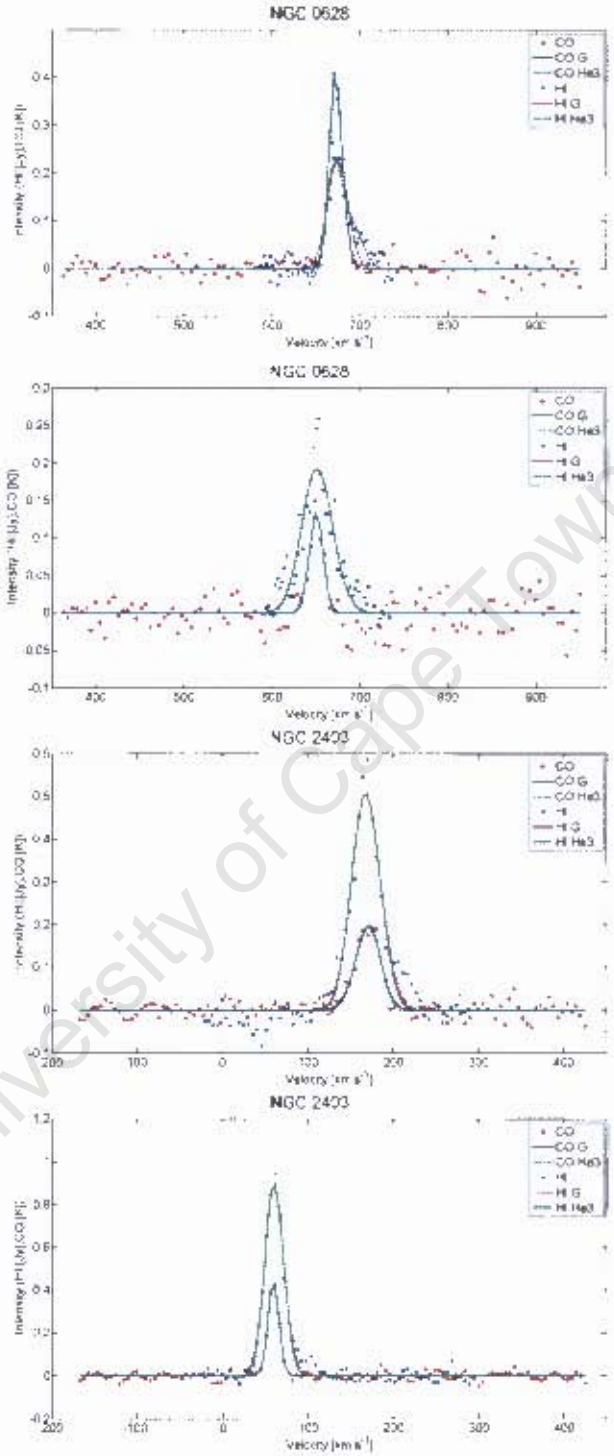

Figure 4.1: Representative plots of the velocity profiles found in the galaxies analysed. In each plot the original data (CO in red dots, HI blue squares) is plotted, with lines of the Gaussian fits (black and purple solid lines) and Hermite h_3 fits (dashed cyan and green lines). Profiles are from NGC 628 (top two plots) and NGC 2403 (next two plots).

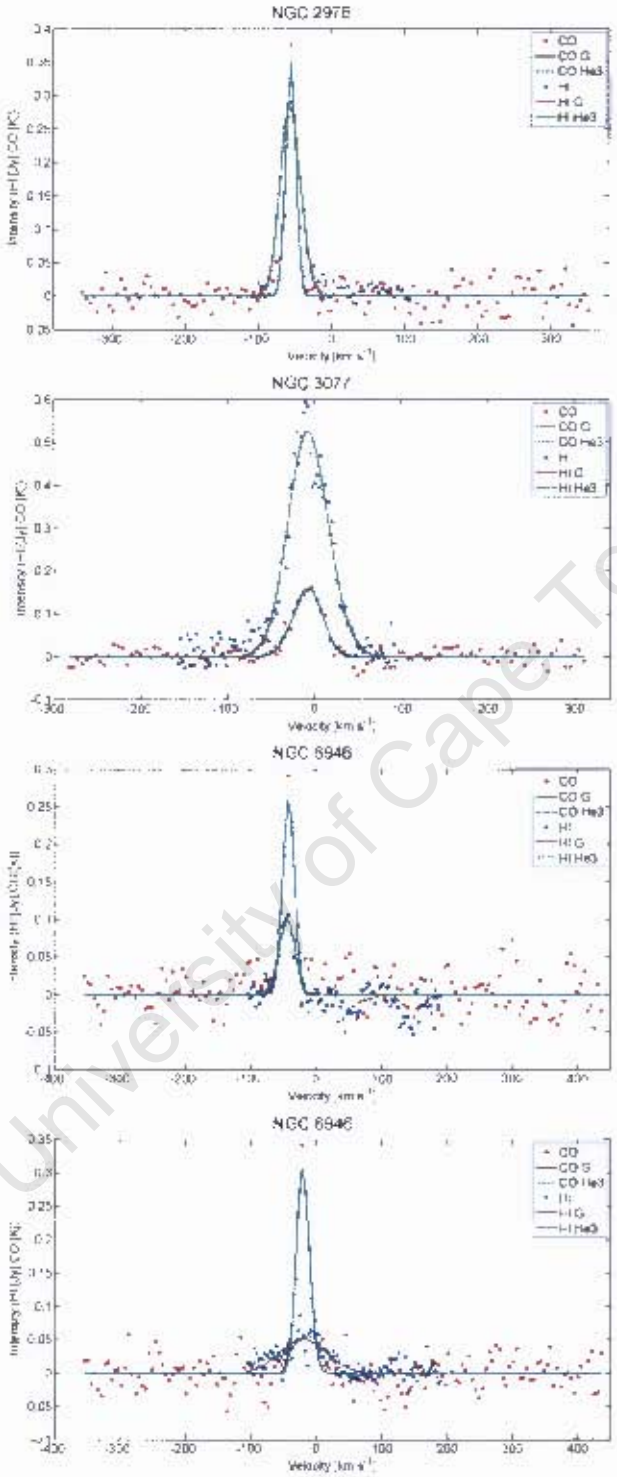

Figure 4.2: Representative plots of the velocity profiles found in the galaxies analysed. In each plot the original data (CO in red dots, HI blue squares) is plotted, with lines of the Gaussian fits (black and purple solid lines) and Hermite h_3 fits (dashed cyan and green lines). Profiles are from NGC 2976 (top left), NGC 3077 (top left) and NGC 6946 (bottom two plots).

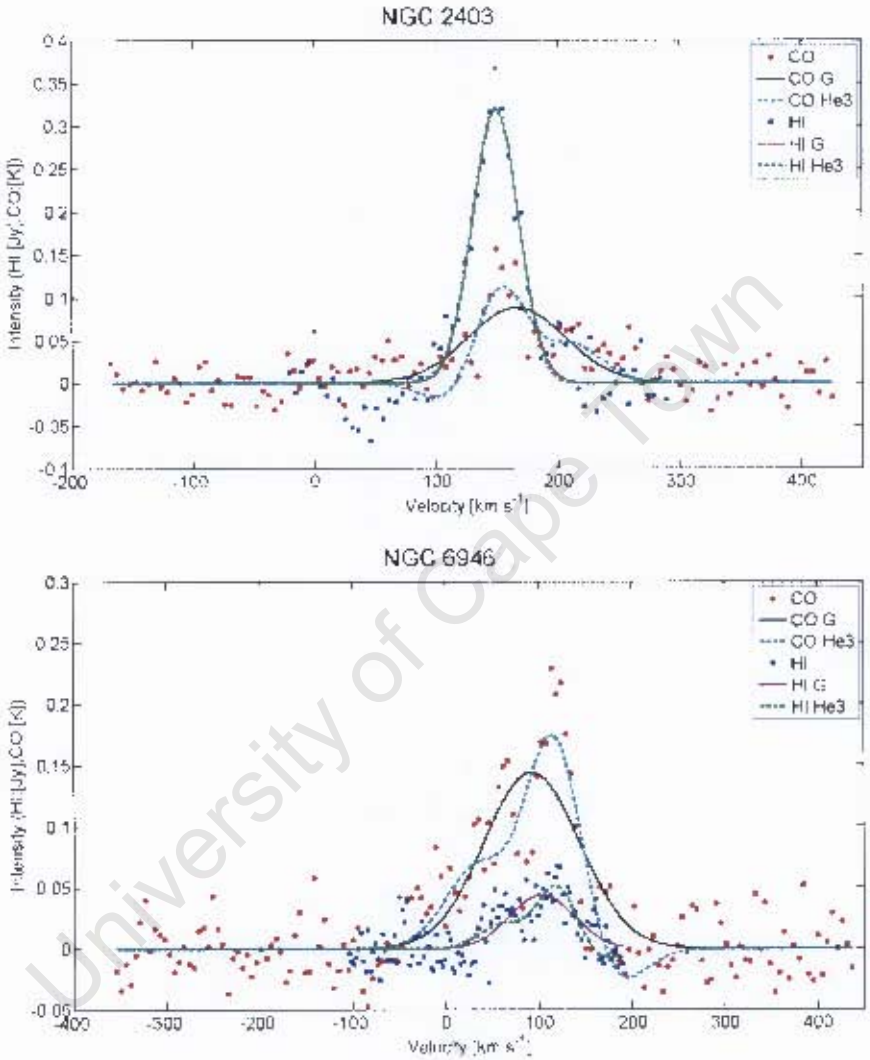

Figure 4.3: Representative plots of some of the very asymmetric velocity profiles found in the galaxies analysed. In each plot the original data (CO in red dots, HI blue squares) is plotted, with lines of the Gaussian fits (black and purple solid lines) and Hermite h_3 fits (dashed cyan and green lines). Profiles are from NGC 2403 (top) and NGC 6946 (bottom).

uncertainties from the Gaussian, Hermite h_3 and Hermite h_4 plots of two representative galaxies are shown in Figures 4.4 and 4.5 . These clearly show that the relative dispersion uncertainties (σ_{unc}/σ) of Hermite h_4 dispersions are much higher than those of Hermite h_3 and Gaussian. Hermite h_3 σ_{unc}/σ are similar, but have slightly lower values than Gaussian σ_{unc}/σ. This is true for HI and CO fits. CO fits have higher relative uncertainties than HI in general. The differences between Gaussian and Hermite h_3 uncertainty distributions are much smaller for CO fits compared to HI fits. From these plots we can see that the uncertainty in the HI velocity dispersions fit by Gaussian and Hermite h_3 functions is $\lessapprox 5\%$. The uncertainties in HI dispersions fit by Hermite h_4 is $\lessapprox 10\%$. The uncertainty in Gaussian and Hermite h_3 CO velocity dispersions is $\sim 7\%$ to $\sim 20\%$. The uncertainty in Hermite h_4 dispersions ranges from $\sim 10\%$ to $\sim 45\%$.

The reduced χ^2 between Hermite h_3 and Hermite h_4 are shown in Figures 4.6 and 4.7. These were calculated by XGAUFIT, and the noise values shown in Table 2.1 were used as the standard error in the calculation. The plots clearly show that the reduced χ^2 values for Gaussian and Hermite h_3 are similar. The Hermite h_4 reduced χ^2 values are similar but a little lower for the HI, whereas the CO values are very similar to the other fits. The CO reduced χ^2 values are lower than the HI χ^2 values. Therefore Gaussian fits generally have good χ^2 values and the lowest relative errors in dispersion.

4.3 Effect of Distance and Inclination

As discussed in Sections 1.5 and 1.4 the scale at which one measures dispersions is important in order to be able to interpret them. At small scales the velocity dispersions have a power-law relationship with molecular cloud size (see Section 1.4; Larson et al 1981 and the references noted in the section). The distances of our galaxies range from 2.9 to 14.7 Mpc, therefore the scales at which our dispersions are being measured range from 200 pc to 1 kpc. As the inclinations of galaxies increase, the contribution of the planar dispersion σ_{xy} to σ_{obs} also increases. As discussed in Section 1.4, the two components are anisotropic. The broadening effect of galactic rotation also increases, therefore distorting the observed profiles. The effect of scale and inclination on our measured dispersions can affect our interpretations of the data. We therefore plotted the modes of the CO and HI dispersions against inclination and distance in order to determine how great the effect is on the measured dispersions. See Figures 4.8-4.11. The distributions have different widths and are not all Gaussian. In order to estimate uncertainties we use the dispersion histograms (e.g. Figures 3.11-3.12) for each galaxy, we sum the number pixels from the miminum dispersion bin until 12.5% of the total number of pixels were counted; then similarly pixels were summed from the maximum dispersion bin until 12.5% were counted. The dispersion values where 12.5% was reached from the minimum and maximum sides constitute the range of dispersions containing 75% of the pixels. The ranges of dispersions that 75% of the pixels in each galaxy cover were shown as errorbars in the abovementioned figures. The peaks of many of the CO dispersion distribu-

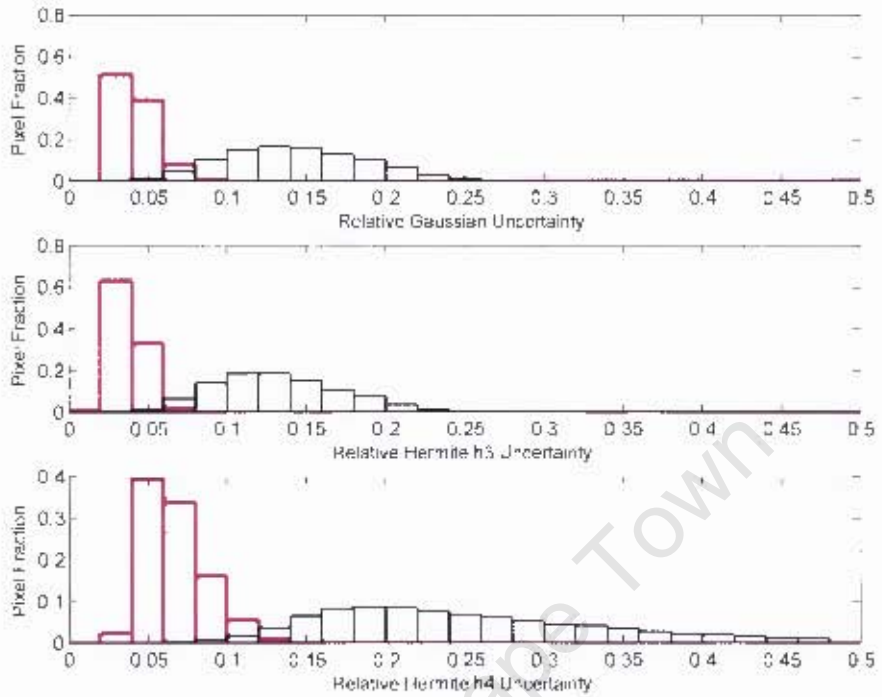

Figure 4.4: Histograms of the relative velocity dispersion uncertainties (σ_{unc}/σ) of NGC 2403. The HI is represented by the thick magenta lines and CO by the black (thinner) lines. The top plot is the Gaussian relative dispersion uncertainty distribution, the middle shows the Hermite h3 and bottom plot shows the Hermite h_4 relative dispersion uncertainty distribution.

tions are close to the 5.2 km s^{-1} dispersion cut-off, and the true 12.5% lower bound for some distributions falls below this cut-off value and is therefore indeterminate. The errorbars for these are down to the dispersion cut-off value in Figures 4.8-4.9. Some galaxies such as NGC 6946 and NGC 925 show no lower bounds for their 75% ranges (for HI dispersion) because large fractions of their pixels are in the tails of their distributions leading to biased values.

Figures 4.8 and 4.10 show that there is no clear relation between velocity dispersions and distances of the galaxies (for our 2.9 – 14.7 Mpc range). There is a hint of a correlation with inclination, but Figures 4.9 and 4.11 only show tentative evidence of this. The fraction of galaxies with dispersion ranges above 15 km s^{-1} increase with increasing inclination (see Figures 4.9 and 4.11), this trend is not as clear in the case of increasing distances. NGC 7331 and NGC 3351 have the largest HI dispersion ranges, while NGC 7331 and NGC 4736 have the largest CO dispersion ranges.

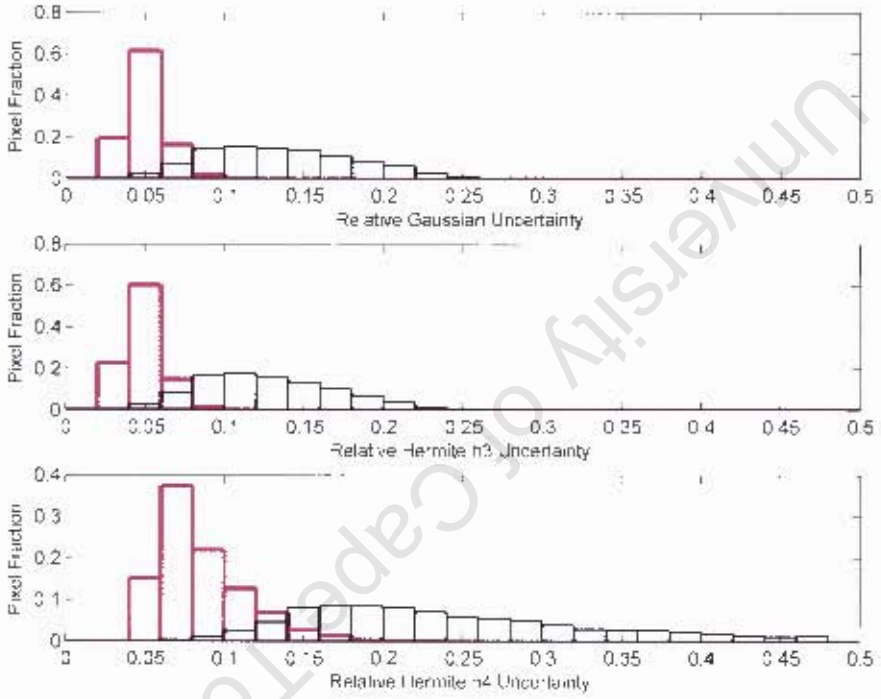

Figure 4.5: Histograms of the relative velocity dispersion uncertainties (σ_{unc}/σ) of NGC 3184. The HI is represented by the thick magenta lines and CO by the black (thinner) lines. The top plot is the Gaussian relative dispersion uncertainty distribution, the middle shows the Hermite h_3 and bottom plot shows the Hermite h_4 relative dispersion uncertainty distribution.

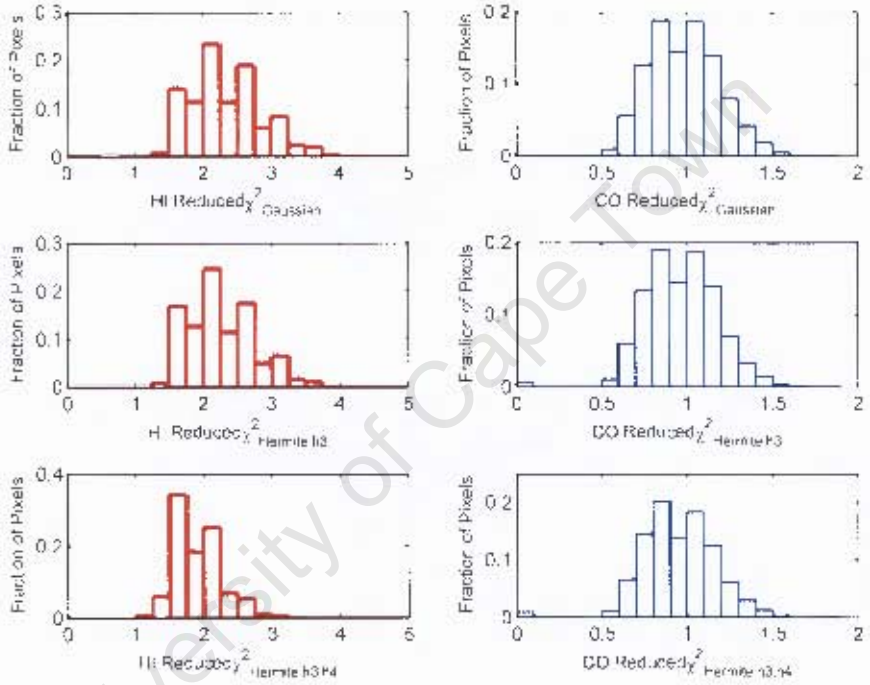

Figure 4.6: Histograms of the χ^2 values of Gaussian, Hermite h_3 and Hermite h_4 fits of NGC 3184's velocity profiles. The HI is shown in the left column and the CO in the right column. The top plot shows the Gaussian, middle plot shows the Hermite h_3 and the bottom plot shows the Hermite h_4 χ^2 distributions.

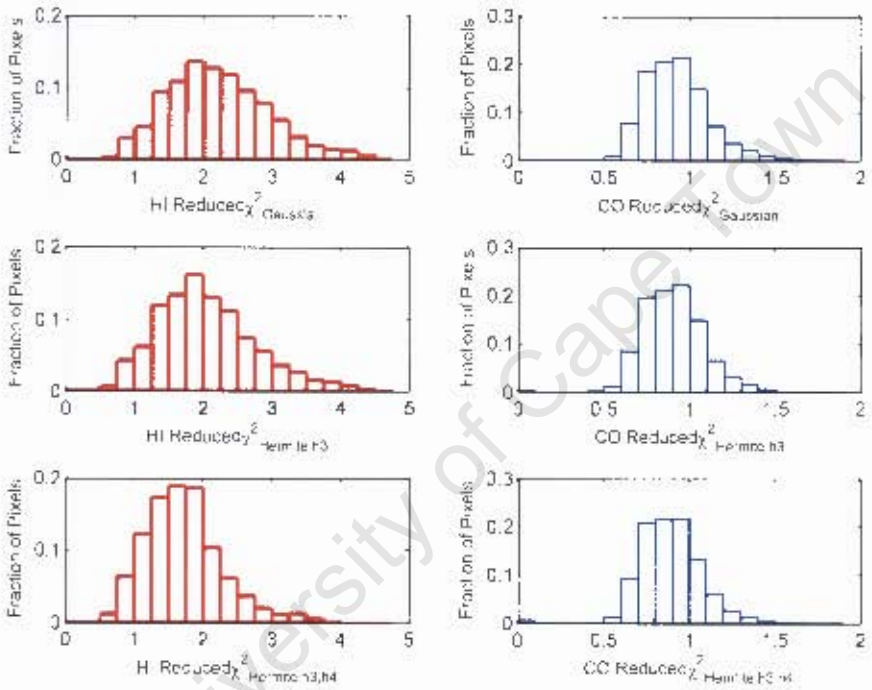

Figure 4.7: Histograms of the χ^2 values of Gaussian, Hermite h_3 and Hermite h_4 fits of NGC 5055's velocity profiles. The HI is shown in the left column and the CO in the right column. The top plot shows the Gaussian, middle plot shows the Hermite h_3 and the bottom plot shows the Hermite h_4 χ^2 distributions.

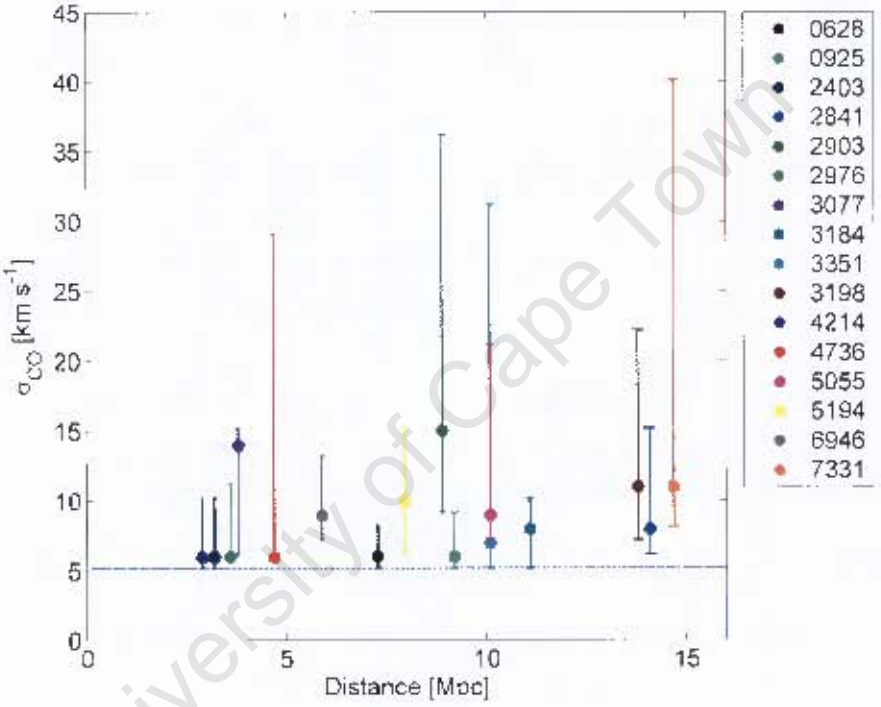

Figure 4.8: The CO dispersion (σ_{CO}) modes of the galaxies versus the distances of the galaxies. The error bars represent the ranges of CO dispersion values for 75% of the pixels in each galaxy. The dashed horizontal line shows the imposed velocity dispersion cut-off (5.2km s^{-1}).

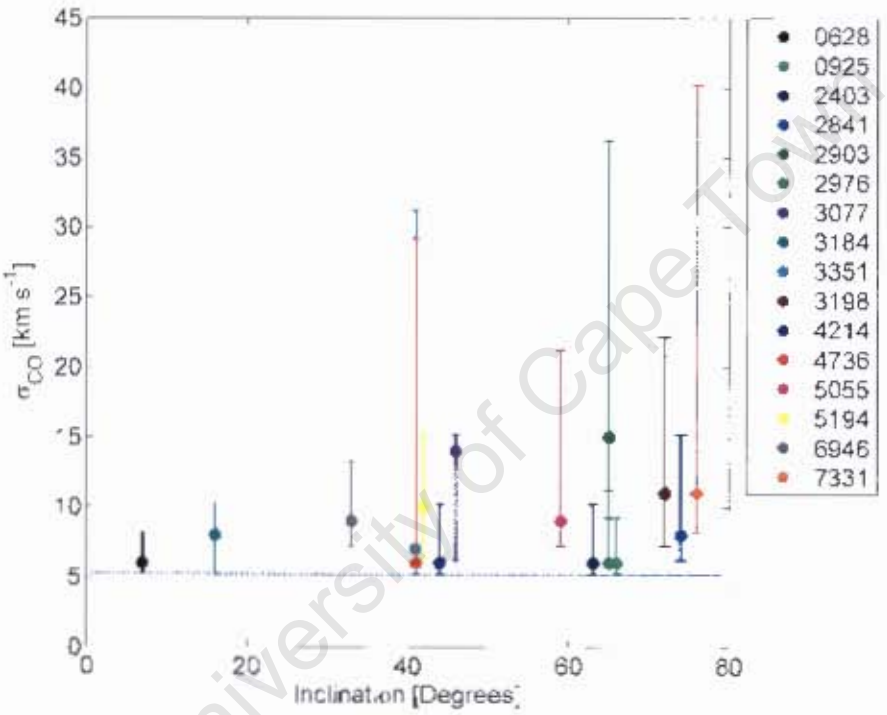

Figure 4.9: The CO dispersion (σ_{CO}) modes of the galaxies versus the inclinations of the galaxies. The error bars represent the ranges of CO dispersion values for 75% of the pixels in each galaxy. The dashed horizontal line shows the imposed velocity dispersion cut-off (5.2km s^{-1}).

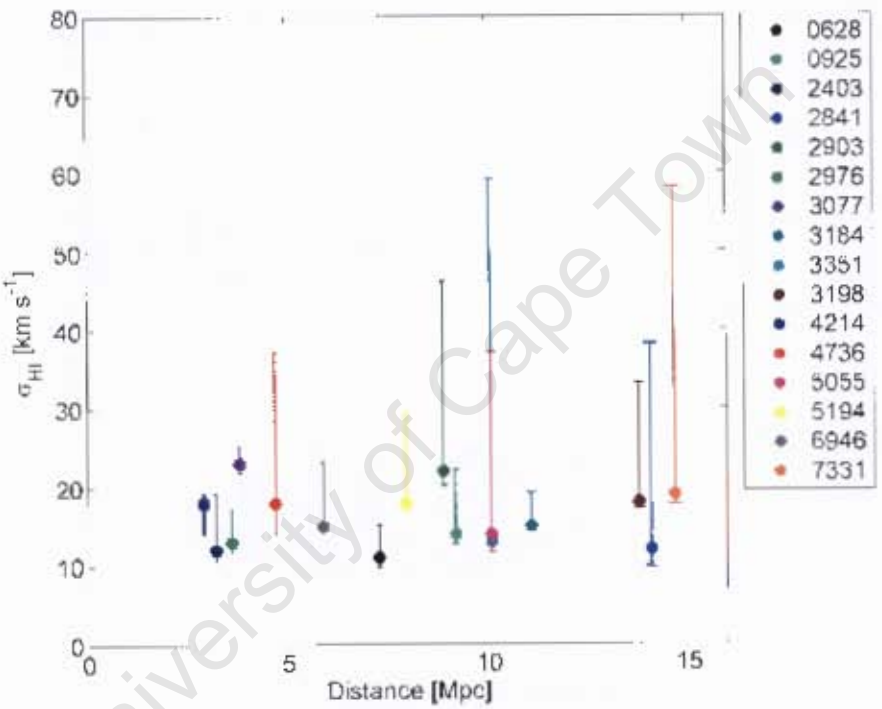

Figure 4.10: The HI dispersion (σ_{HI}) modes of the galaxies versus the distances of the galaxies. The error bars represent the ranges of HI dispersion values for 75% of the pixels in each galaxy.

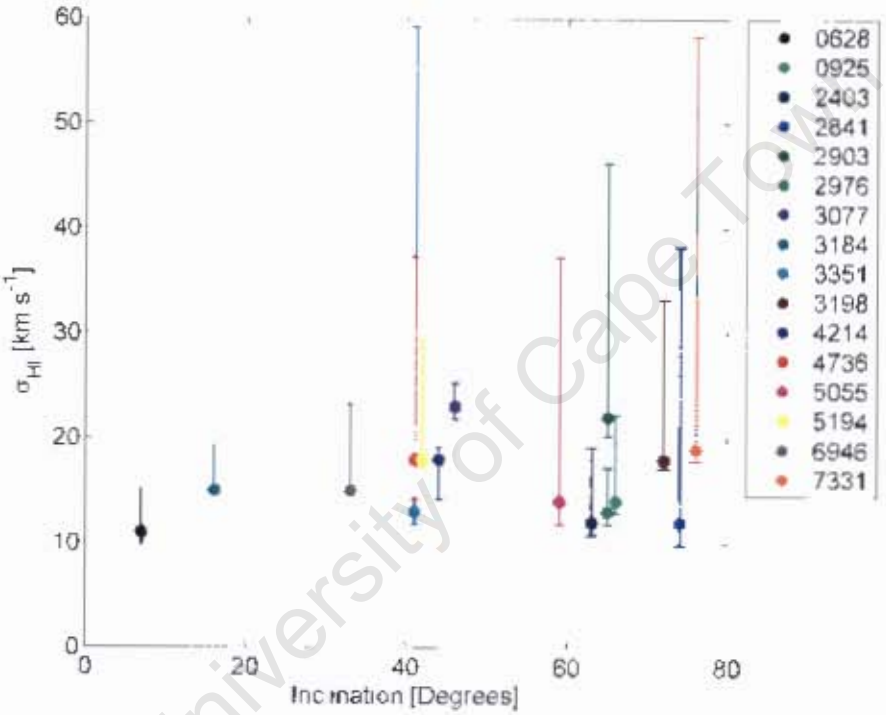

Figure 4.11: The HI dispersion (σ_{HI}) modes of the galaxies versus the inclinations of the galaxies. The error bars represent the ranges of HI dispersion values for 75% of the pixels in each galaxy.

Chapter 5

Individual Galaxies

In this Section we discuss some of the peculiar features in NGC 5055. NGC 3077 and NGC 6946.

5.1 NGC 5055

The $\sigma_{CO} - \sigma_{HI}$ map of NGC 5055 is very intriguing (Figure 5.1). There is an extended central structure where $\sigma_{CO} > \sigma_{HI}$, and an X-shaped structure surrounding the central region that culminates in two large lobes where $\sigma_{CO} - \sigma_{HI} \leq -25$ km s^{-1}. These features are found nowhere else in the galaxy at such large scales. These structures are found in the σ_{HI}/σ_{CO} map as well (see Fig.5.2). The central region (surprisingly) has $\sigma_{HI}/\sigma_{CO} \leq 1$. In the eastern (right) lobe the X-shaped structure is more prominent. When one looks at the distribution of σ_{HI} and σ_{CO} there are many pixels with high dispersions ($\sigma > 25$ km s^{-1}) and the abovementioned structures show up in the $\sigma_{CO} - \sigma_{HI}$ and σ_{HI}/σ_{CO} distribution histograms as asymmetric skewness ("tails") of the histograms towards high values.

To understand these regions it is necessary to look at the individual dispersions in the region. The velocity profiles from the central region show that the HI and CO have high dispersions. but interpreting any dispersions from the central regions of galaxies is fraught with uncertainty. It is not always clear whether the line of sight observations actually probe intrinsic dispersions and individual gas clumps/aggregates. There is more uncertainty in non-face-on galaxies like NGC5055 ($i = 59°$, from Table 2.2). NGC 5055 has a steep rotation curve in the inner regions (de Blok et al. 2008) and that combined with its inclination will result in higher levels of beam smearing and therefore more unphysical broadening of some of its velocity profiles. The profiles from the central region are very Gaussian in shape (see Figure 5.3). The profiles from the two lobe structures are very interesting (see Figures 5.5 and 5.4) - the HI profiles seem more distorted than the CO velocity profiles. The HI profiles have tails which lie in the directions opposite to where the gas is moving (or at least opposite to the motion of the main Gaussian peak). Even though the Gaussian fits are not as good as

the Hermite h_3 fits, for these highly distorted profiles the Gaussian fits describe the width of the profiles quite well.

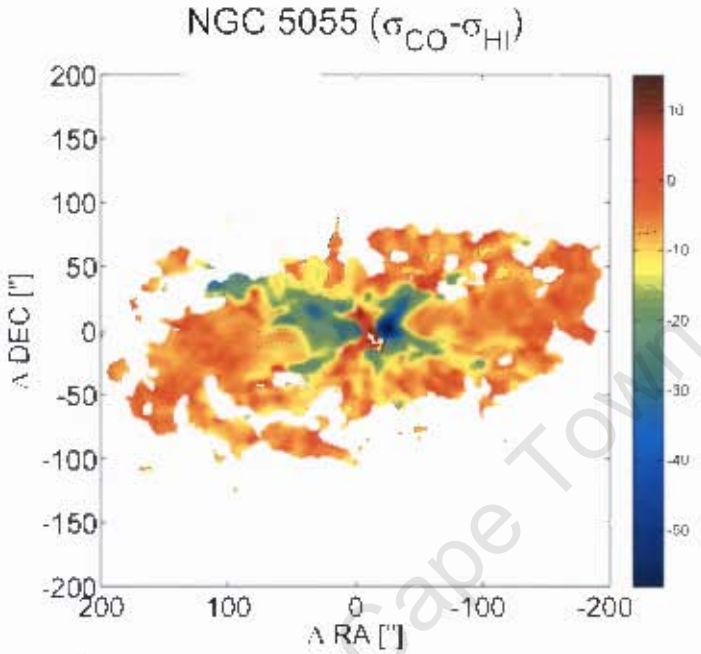

Figure 5.1: Plot of the dispersion difference $\sigma_{CO} - \sigma_{HI}$ in NGC 5055 (with the colourbar representing $\sigma_{CO} - \sigma_{HI}$ in $\mathrm{km\,s^{-1}}$).

Maps of σ_{HI} and σ_{CO} confirm that both the σ_{HI} and σ_{CO} are high in the central region (Figure 5.6). The plots indicate that the X-region also has high dispersions, the high dispersion areas of CO and to a lesser degree HI are correlated to the X-shaped structure in this region. The distinct lobes seem to be where the CO dispersions have decreased compared to the central regions, but the HI dispersions have not decreased by as much. Figure 5.7 is a plot of σ_{HI}/σ_{CO} overlaid with (FUV from *GALEX* archive) and 24 μm (from *Spitzer* archive) (which are star-formation tracers) contours. The plot shows that the two lobes are correlated with areas of high star formation.

NGC 5055 is a UV-bright LINER (Maoz 1996), with a peculiar non-point like bright UV source at the center (Maoz et al. 1995). The central region is known to be peculiar and has bright Hα continuum emission and a large fraction of pixels have two emission lines (Blais-Ouellette et al. 2004). When emission was separated into two different velocity components one component showed two regions of high peculiar velocities and the presence of a high intensity Hα counter-rotating disk or bipolar outflow was suggested by Blais-Ouellette et al. (2004). Pismis et al. (1995) and Afanasiev and Sil'chenko (2002) also found anomalous structures in the central regions that showed departures from the overall rotation of the galaxy. The Figure 5.5-5.6 velocity profiles show that there is HI and CO emission at high

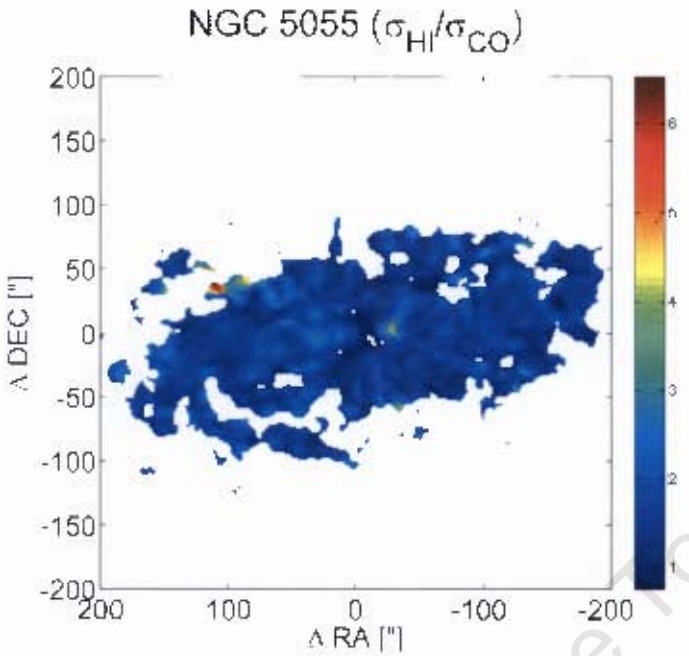

Figure 5.2: Plot of the dispersion ratio (σ_{HI}/σ_{CO}) in NGC 5055.

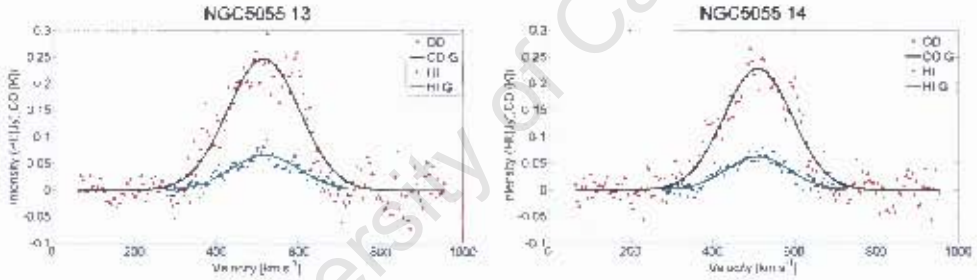

Figure 5.3: The CO and HI velocity profiles in the central region of NGC 5055 where $\sigma_{CO} \sim \sigma_{HI}$. The solid black and green lines are the Gaussian fits of the profiles.

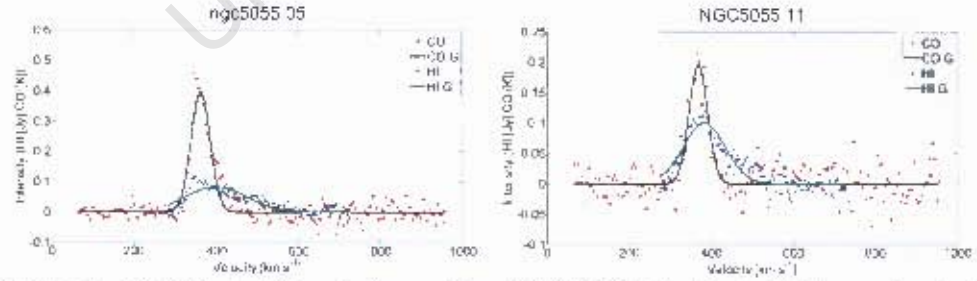

Figure 5.4: The CO and HI velocity profiles of NGC 5055 in the right lobe and extended region on the right where $\sigma_{CO} - \sigma_{HI} < -20$ km s^{-1}. The solid black and green lines are the Gaussian fits of the profiles. The plot on the left is one of the central region of the lobe and the plot on right is a profile from the upper part of the right part of the extended X-shaped region.

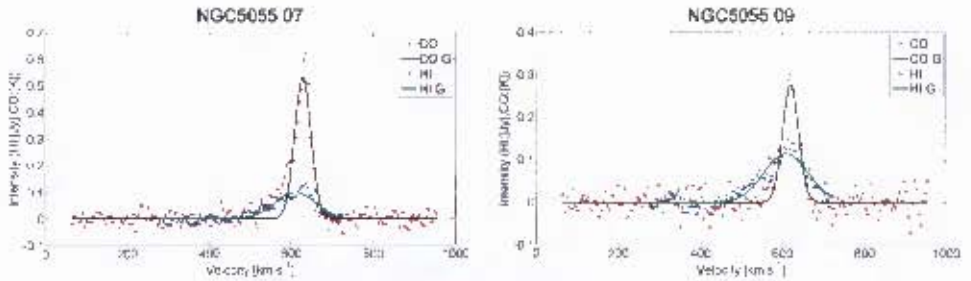

Figure 5.5: The CO and HI velocity profiles of NGC 5055 in the left lobe and extended region on the left where $\sigma_{CO} \quad \sigma_{HI} < 20$ km s $^{-1}$. The solid black and green lines are the Gaussian fits of the profiles. The left plot shows a profile from the central region of the lobe. The plot on the right shows a profile from the upper-left part of extended X-shaped region.

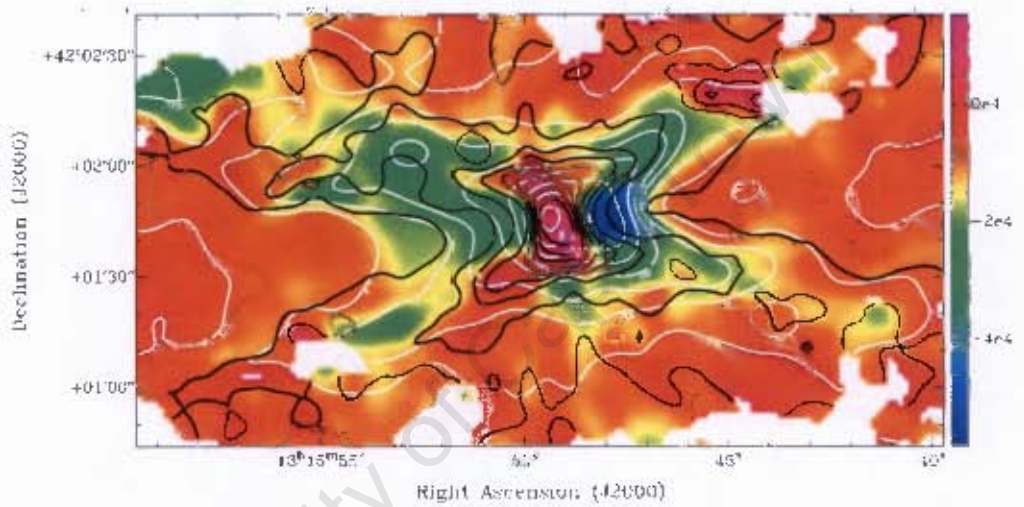

Figure 5.6: The dispersion difference $\sigma_{CO} \quad \sigma_{HI}$ in NGC 5055 overlaid with contours of σ_{HI} (white) and σ_{CO} (black). The colourbar is $\sigma_{CO} \quad \sigma_{HI}$ in units of m s $^{-1}$.

peculiar velocities, the HI having much wider velocity ranges than the CO (hence the higher dispersion). The shapes of the profiles are consistent with outflows but the X-structure that is seen in the maps does not seem to fit the bipolar outflow or counter-rotating disk hypotheses. Another interesting feature is that the HI is being affected more severely than the CO (profiles are more distorted than the CO) and because of this we see large dispersion difference regions in the maps..

5.2 NGC 3077

NGC 3077's dispersion difference map is peculiar because it shows two distinct regions of $\sigma_{CO} - \sigma_{HI}$ (see Figure 5.8). The histogram of the dispersions indicates that there are two populations of σ_{CO} in this galaxy but only a single σ_{HI} population. The CO dispersion map confirms the presence of two σ_{CO} populations. The populations are separate from each other and seem to be what causes the distinct regions of $\sigma_{CO} - \sigma_{HI}$. The cause of these

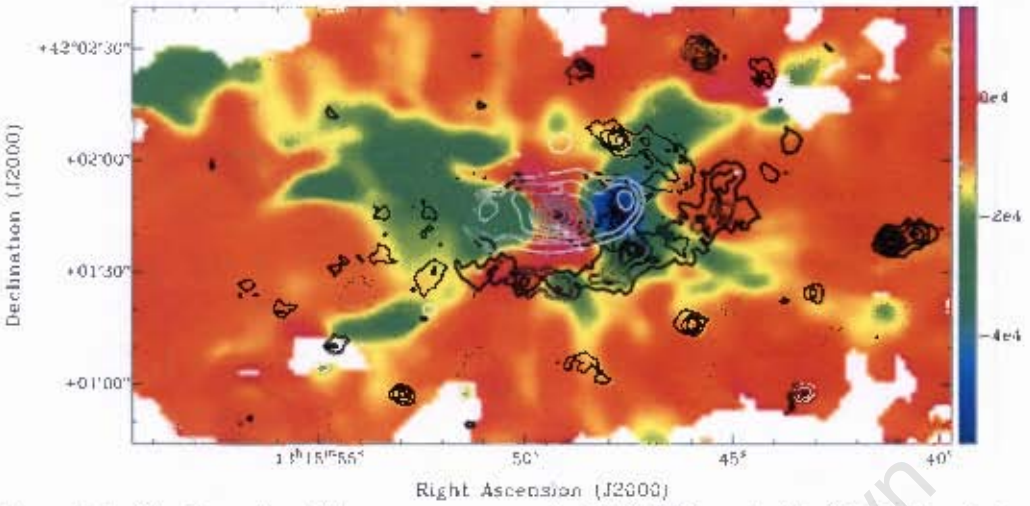

Figure 5.7: The dispersion difference $\sigma_{CO} - \sigma_{HI}$ in NGC 5055 overlaid with FUV emission (black contours) and 24μm emission (white contours). The colourbar is $\sigma_{CO} - \sigma_{HI}$ in units of ms^{-1}.

offsets therefore seems to lie in the CO. When the 24 μm emission (from *Spitzer* archive) is plotted over the dispersion differences (Figure 5.9) - we see that the dust emission is most intense in the large region, indicating a high star formation rate. The integrated intensities of the HI do not correlate with any of the regions (Figure 5.10), whereas the CO integrated intensities do correlate with the two regions (Figure 5.11), with the high 24 μm region having the highest intensity. From these plots it seems as though there are two distinct regions of CO which have different star formation rates, CO emission and dispersions.

NGC 3077 is an interacting dwarf galaxy and forms part of the M81 triplet, which is a system where three interacting galaxies are connected by tidal arms and tails (Cottrell 1977, van der Hulst 1979, Yun et al. 1994). NGC 3077 has an intensely star-forming core of bright Hα emission, soft X-ray emission and molecular gas (Price and Gullixson 1989, Bi et al. 1994, Becker et al. 1989). Extended star formation was found in the tidal tails as well (Walter et al. 2006). Figures 5.9 and 5.11 show that there is a higher fraction of high dispersion molecular gas in regions of high star formation and high CO gas density than in regions that do not have high star formation. This can be attributed to the large amounts of energy that are being pumped into the ISM due to the high star formation rate at the center of the galaxy.

5.3 NGC 6946

NGC 6946 also has an interesting dispersion difference map (see Figure 5.12). Like NGC 5055, there is a central region that has $\sigma_{CO} > \sigma_{HI}$. Unlike NGC 5055 however, this region extends to outside the center. There are extensions to the east and south-east of the center.

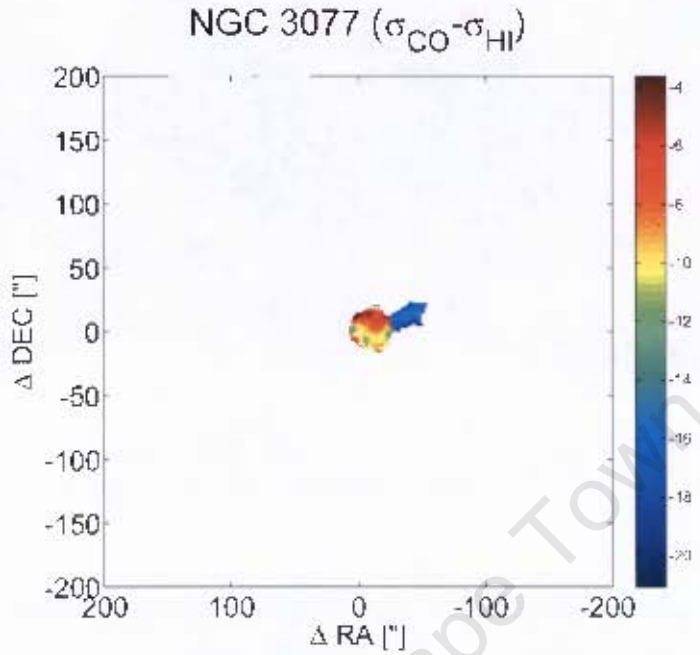

Figure 5.8: The dispersion difference $\sigma_{CO} - \sigma_{HI}$ in NGC 3077 (with the colourbar representing $\sigma_{CO} - \sigma_{HI}$ in $\mathrm{m\,s^{-1}}$).

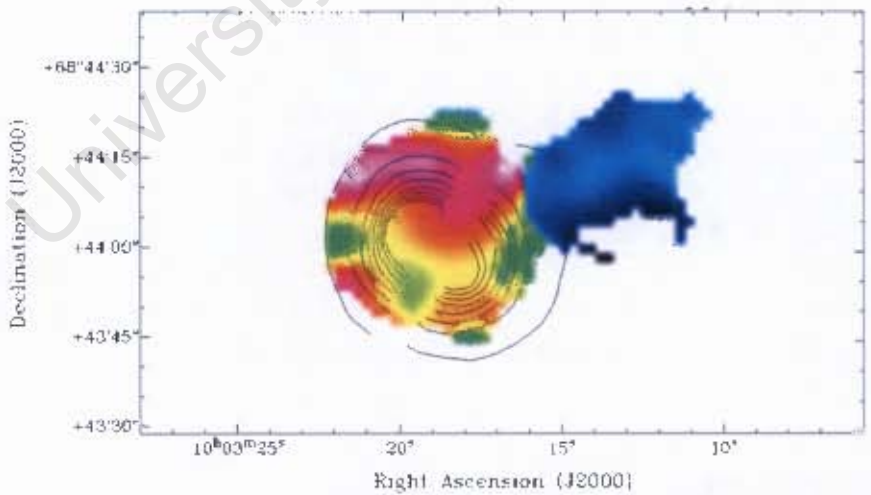

Figure 5.9: The dispersion difference $\sigma_{CO} - \sigma_{HI}$ in NGC 3077 overlaid with 24μm emission (black contours).

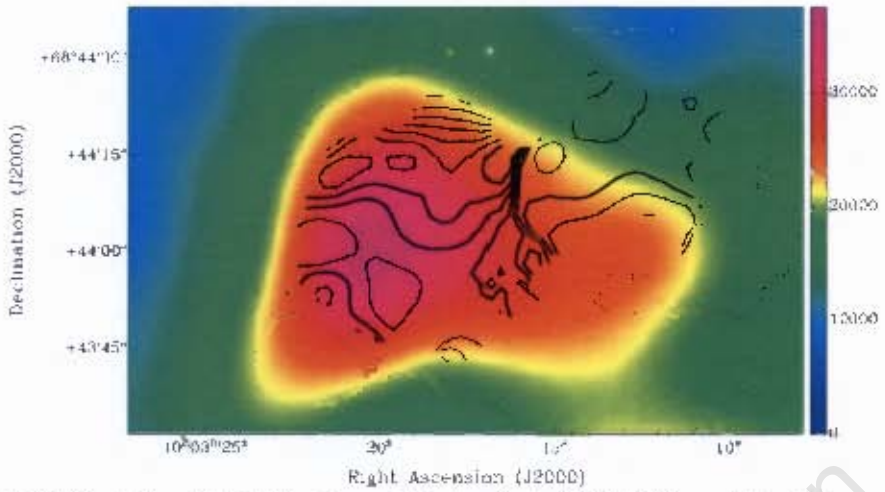

Figure 5.10: The integrated HI (in Jy m s^{-1}) intensity in NGC 3077 overlaid with $\sigma_{CO} - \sigma_{HI}$ (black contours).

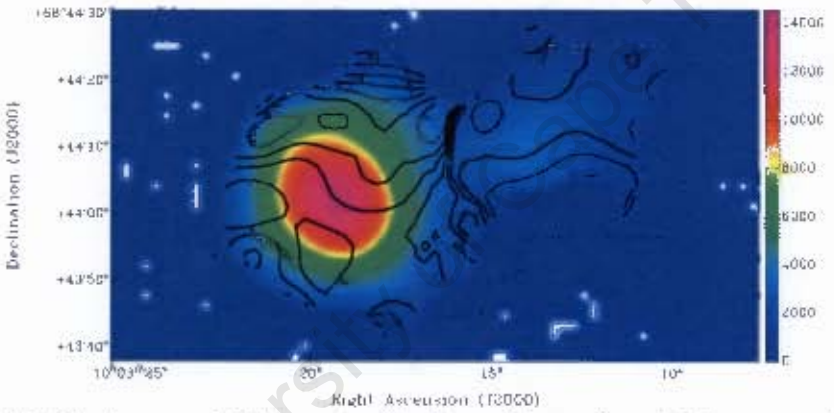

Figure 5.11: The integrated CO intensity (in K m s^{-1} beam^{-1}) in NGC 3077 overlaid with $\sigma_{CO} - \sigma_{HI}$ (black contours).

The representative profiles of the central and extended regions are shown in Figures 5.14 and 5.15. In the center the HI profiles are very asymmetric and there seems to be multiple components distinguishable from the velocity profiles; the CO profiles are very broad and also asymmetric (see Figure 5.14). The HI profiles have low signal-to-noise (S/N) and may not be real emission. The higher S/N profiles have multiple peaks, so the HI dispersions fitted in these regions cannot be trusted. This means that dispersion difference values are not a true indication of the dispersion difference in this region. If the low S/N HI is actual emission then it is still clear that the CO has a greater dispersion than the HI. The extended regions also have broad CO profiles (but not as broad as in the central regions), but both the HI and CO have more symmetric and single-peaked profiles than in the central regions. These regions have very low dispersion ratios (see Figure 5.13). Like NGC 5055 there are also regions with $\sigma_{CO} - \sigma_{HI} < -20$ km s^{-1} extending outwards from near the center, but in

NGC 6946 these only occur on the west side of the galaxy. The profiles from this extended region are shown in Figure 5.16. Unlike NGC 5055, the CO profiles are more asymmetric than the HI in the extreme areas of this region. In other areas further from the center both HI and CO profiles are symmetric and Gaussian.

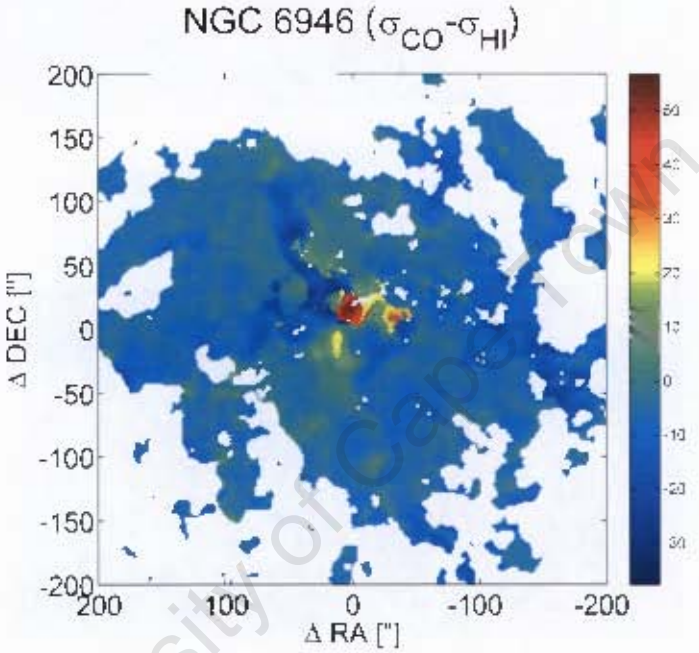

Figure 5.12: The dispersion difference $\sigma_{CO} - \sigma_{HI}$ in NGC 6946 (with the colourbar representing $\sigma_{CO} - \sigma_{HI}$ in kms^{-1}).

NGC 6946 has a high concentration of molecular gas in its central region and the central overdensity is extended along the minor axis of the galaxy into what is referred to as a molecular bar (e.g. Ball et al. 1985, Weliachew et al. 1988, Ishizuki et al. 1990). It also has a very high nuclear molecular gas concentration which coincides with a strong radio continuum source and bright HII region (Ishizuki et al. 1990). Israel and Baas (2001) found evidence for double-peaked CO emission in their observations of the central region of NGC 6946. They attributed this and the steep velocity gradients they found to a hole in the CO distribution at the center of NGC 6946. In our analysis: the central velocity profiles in Figure 5.14 also show hints of double-peaked CO emission. The minima of these double peaked profiles occur at similar velocities, Israel and Baas (2001) also found minima occuring at similar velocities. Therefore our results seem to provide further evidence for their theory of a central "hole". Some of the profiles (see Figure 5.15) show signs of "tails" and these could mean that the activity of the core is causing mild gas outflows near the center.

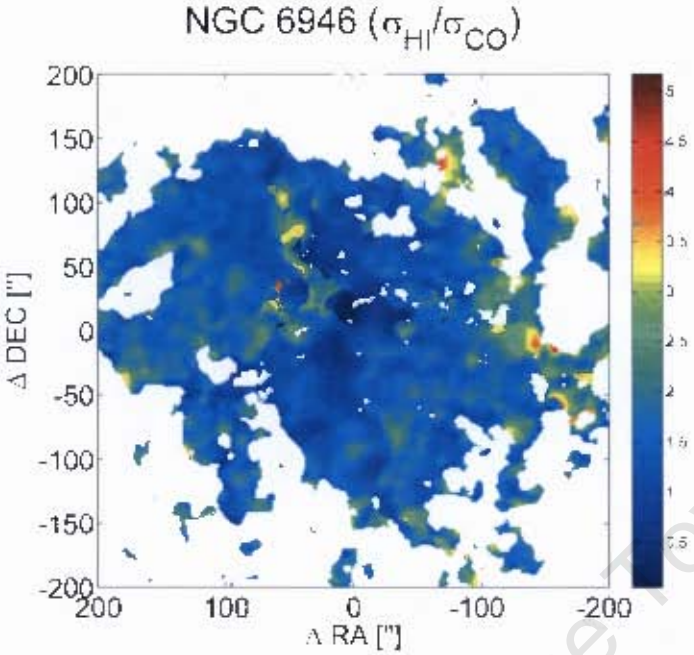

Figure 5.13: The dispersion ratio (σ_{HI}/σ_{CO}) in NGC 6946.

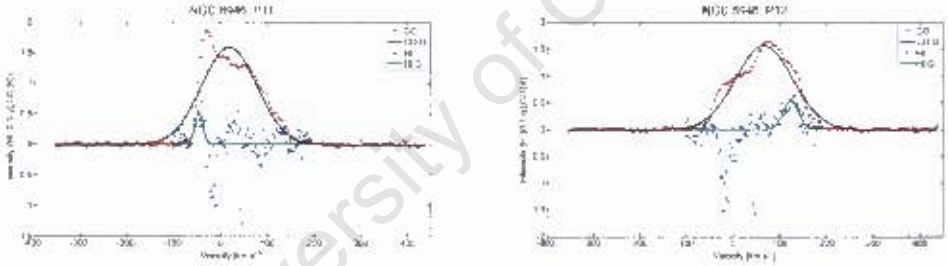

Figure 5.14: The CO and HI velocity profiles in the central region of NGC 6946, where σ_{CO} $>\sigma_{HI}$. The solid black and green lines are the Gaussian fits of the profiles.

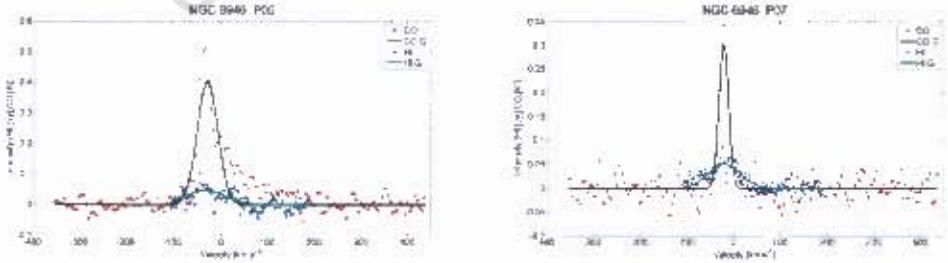

Figure 5.15: The CO and HI velocity profiles of NGC 6946 in the two extended regions in the East and South-East of the centor; where $\sigma_{CO} >\sigma_{HI}$. The solid black and green lines are the Gaussian fits of the profiles. The plot on the left is a profile from the region in the East and the plot on the right is of a profile from a South-East region.

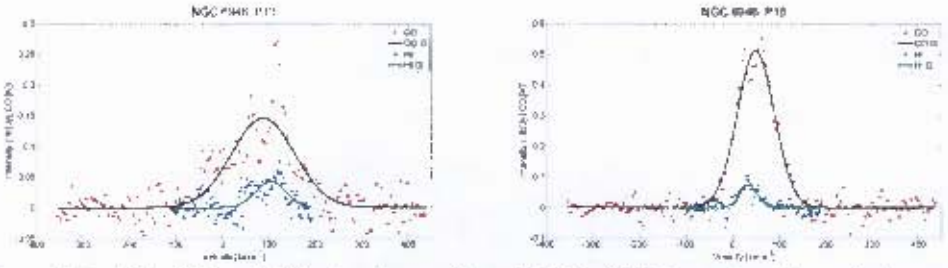

Figure 5.16: The CO and HI velocity profiles of NGC 6946 in to the West of the center; where $\sigma_{H2} - \sigma_{HI} < -20\,\mathrm{km\,s^{-1}}$. The solid black and green lines are the Gaussian fits of the profiles. The plot on the left is a profile near the center and the plot on the right is of a profile from the North-West extension of the region.

However, in a region that is similar to the X-structure in NGC 5055, the velocity profiles have different shapes to those found in NGC 5055 (see Figures 5.16 and 5.5). Therefore this structure is probably not due to the same processes as in NGC 5055. Some of the profiles this region are seemingly double-peaked, so the dispersions that were determined may not be a representation of the actual velocity dispersions of the gas in these regions. The reason for double peaked profiles in this region is still unclear.

Chapter 6

Discussion

6.1 Gaussian or Hermite?

Hermite h_4 fits have much higher σ_{error}/σ values than Gaussian distributions and Hermite h_3 fits do (see Figures 4.4 and 4.5). These errors are too large to allow for good analysis of the resulting dispersions to be made. As seen in Figures 4.3 and 4.2 most of the profiles in the galaxies are Gaussian in shape and can be fitted by Gaussians and Hermite h_3 polynomials. The reduced χ^2 values of the Gaussian and Hermite h_3 fits are similar. In the areas that have asymmetric profiles, Hermite h_3 fits fit the data better than Gaussians do. The definition of dispersion in these regions however is not clear because the broadening could be due to multiple cloud components, turbulence, non-standard motions, rotation etc. Gaussians distributions generally fit most of the data well and have small dispersion uncertainties and are therefore sufficient for use in this analysis.

6.2 What do the dispersions mean?

Our analysis considers scales of 200 pc to 1 kpc. At these scales a single beam contains multiple GMCs; therefore the major contribution to the measured CO dispersion is the cloud-cloud dispersion. Due to uncertainties in the assumptions required to estimate the internal velocity dispersion of molecular clouds we use the measured dispersions as the upper limit for cloud-cloud dispersions in the galaxies. Some HI and CO velocity profiles in some of the galaxies (e.g. NGC 5055 and NGC 6946) are very asymmetric and in many galaxies the central regions have unphysically large dispersions. The broad dispersions may be caused by the steep rotation curves in the central regions resulting in unphysical broadening due to clumps of gas in the same beam having very different rotation velocities. The presence of multiple gas components in the line of sight in these central regions could also be causing the apparently broad profiles.

From Section 4.3 it seems that the increase in scale from 200 pc to 1 kpc has little effect

on the observed dispersions. At higher inclinations the contribution of rotation and planar turbulence on the observed velocity dispersions increase; these cause broadening of the velocity profiles. The "tails" (towards higher dispersions) in the dispersion distributions seem to get larger with increasing inclination. The galaxies with inclinations greater than 70 degrees had large "tails". This is seen in Figures 4.9 and 4.11 where the fraction of galaxies with large velocity dispersion ranges ($\geq 15\,\mathrm{km\,s^{-1}}$) increase with increasing inclination. This however, is a tentative conclusion because comparisons of the dispersions versus inclination were inconclusive. A larger sample of galaxies will be required to verify this.

6.3 HI and CO Dispersions

The expected dispersion due to thermal broadening of HI is $\sim 8\,\mathrm{km\,s^{-1}}$ and of CO $\sim 0.5\,\mathrm{km\,s^{-1}}$. The σ_{HI} values in our galaxies are $\sim$ 8-30 $\mathrm{km\,s^{-1}}$. This is larger than the values expected from thermal broadening and also larger than what Tamburro et al (2009) found. Our dispersion values are from the inner regions of galaxies where there is sufficiently strong CO emission (we used a 4σ noise cut-off). These regions have high star formation rates. Studies have shown that velocity dispersions are high in the central regions of galaxies and decline with radius (e.g. Kamphuis and Sancisi 1993, Petric and Rupen 2007, Tamburro et al. 2009). In Section 3.2 (see Figures 3.9 and 3.10) the radial dispersion trends for two galaxies are shown, plots for the other galaxies are in the Appendix (we did not have star formation maps for NGC 2903 and so we did not create a similar plot for it). It is clear from these that σ_{HI} and σ_{CO} decline with radius from the centers of galaxies. They however, do not decline to the same values, indicating that there is always a dispersion difference between HI and CO in galaxies (even in the outer regions of the CO disk). It is no surprise that our measured HI dispersions are higher than the average dispersions over the entire galaxies, because regions where HI and CO overlap are in the inner parts of galaxies, and HI has high dispersion values in the inner regions of galaxies (Tamburro et al 2009). Our velocity resolution cut-offs (usually $< 5.2\,\mathrm{km\,s^{-1}}$) mean that we are only exploring the high dispersion and warm CO (since we are studying the CO($J = 2 - 1$) line). From our dispersion maps it is clear that there is a lot of emission from the CO($J = 2 - 1$) line in the inner regions of most of the galaxies we analysed (NGC 925, NGC 3077 and NGC 4214 are the exceptions). Our range of CO dispersions is $5.2\,\mathrm{km\,s^{-1}}$ (due to the dispersion cut-off) to $25\,\mathrm{km\,s^{-1}}$ and this is consistent with Wilson et al. (2011) values (found using the CO($J = 3 - 2$) line: $2.7 - 20\,\mathrm{km\,s^{-1}}$, with $0.43\,\mathrm{km\,s^{-1}}$ velocity resolution).

The mean $\sigma_{CO} - \sigma_{HI}$ was found to be $-7.2 \pm 1.3\,\mathrm{km\,s^{-1}}$ (with NGC 3077 and NGC 2841 excluded in the mean calculation, see Section 3.1 and Table 3.2), and the ratio between the two was found to be $\sigma_{HI}/\sigma_{CO} = 1.54 \pm 0.18$. This is consistent with what Wilson et al. (2011) found ($\sigma_{HI}/\sigma_{CO} \sim 2$) in their analysis. This confirms that HI dispersions are greater than CO dispersions. CO and HI dispersions are both larger than the expected dispersion due to thermal broadening.

The σ_{HI}/σ_{CO} and $\sigma_{CO} - \sigma_{HI}$ maps show that there is a lot of structure in the galaxies. This indicates that in small local scales the ratio and difference between σ_{HI} and σ_{CO} is highly affected by local processes that pump kinetic energy into ISM, affect the movement of gas and affect σ_{HI} and σ_{CO} in different ways. In some of the galaxies distinct large scale structures appear. These usually appear in the centers of galaxies (NGC 5055, NGC 6946, NGC 4736, NGC 7331, NGC 3351) and around the centers like in (NGC 5055 and NGC 6946). These indicate that large scale features and processes may be affecting gas in these regions compared to other regions in the galaxies. In the irregular or interacting galaxies such as (NGC 3077, NGC 4214, NGC 4736) there are also structures that may be related to interactions, starbursts and other dynamical effects due to the non-disk structure and interactions with other galaxies.

6.4 Dispersions and Star Formation

σ_{CO}, σ_{HI}, and $\Sigma_{\rm SFR}$ have similar exponential radial trends, and CO seems better correlated to $\Sigma_{\rm SFR}$ the radial trends, but quantification of correlation was not covered in this thesis. Figure 3.16 shows that for low $\Sigma_{\rm SFR}$ ($\Sigma_{\rm SFR} \leq 10^{-2.6}\,{\rm M}_\odot\ {\rm yr}^{-1}\ {\rm kpc}^{-2}$) CO dispersions do not normally go above $10\,{\rm km\,s}^{-1}$. At higher $\Sigma_{\rm SFR}$ values the dispersion increases with increasing $\Sigma_{\rm SFR}$, and for $\Sigma_{\rm SFR}$ between $10^{-2.6}$ and $10^{-1.5}\,{\rm M}_\odot\,{\rm kpc}^2\,{\rm yr}^{-1}$. There is a strong correlation between $\log\Sigma_{\rm SFR}$ and σ_{CO} in this regime, the correlation decreases at higher $\Sigma_{\rm SFR}$ values. HI dispersions are very scattered for $\Sigma_{\rm SFR} \leq 10^{-2.6}\,{\rm M}_\odot\ {\rm yr}^{-1}\ {\rm kpc}^{-2}$ and they exhibit little or no correlation with $\Sigma_{\rm SFR}$. At higher $\Sigma_{\rm SFR}$ values σ_{HI} values have less scatter and there is a clearer correlation with $\Sigma_{\rm SFR}$. There is also a lot of scatter and no clear correlations between σ_{HI}/σ_{CO} and $\Sigma_{\rm SFR}$ when $\Sigma_{\rm SFR} \leq 10^{-2.6}\,{\rm M}_\odot\ {\rm yr}^{-1}\ {\rm kpc}^{-2}$. There is a clear anti-correlation between σ_{HI}/σ_{CO} and $\Sigma_{\rm SFR}$ for $\Sigma_{\rm SFR}$ between $10^{-2.6}$ and $10^{-1.5}\,{\rm M}_\odot\ {\rm yr}^{-1}\ {\rm kpc}^{-2}$. This suggests that the slope of σ_{CO} is greater than the σ_{HI} slope in this regime. When the above analysis was performed for all HI dispersions above the noise and dispersion cut-offs, the correlation between $\Sigma_{\rm SFR}$ and σ_{HI} was found (see Figure3.17). The correlation was found across the entire range of $\Sigma_{\rm SFR}$ used in the analysis. There were gradient changes in the σ_{HI} versus $\Sigma_{\rm SFR} \geq 10^{-2.6}\,{\rm M}_\odot\ {\rm yr}^{-1}\ {\rm kpc}^{-2}$ curves at the threshold values mentioned above.

This behaviour indicates that $\Sigma_{\rm SFR} \sim 10^{-2.6}\,{\rm M}_\odot\ {\rm yr}^{-1}\ {\rm kpc}^{-2}$ may be a threshold value below which the trends with dispersion are either weak or non-existent. This maybe due to the star formation rate not supplying sufficient energy to the ISM to drive dispersions or that the efficiency of the energy transfer from star formation to the gas is low. Above this "threshold" value the dispersion is much better correlated with $\Sigma_{\rm SFR}$ than below it. The energy transfer or transfer efficiency in this regime may be enough to allow star formation to effectively drive the gas velocity dispersions. Tamburro et al (2009) found that kinetic energy is proportional to the star formation of the gas, and our result is consistent with that.

The problems that were mentioned earlier about interpreting the velocity dispersions, where they come from and the effects of inclination could all have an effect on the above-mentioned correlations. Problematic profiles are in the minority and would not have a large effect on the correlations due to the averaging that was done. Most of these profiles would have large errors (signs of these are seen in some of the points in Figure 3.13), and identifying them would be simple. In the areas of the plots where there are correlations, most of the average dispersions have small errors, so the effect of those kinds of profiles is not very large. NGC 925, NGC 3077 and NGC 4214 do not have many pixels and if they are excluded from the analysis the trends still hold. Unphysically large dispersions with values larger than $30-40\,\mathrm{km\,s^{-1}}$ (CO and HI cases, found in some of the galaxy centers e.g. NGC 3198, NGC 3198 3351, NGC 4736, NGC 5055, NGC 6946, NGC 7331), usually lie above $\Sigma_{\mathrm{SFR}} \sim 10^{-1.5}\,\mathrm{M_\odot\ yr^{-1}\ kpc^{-2}}$. In this regime we do still see some correlation, but not as strong as in the $10^{-2.5}$ to $10^{-1.5}\,\mathrm{M_\odot\ yr^{-1}\ kpc^{-2}}$ regime. Some galaxies do not show any correlation and some have anti-correlations between dispersion and $\Sigma_{\mathrm{SFR}} \geq 10^{-2.6}\,\mathrm{M_\odot\ yr^{-1}\ kpc^{-2}}$. Bigiel (2008) found a "kink" in the combined $\log\Sigma_{\mathrm{SFR}}$ versus $\log\Sigma_{\mathrm{HI+H_2}}$ plot from all the nearby galaxies in their sample (which was a subset of the THINGS sample). This gradient change occurs near $\Sigma_{\mathrm{SFR}} \geq 10^{-2.6}\,\mathrm{M_\odot\ yr^{-1}\ kpc^{-2}}$, they also found a "kink" when they considered data from other surveys. Their "kink" was identified at $\Sigma_{\mathrm{gas}} \sim 9\,M_\odot\,\mathrm{kpc^{-2}}$ and was attributed saturation of HI. We find evidence for a threshold in the CO and HI.

6.5 Conclusion

The aim of the thesis was to compare HI and CO velocity dispersions in nearby galaxies. These velocity dispersions are important for understanding turbulence, dynamics and star formation in galaxies. HI dispersions have been extensively used to study these, but in areas where molecular gas is dominant it is also important to study the molecular gas dispersions. Data from high resolution and high sensitivity nearby galaxy surveys were used and the velocity dispersions of the galaxies in these surveys were determined. Pixel-by-pixel analysis and comparisons of the CO and HI velocity dispersions were made. The relationship between the star formation rate and velocity dispersions was also analysed. Both HI and

CO velocity dispersions are greater than the expected dispersions from thermal broadening, and they decline with increasing radius. There is evidence that the range of dispersions found in the galaxies increases with increasing inclination. There is little evidence for the modes of the dispersions changing with inclination.
The mean $\sigma_{CO} - \sigma_{HI}$ was found to be $7.2 \pm 1.3\,\mathrm{km\,s^{-1}}$ and $\sigma_{HI}/\sigma_{CO} = 1.5 \pm 0.18$.
There is a correlation between HI and CO velocity dispersions and the star formation rate density, for $\Sigma_{\mathrm{SFR}} \geq 10^{-2.6}\,\mathrm{M_\odot\ yr^{-1}\ kpc^{-2}}$; and σ_{HI}/σ_{CO} is anti-correlated with the star formation rate density in the same regime.

6.6 Future

The only gas component that is missing in the analysis is the ionized gas. Therefore the next step in the analysis is to compare the HI and CO with Hα velocity dispersions of the galaxies in the sample. We will be doing this comparison very soon. The major limitation of the CO data was the dispersion cut-off, therefore future analysis with higher velocity resolution will need to be done so that low dispersion molecular gas can also be studied. Higher velocity resolution observations will also allow for good studies of velocity profile shapes in both CO and HI. ALMA will revolutionize molecular gas studies because its orders of magnitude impovements in sensitivity will allow us to probe very low column density regimes of CO and possibly find molecular gas in environments where it is not expected to exist. This will allow us to better understand the links between molecular gas, atomic gas and star formation.

References

Afanisiev V.L. and Sil'chenko O.K. 2002, *A&A* 388, 461

Agertz O. et al. 2009, *MNRAS* 392, 1 : 294 – 308 ,arXiv: 0810.1741v2

Ball R. et al. 1985, *ApJL* 298 *L*21

Becker R., Schilke P., Henkel C. 1989, *A&A*, 35, 463

Begeman K. 1987, PhD thesis, University of Groningen

Bertin G. 1996, in Block D.L., Greenberg J.M., eds, New Extragalactic Perspectives in the New South Africa. Kluwer, Dordrecht, p.227

Bertin G. and Lin C.C. 1996, Spiral Structure in Galaxies :A Density Wave Theory. MIT Press, Campbridge, MA

Bi H.G., Arp H. and Zimmermann H.U. 1994, *A&A*, 282, 386

Bianchi L. et al. 2003, *AAS* 203, 9112

Bigiel F. et al. 2008, *ApJ* 136 : 2846

Bigiel F. et al. 2010, *AJ* 140, 1194

Blaise-Ouellette S., Philippe A. and Carignan C. 2001, *AJ* 121, 1952

Blitz L. et al. 2007, , *Protostars and Planets V* 81 – 96

Bloemen J.B.G.M. et al 1984, *A&A* 139, 37

Bloemen J.B.G.M. et al. 1986, *A&A* 154, 24

Bosma A. 1981, *AJ* 86, 1791*B*

Bosma A. 1981, *AJ* 86, 1825*b*

Bosma A. 1983, *IAUS* 100, 11*B*

Braine J. and Combes F. 1993, *A&A* 267 7

Braine J. et al 1993, *A&A* 97 887

Braun R. 1995, *A&A* 114 409

Brinks E. and Bajaja E. 1986, *A&A* 169 14

Burgers J.M. 1974, *Acoust. Soc. Am. J.* 55 50

Burkert A. 2006, *Comptes Rendus Physique* 7 433

Burton M.G., Hollenbach D.J. and Tielens A.G.G. 1992, *ApJ* 399 563*B*

Carruthers G. 1970, *ApJL* 161 *L*81

Casoli F. et al 1998, *A&A* 331 451

Cayatte V., van Gorkom J.H., Balkowski C. and Kotanyi C. 1990, *AJ* 100 604

Clemens D.P. 1985, *ApJ* 295 422

Combes F. and Becquaert J.-F. 1997, *A&A* 326, 554
Cottrell G.A. 1977, *MNRAS*, 178, 577
Dame T.M. and Thaddeus P. 1985, *ApJ* 297, 751
de Blok W.J.G. and Walter F. 2002, *ApJ* 537, *L*95
de Blok W.J.G. et al. 2008, *AJ* 136 2648
Dib S., Bell E. and Burkert 2006, *ApJ* 638, 797
Dickman R.L., Snell R.L. and Schloerb F.P. 1986, *ApJ* 309 326
Eddington A.S. 1937, *Obs* 60 99*E*
Elmegreen B.G. 1989, *ApJ* 338, 178
Elmegreen B.G. 1995, *ApJ* 275, 944
Elmegreen B.G. 1999, in Star Formation 1999, ed. T. Nakamoto (Nagano : Nobeyama Radio Obss),3
Elmgreen B.C. and Scalo J. 2004,*Annu. Rev. Astron. Astrophys.* 42 : 211
Engargiola G., Plambeck R.L., Rosolowsky E. and Blitz L. 2003, *ApJS* 149 343
Ewen H.I. and Purcell E.M 1945, *Nature* 168, 351
Ferguson A.N.M., Wyse R.F.G., Gallagher J.S. and Hunter D.A. 1998, *ApJ* 506, *L*19
Frisch U.(ed.) 1995, Turbulence. The legacy of A.N. Kolmogorov (Cambridge: Cambridge Univ Press)
Fukui Y. et al 1999, *PASJ* 51 754
Gammie C.G., Ostriker J.P. and Jog J.P. 1991, *ApJ* 378 565
Glover S.C.O 2003, *ApJ* 584 331
Gold T. 1961, *Mem. Soc. R. Sci. Liege* 20 467
Gould R.J. and Saltpeter E.E. 1963, *ApJ* 138 393
Grenier I.A., Casandjian J., and Terrier R. 2005, *Science* 307 1292
Heckman T.M., Blitz L., Wilson A.S., Armus L., and Miley G.K. 1989, *ApJ* 342, 735
Helfer T.T. et al 2003, *ApJS* 145 259
Henebelle P. and Audit E. 2007, *A&A* 465, 431
Hunter D.A., Elmegreen B.G. and Baker A.L. 1998, *ApJ* 493, 595
Ishizuki S. et al 1990, *ApJ* 355 436
Israel F.P. et al. 1984, *A&A* 134 396
Israel F.P. and Baas F. 2001, *A&A* 371 433
Jannuzi B.T., Black J.H., Lada C.J. and van Dishoeck E.F. 1988, *ApJ* 332 995
Jog C.J. and Ostriker J.P. 1988, *ApJ* 328 404
Jog C.J. 1996, *MNRAS* 278 209
Kenney J.D.P. and Young J.S. 1988, *ApJ* 326, 588
Kennicutt R.C. 1989, *ApJ* 344, 658
Kennicutt R.C. 1998, *ApJ* 498, 541
Kim S., Dopita M.A., Staveley-Smith L. and Bessell M.S. 1999, *AJ* 118, 2797
Knapp G.R. and Jura M. 1976, *ApJ* 209 782 – 792
Kopp M., Gerin M., Roueff E. and Le Bourlot J. 1996, *A&A* 305 558 – 571
Krumholz M.R. and McKee C.F. 2005, *ApJ* 630, 250

Krumholz M.R., Leroy A.K. and McKee C.F. 2011, *ApJ* 731, 25
Kuno N. et al 2007, *PASJ* 59 117
Larson R.B. 1981, *MNRAS* 194, 809 - 826
Lebrun F. et al 1983, *ApJ* 274, 231
Leroy A.K. et al. 2009, *ApJ* 137 : 4670
Leroy A.K. et al. 2008, *ApJ* 136 : 2782
Liszt H.S. 1997, *A&A* 322 962 – 974
Low F.J. et al. 1984, *ApJ* 278, *L*19 – 22
Mac Low M.-M. and Klessen R.S. 2004, *RevModPhys* 76, 125
Madore B.F. 1977, *MNRAS* 178, 1
Maloney P. and Black J.H. 1988, *ApJ* 325, 389
Maoz D. et al. 1995, *ApJ* 440, 91
Maoz D. 1996, *ASPC* 103, 90
Martin C.L. and Kennicutt R.C. 2001, *ApJ* 555, 301
McKee C.F. and Ostriker J.P. 1977, *ApJ* 218, 148
McKee C.F. Ostriker E.C. 2007, *Ann. Rev. Astron. Astrophys.* 45, 565
Meurer G.R., Carignan C., Beaulieu S.F. and Freeman K.C. 1996, *AJ* 111, 1551
Miller C.A. and Oort J.H. 1951, *Nature* 168, 357
Passot T., Pouquet A. and Woodward P. 1988, *A&A* 197, 228
Piontek R.A. and Ostriker E.C. 2004, *ApJ* 601, 905
Pismis P., Mampaso A., Mnateiga M., Recillas E. and Cruz Gonzalez G. 1995, *AJ* 109, 140
Price J.S. and Gullixson C.A. 1989, *ApJ*, 337, 658
Puche D. and Carignan C. 1991, *ASPC* 18, 155*P*
Rafikov R.R. 2001, *MNRAS* 323, 445
Rickard L.J., Palmer P., Morris M., Zuckerman B., and Turner B.E. 1975, *ApJ* 199 75
Roman-Duval J. et al 2011, *ApJ*, 740, 120
Romeo A.B. and Wiegert J. 2011, *MNRAS* 416, 1191
Safranov V.S. 1960, *Ann. d'Astrophys.* 23, 979
Sakamoto K. et al 1995, *ApJS*, 100, 125
Sakamoto K., Okumura S.K., Sumio I. and Scoville N.Z. 1999, *ApJS*, 124, 403
Sage L.J. 1993, *A&A*, 272, 123
Sanders D.B., Scoville N.Z. and Solomon P.M. 1985, *ApJ* 289 373
Schaye J. 2004, *ApJ* 609, 667
Schmidt M. 1959, *ApJ* 129, 243
Schruba A. et al. 2011, *AJ* 142, 37
Shen Y. and Lou Y.-Q. 2003, *MNRAS* 345, 1340
Shetty R. et al 2011, *MNRAS* 415, 3253
Shull M. and Beckwith S. 1982, *Annu. Rev. Astrophys.* 20 163 – 190
Skillman E.D. 1987, Star Formation in Galaxies, ed. C.J. Lonsdale Persson (Greenbelt, MD: NASA), 263
Smith A.M. and Stecher T.P. 1971, *ApJ* 164 43

Snow T.P. and McCall B.J. 2006, *Annu. Rev. Astrophys.* 44 367 – 414
Solomon P.M., Rivolo A.R., Barrett J., and Yahil A. 1987, *ApJ* 319 730
Solomon P.M. and Sage L.J. 1988, *ApJ* 334 613
Solomon P.M. and de Zafra R. 1975, *ApJ* 199 79
Stark A.A. and Brand J. 1989, *ApJ* 339 763
Staveley-Smith L. et al 1997, *MNRAS* 289 225
Sternberg A. and Dalgarno A. 1995, *ApJS* 99 565
Strömgren B. 1939, *ApJ* 89 526
Tasker E.J. and Tan J.C. 2009, *ApJ* 700 358
Tamburro D. et al 2009, *AJ* 137 4424
Thomasson M., Donner K.J. and Elmegreen B.G. 1991, *A&A* 250 316
Thornley M.D. and Wilson C.D. 1995, *ApJ* 447, 616
Tielens A.G.G.M, Hollenbach D. 1985, *ApJ* 291 722
Tielens A.G.G.M, Hollenbach D. 1985, *ApJ* 291 747
Toomre 1964, *ApJ* 139, 1217
van Dishoeck E.F. and Black J.H. 1988, *ApJ* 334 771
van de Hulst H.C. 1945, *Ned. Tijdschr. Natuurkd.* 11, 210
van der Hulst J.M. 1979, *A&A*, 75, 97
von Hoerner S. 1951, *Z. Astrophys.* 30, 17 – 64
von Weizsäcker 1951, *ApJ* 114, 165 – 186
Wada K., Meurer G., Norman C.A. 2002, *ApJ*, 577, 197
Wada K. and Norman C.A. 2007, *ApJ*, 660, 276
Walsh W. et al 2002, *A&A*, 388, 7
Walter F. and Brinks E. 1999, *AJ*, 118, 273
Walter F. and Brinks E. 2001, *AJ*, 121, 3026
Walter F. et al 2001, *AJ*, 121, 727
Walter F., Martin C., and Ott J. 2006, *AJ*, 132, 2289
Walter F. et al. 2008, *AJ* 136 : 2563
Wang B. and Silk J. 1994, *ApJ*, 427, 759
Weliachew L., Casoli F., and Combes F. 1988, *Astr. Ap.* 134 396
Wevers B.M.H.R., van der Kruit P. C. and Allen R.J. 1986, *AAS* 66 4
Wilson C.D. and Scoville N. 1990, *ApJ* 363 435
Wilson C.D. 1995, *ApJ* 448 *I*.97 – *I*.100
Wilson C.D. et al. 2011, *MNRAS* 410 1409
Wolfire M.G., Hollenbach D., and McKee C.F. 2010, *ApJ* 716 1191
Wong T. and Blitz L. 2002, *ApJ* 569, 157
Young J.S. and Knezek P.M. 1989, *ApJ* 347 55
Young J.S. et al 1995, *ApJS* 98, 219
Young J.S., Allen L., Kenney J.D.P., Lesser A., and Rownd B. 1996, *AJ* 112, 1903
Yun M.S., Ho P.T.P., Lo K.Y. 1994, *Nature*, 372, 530

Appendix

NGC 628

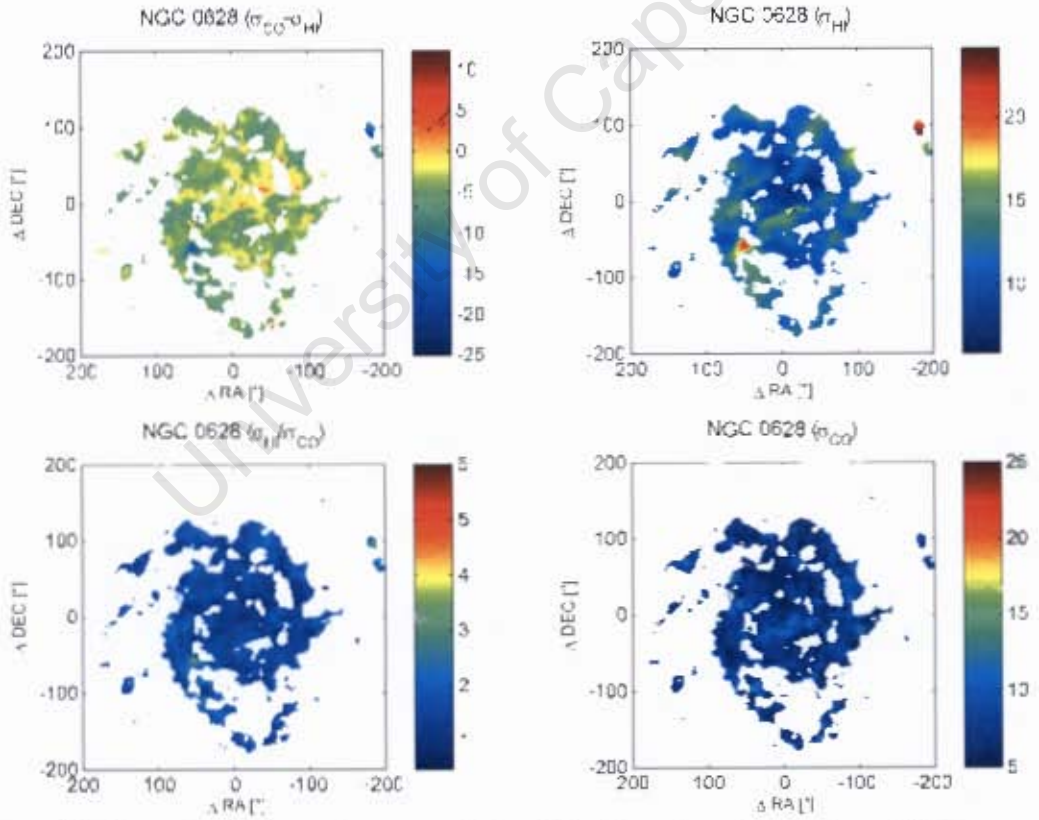

Figure A1: Dispersion difference ($\sigma_{CO} - \sigma_{HI}$) (top left), dispersion ratio (σ_{HI}/σ_{CO}) (bottom left), CO dispersion (bottom right) and HI dispersion (top right) maps of NGC 628. The colourmap values of the dispersion plots are in units of km s^{-1}.

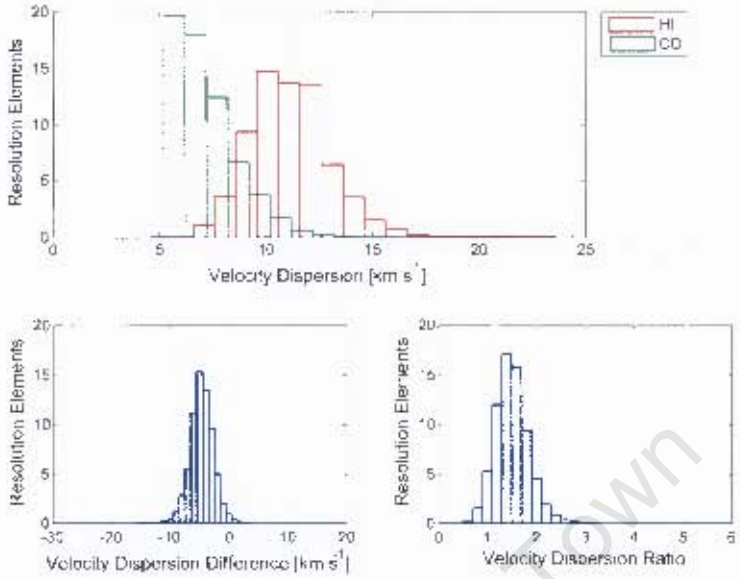

Figure A2: (Top) Distributions of the HI and CO dispersions for NGC 628. Lower Left and Right figures are histograms of the dispersion difference $\sigma_{CO} - \sigma_{HI}$ and dispersion ratio σ_{HI}/σ_{CO} in NGC 628.

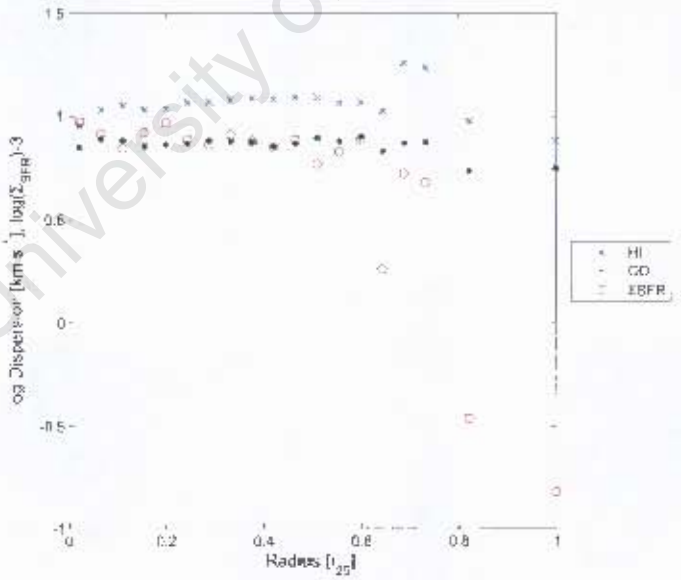

Figure A3: The radially smoothed log CO and log HI dispersions and the log star formation rate density in NGC 628 versus radius (in r_{25}). Smoothing was done in annuli of width 13". Log dispersions are plotted and log star formation rate density -3 is plotted (with Σ_{SFR} in the units : $[M_\odot\ Myr^{-1}\ kpc^{-1}]$).

NGC 925

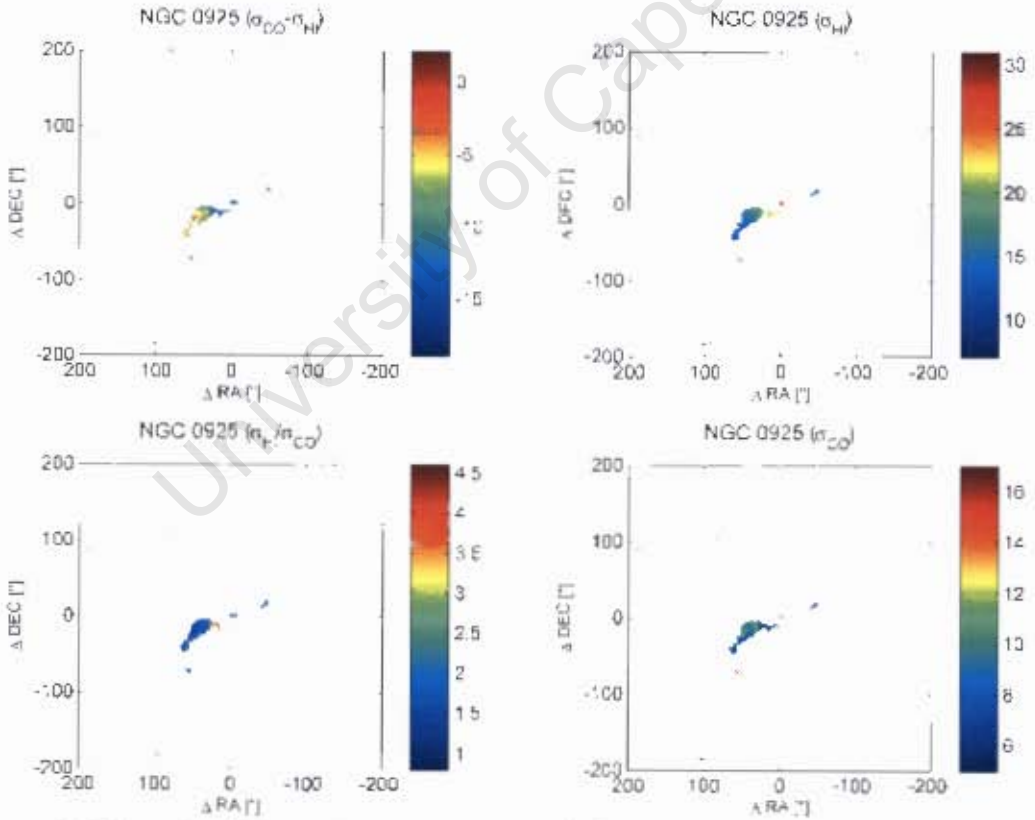

Figure A4: Dispersion difference ($\sigma_{CO} - \sigma_{HI}$) (top left), dispersion ratio (σ_{HI}/σ_{CO}) (bottom left), CO dispersion (bottom right) and HI dispersion (top right) maps of NGC 925. The colourmap values of the dispersion plots are in units of km s^{-1}.

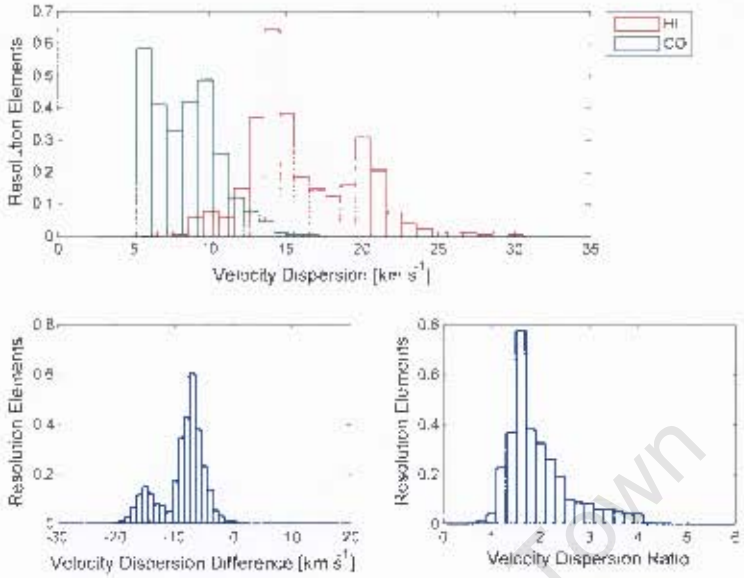

Figure A5: (Top) Distributions of the HI and CO dispersions for NGC 925. Lower Left and Right figures are plots of the dispersion difference $\sigma_{CO} - \sigma_{HI}$ and dispersion ratio σ_{HI}/σ_{CO} in NGC 925.

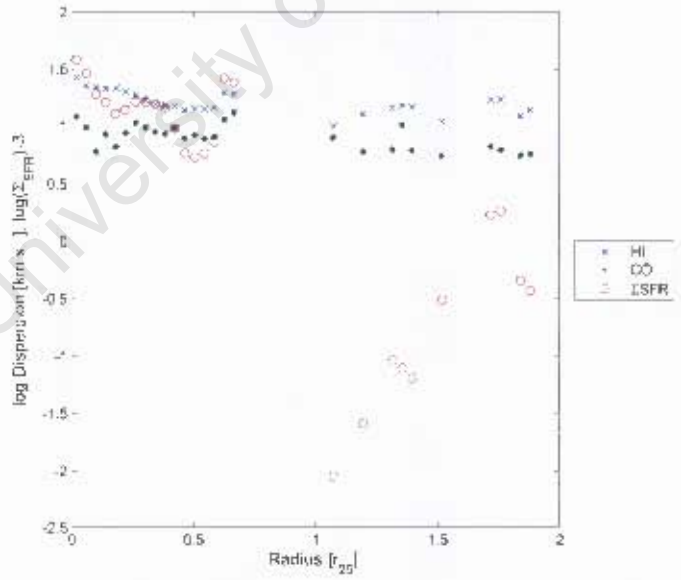

Figure A6: The radially smoothed log CO and log HI dispersions and the log star formation rate density in NGC 925 versus radius (in r_{25}). Smoothing was done in annuli of width 13". Log dispersions are plotted and log star formation rate density −3 is plotted (with Σ_{SFR} in the units : [$M_\odot$ Myr^{-1} kpc^{-1}]).

NGC 2403

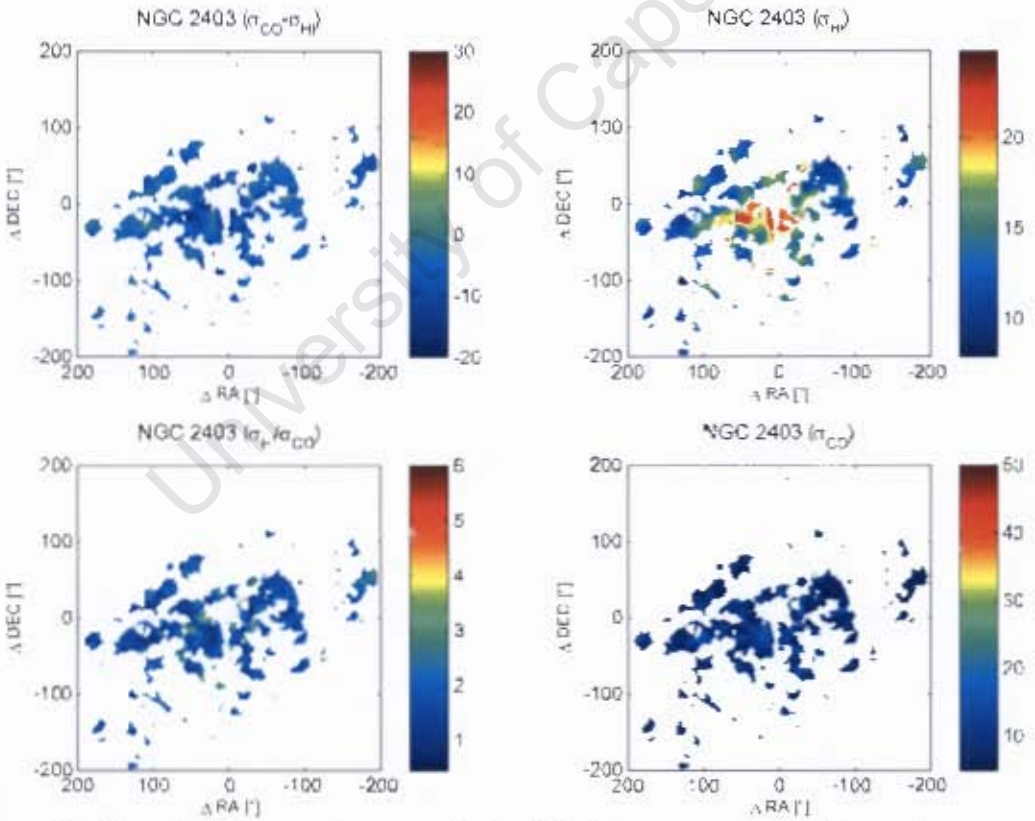

Figure A7: Dispersion difference ($\sigma_{CO} - \sigma_{HI}$) (top left), dispersion ratio (σ_{HI}/σ_{CO}) (bottom left), CO dispersion (bottom right) and HI dispersion (top right) maps of NGC 2403. The colourmap values of the dispersion plots are in units of km s^{-1}.

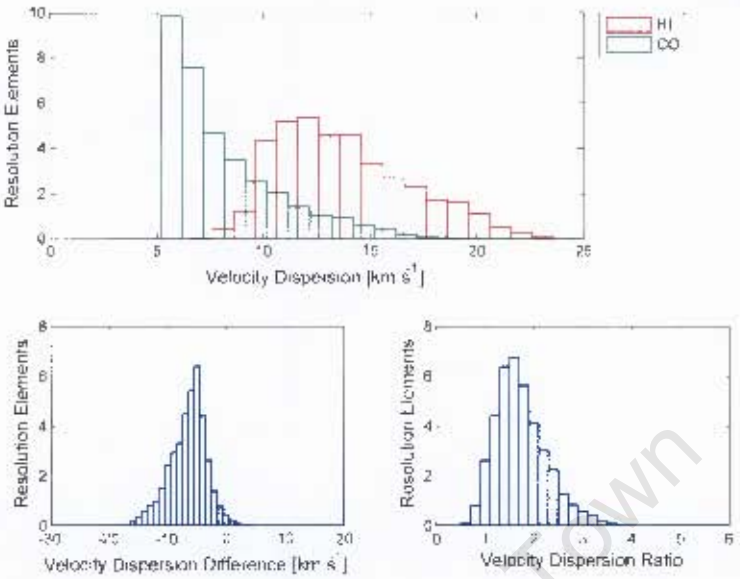

Figure A8: (Top) Distributions of the HI and CO dispersions for NGC 2403. Lower Left and Right figures are plots of the dispersion difference $\sigma_{CO} - \sigma_{HI}$ and dispersion ratio σ_{HI}/σ_{CO} in NGC 2403.

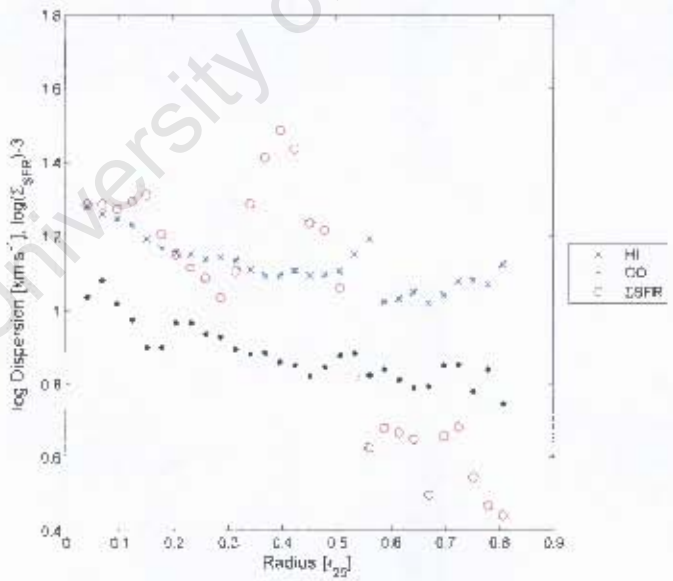

Figure A9: The radially smoothed log CO and log HI dispersions and the log star formation rate density in NGC 2403 versus radius (in r_{25}). Smoothing was done in annuli of width 13". Log dispersions are plotted and log star formation rate density −3 is plotted (with Σ_{SFR} in the units : [$M_\odot$ Myr^{-1} kpc^{-1}]).

NGC 2841

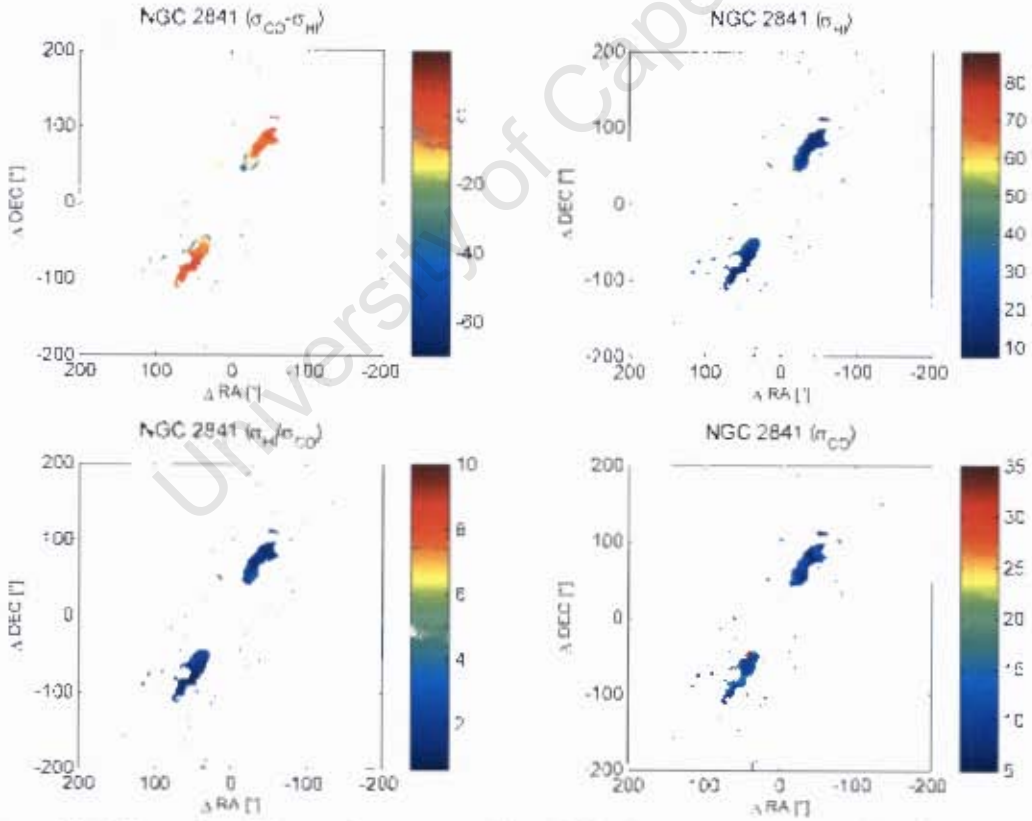

Figure A10: Dispersion difference ($\sigma_{CO} - \sigma_{HI}$) (top left), dispersion ratio (σ_{HI}/σ_{CO}) (bottom left), CO dispersion (bottom right) and HI dispersion (top right) maps of NGC 2841. The colourmap values of the dispersion plots are in units of km s^{-1}.

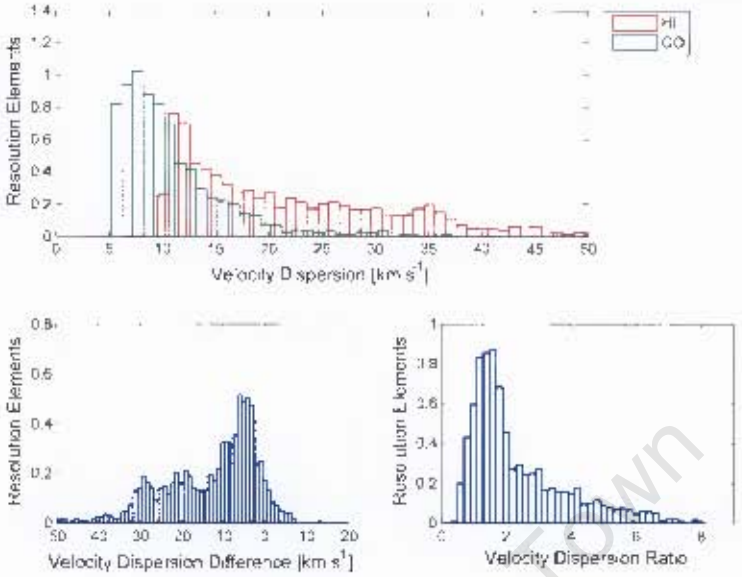

Figure A11: (Top) Distributions of the HI and CO dispersions for NGC 2841. Lower Left and Right figures are plots of the dispersion difference $\sigma_{CO} - \sigma_{HI}$ and dispersion ratio σ_{HI}/σ_{CO} in NGC 2841.

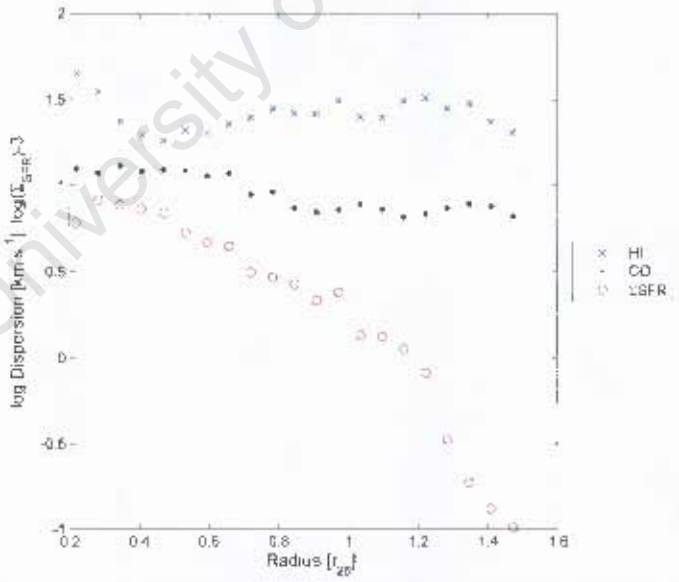

Figure A12: The radially smoothed log CO and log HI dispersions and the log star formation rate density in NGC 2841 versus radius (in r_{25}). Smoothing was done in annuli of width 13". Log dispersions are plotted and log star formation rate density −3 is plotted (with Σ_{SFR} in the units : [$M_\odot$ yr^{-1} kpc^{-1}]).

NGC 2903

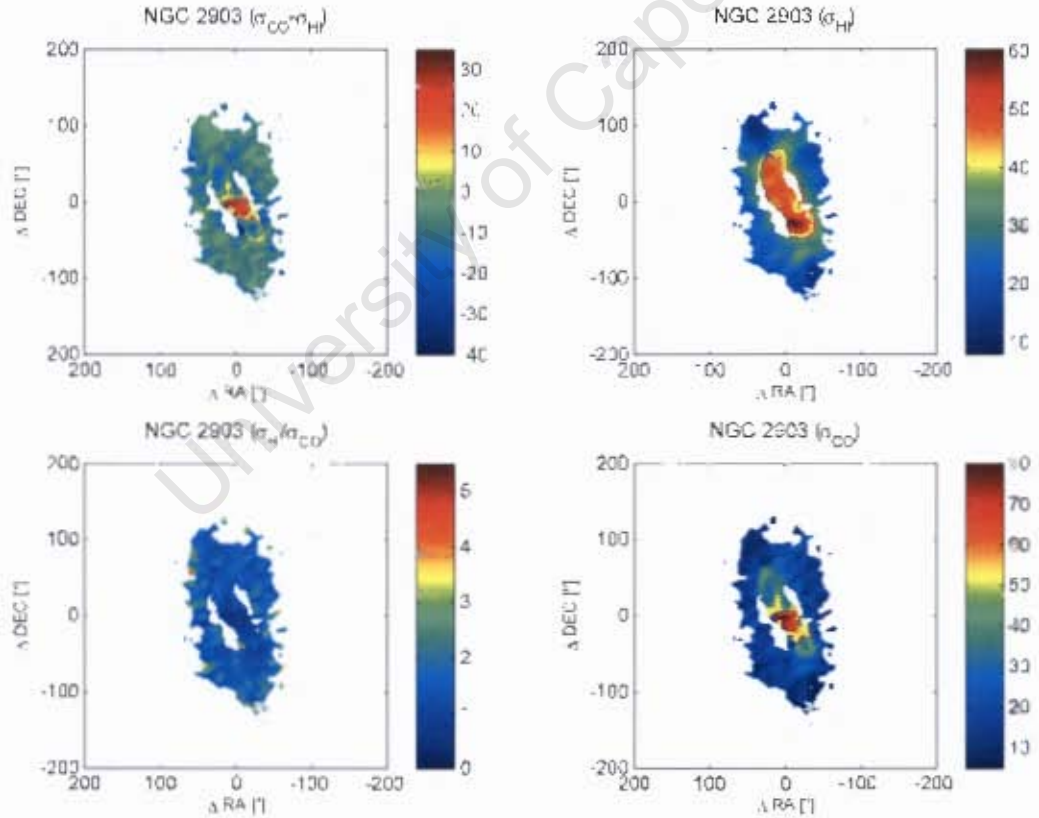

Figure A13: Dispersion difference ($\sigma_{CO} - \sigma_{HI}$) (top left), dispersion ratio (σ_{HI}/σ_{CO}) (bottom left), CO dispersion (bottom right) and HI dispersion (top right) maps of NGC 2903. The colourmap values of the dispersion plots are in units of kms $^{-1}$.

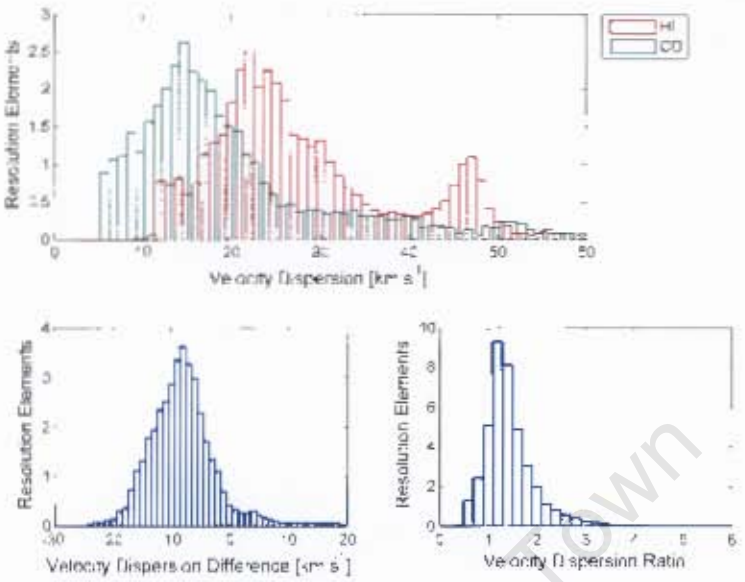

Figure A14: (Top) Distributions of the HI and CO dispersions for NGC 2903. Lower Left and Right figures are plots of the dispersion difference $\sigma_{CO} - \sigma_{HI}$ and dispersion ratio σ_{HI}/σ_{CO} in NGC 2903

NGC 2976

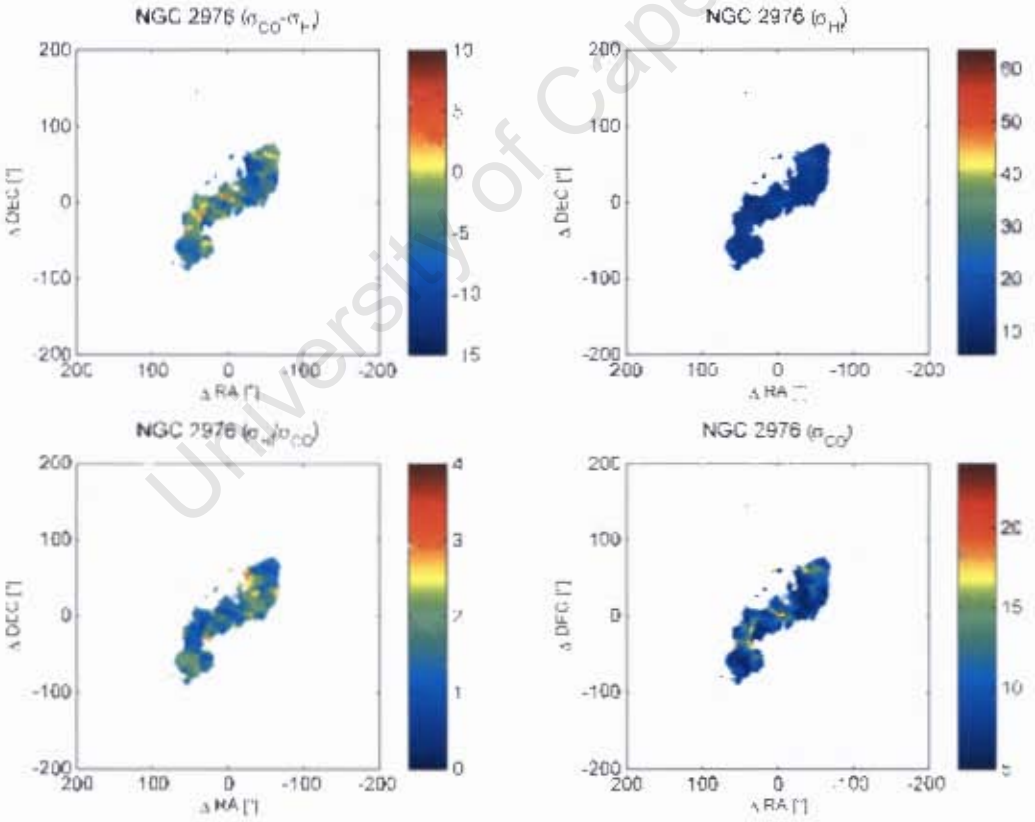

Figure A15: Dispersion difference ($\sigma_{CO} - \sigma_{HI}$) (top left), dispersion ratio (σ_{HI}/σ_{CO}) (bottom left), CO dispersion (bottom right) and HI dispersion (top right) maps of NGC 2976. The colourmap values of the dispersion plots are in units of km s^{-1}.

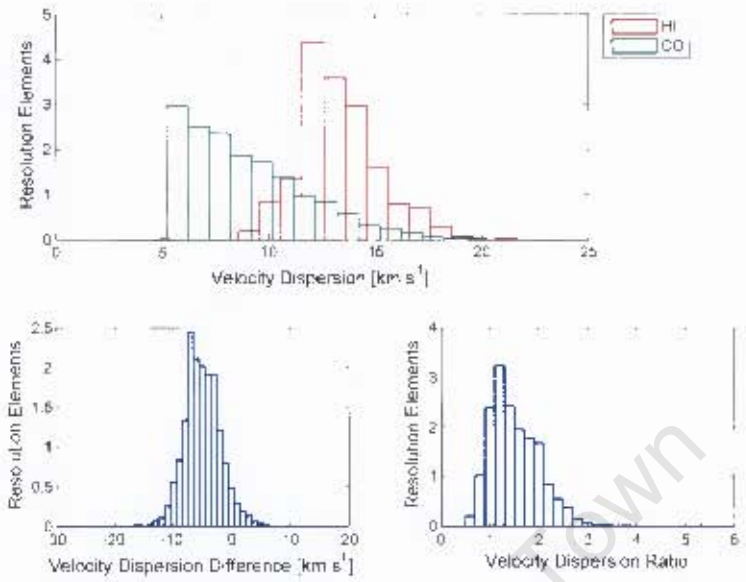

Figure A16: (Top) Distributions of the HI and CO dispersions for NGC 2976. Lower Left and Right figures are plots of the dispersion difference $\sigma_{CO} - \sigma_{HI}$ and dispersion ratio σ_{HI}/σ_{CO} in NGC 2976

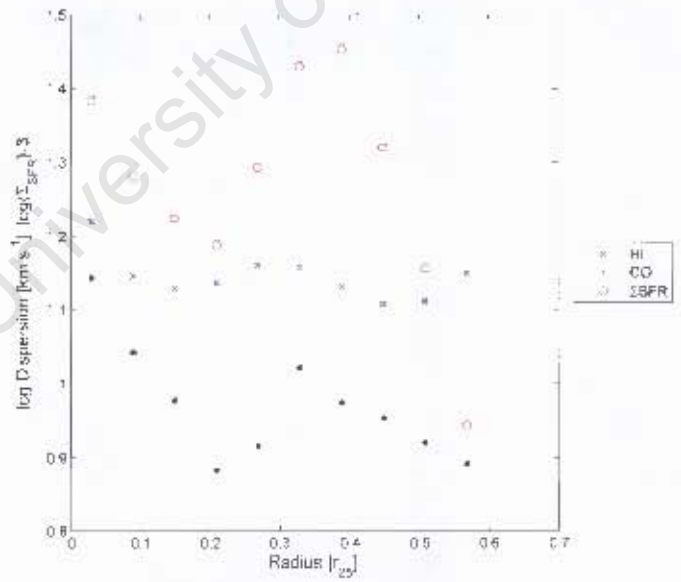

Figure A17: The radially smoothed log CO and log HI dispersions and the log star formation rate density in NGC 2976 versus radius (in r_{25}). Smoothing was done in annuli of width 13". Log dispersions are plotted and log star formation rate density -3 is plotted (with Σ_{SFR} in the units : [$M_\odot$ Myr^{-1} kpc^{-1}]).

NGC 3077

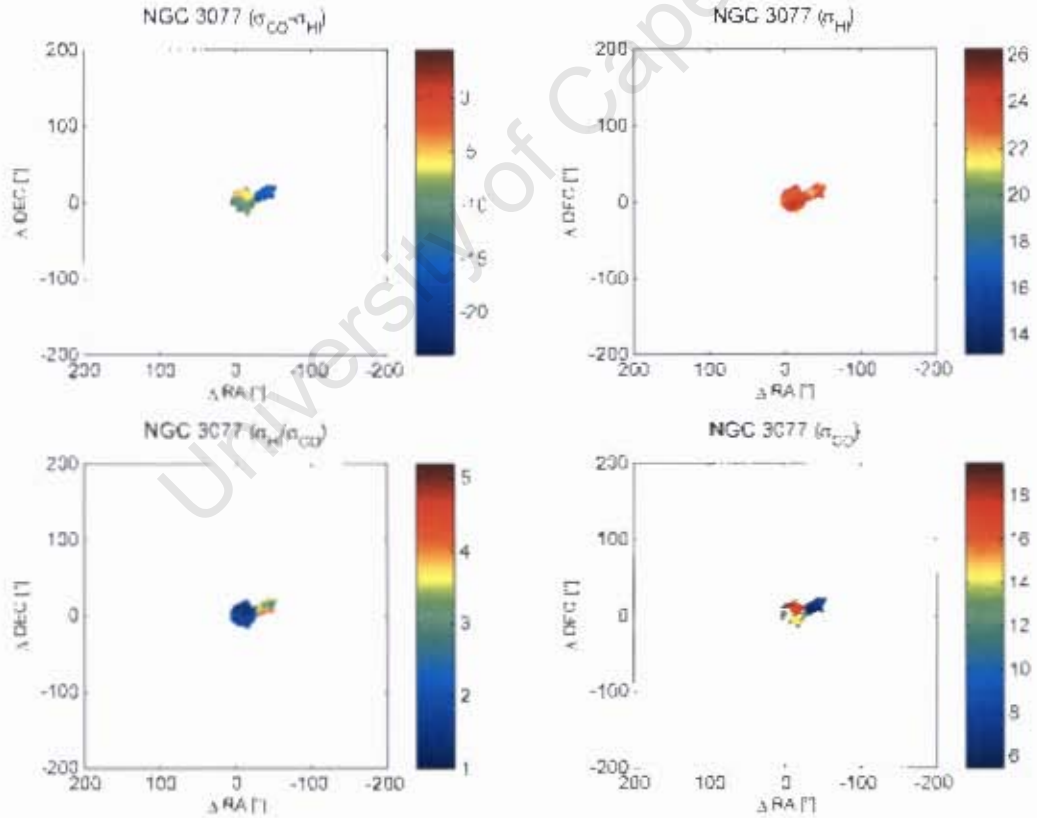

Figure A18: Dispersion difference ($\sigma_{CO} - \sigma_{HI}$) (top left), dispersion ratio (σ_{HI}/σ_{CO}) (bottom left), CO dispersion (bottom right) and HI dispersion (top right) maps of NGC 3077. The colourmap values of the dispersion plots are in units of km s $^{-1}$.

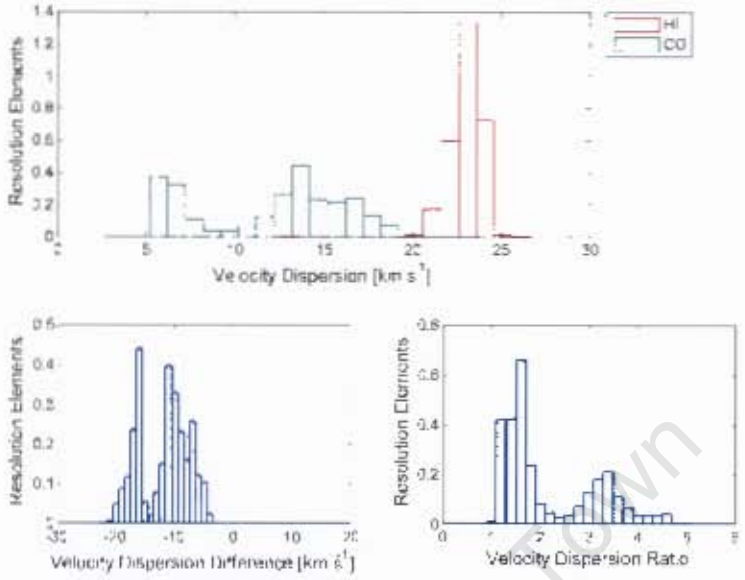

Figure A19: (Top) Distributions of the HI and CO dispersions for NGC 3077. Lower Left and Right figures are plots of the dispersion difference $\sigma_{CO} - \sigma_{HI}$ and dispersion ratio σ_{HI}/σ_{CO} in NGC 3077

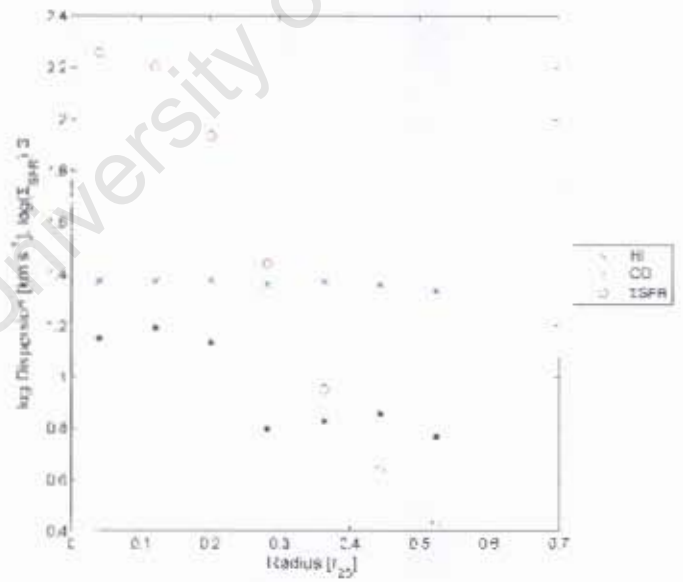

Figure A20: The radially smoothed log CO and log HI dispersions and the log star formation rate density in NGC 3077 versus the radius (in r_{25}). Smoothing was done in annuli of width 13". Log dispersions are plotted and log star formation rate density + 3 is plotted (with Σ_{SFR} in the units : $[M_\odot\ Myr^{-1}\ kpc^{-1}]$).

NGC 3184

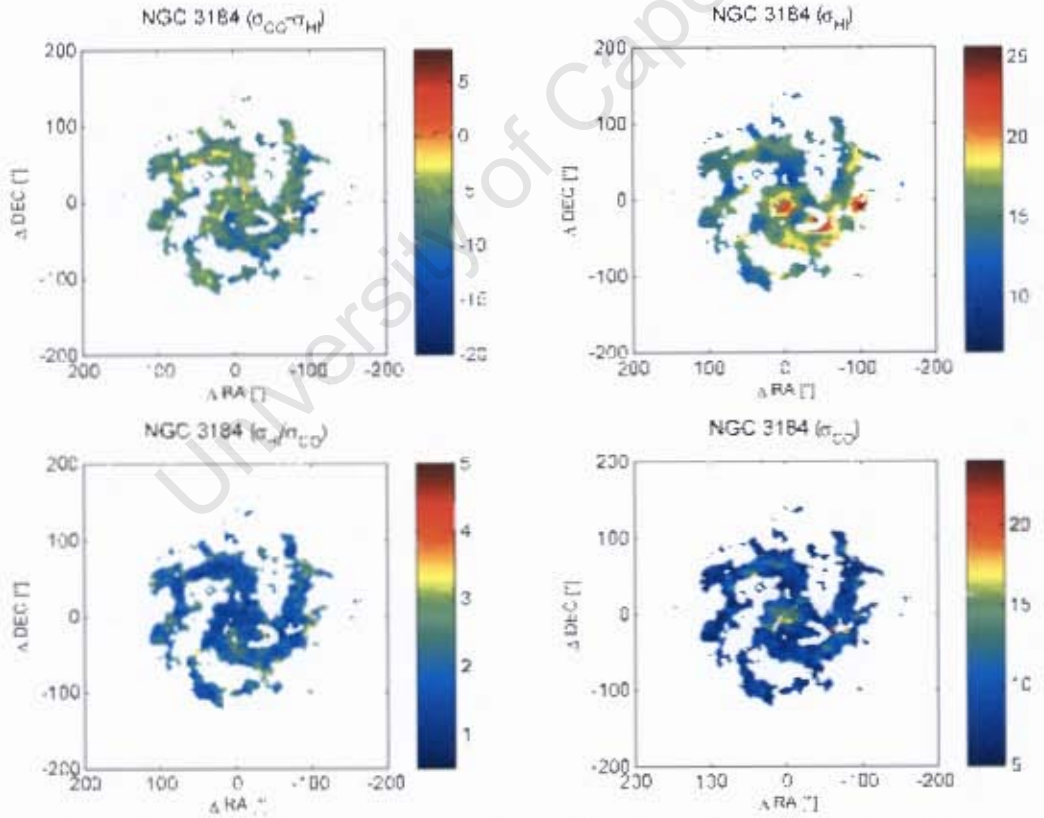

Figure A21: Dispersion difference ($\sigma_{CO}-\sigma_{HI}$) (top left), dispersion ratio (σ_{HI}/σ_{CO}) (bottom left), CO dispersion (bottom right) and HI dispersion (top right) maps of NGC 3184. The colourmap values of the dispersion plots are in units of $\mathrm{km\,s^{-1}}$.

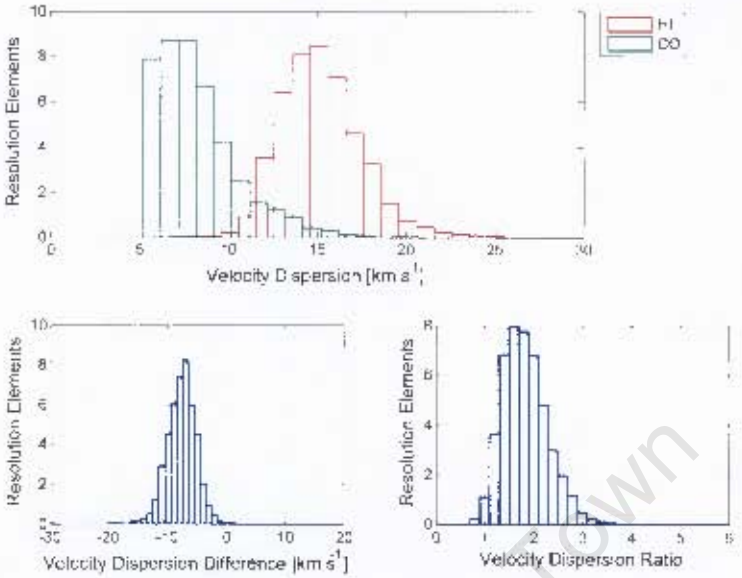

Figure A22: (Top) Distributions of the HI and CO dispersions for NGC 3184. Lower Left and Right figures are plots of the dispersion difference $\sigma_{CO} - \sigma_{HI}$ and dispersion ratio σ_{HI}/σ_{CO} in NGC 3184

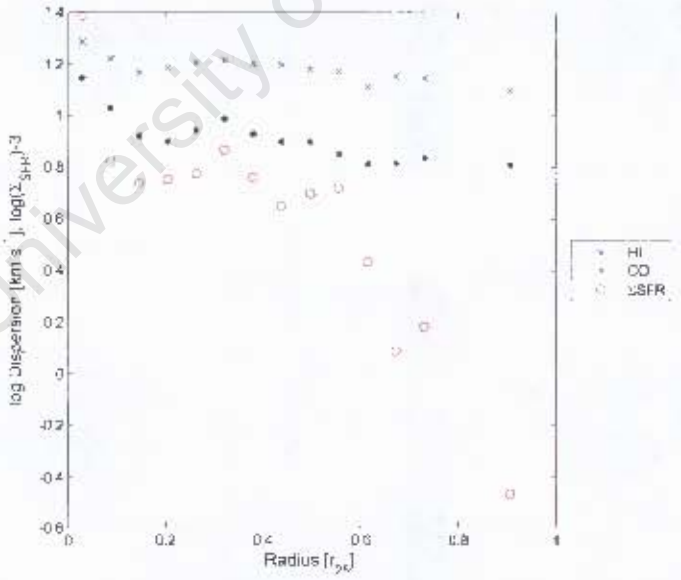

Figure A23: The radially smoothed log CO and log HI dispersions and the log star formation rate density in NGC 3184 versus the radius (in r_{25}). Smoothing was done in annuli of width 13". Log dispersions are plotted and log star formation rate density −3 is plotted (with Σ_{SFR} in the units : $[M_\odot\ Myr^{-1}\ kpc^{-1}]$).

NGC 3198

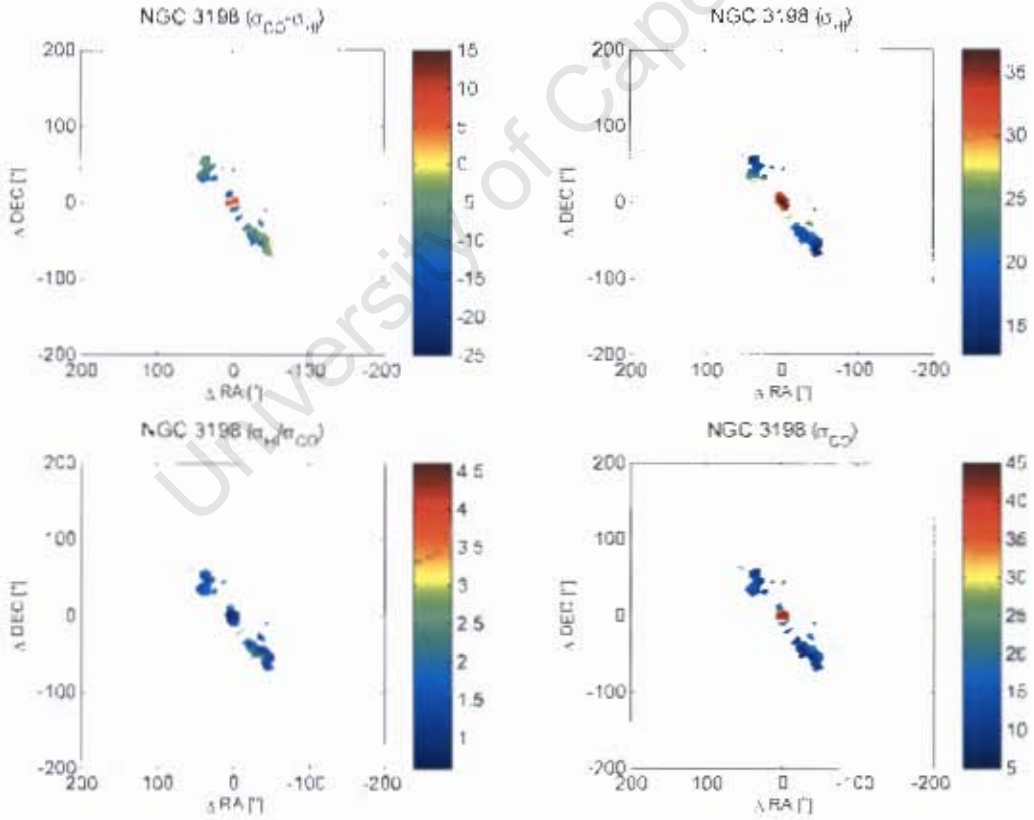

Figure A24: Dispersion difference ($\sigma_{CO} - \sigma_{HI}$) (top left), dispersion ratio (σ_{HI}/σ_{CO}) (bottom left), CO dispersion (bottom right) and HI dispersion (top right) maps of NGC 3198. The colourmap values of the dispersion plots are in units of km s^{-1}.

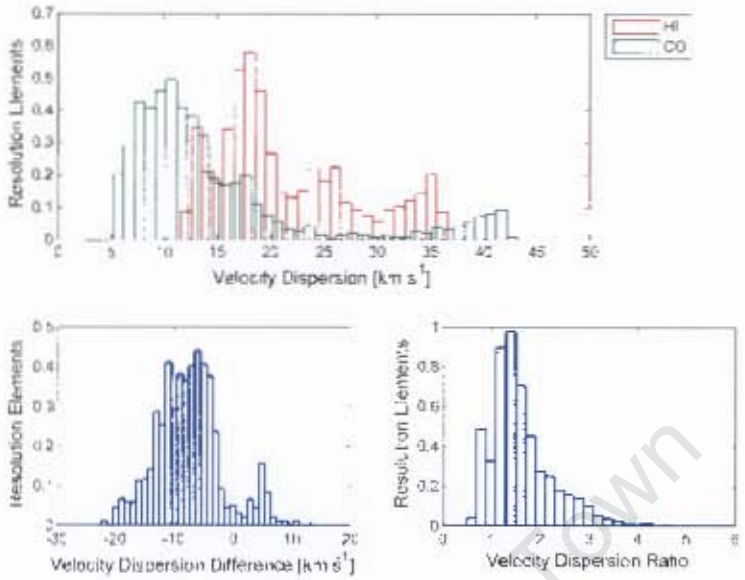

Figure A25: (Top) Distributions of the HI and CO dispersions for NGC 3198. Lower Left and Right figures are plots of the dispersion difference $\sigma_{CO} - \sigma_{HI}$ and dispersion ratio σ_{HI}/σ_{CO} in NGC 3198

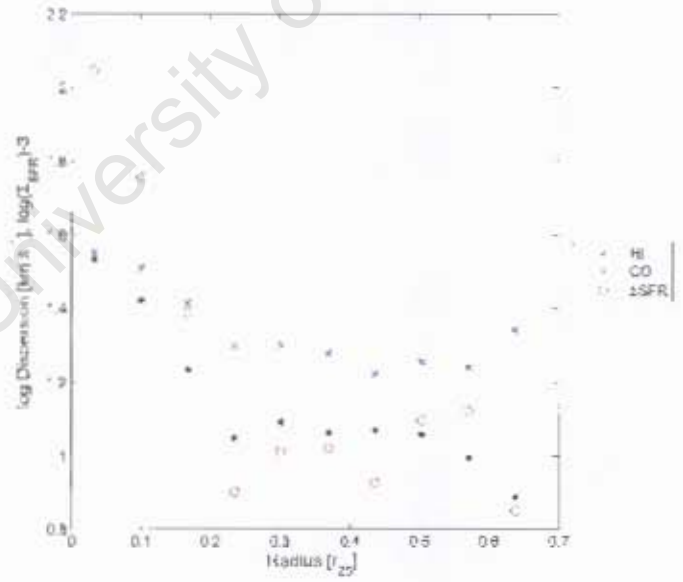

Figure A26: The radially smoothed log CO and log HI dispersions and the log star formation rate density in NGC 3198 versus the radius (in r_{25}). Smoothing was done in annuli of width 13". Log dispersions are plotted and log star formation rate density − 3 is plotted (with Σ_{SFR} in the units : $[M_\odot\ Myr^{-1}\ kpc^{-1}]$).

NGC 3351

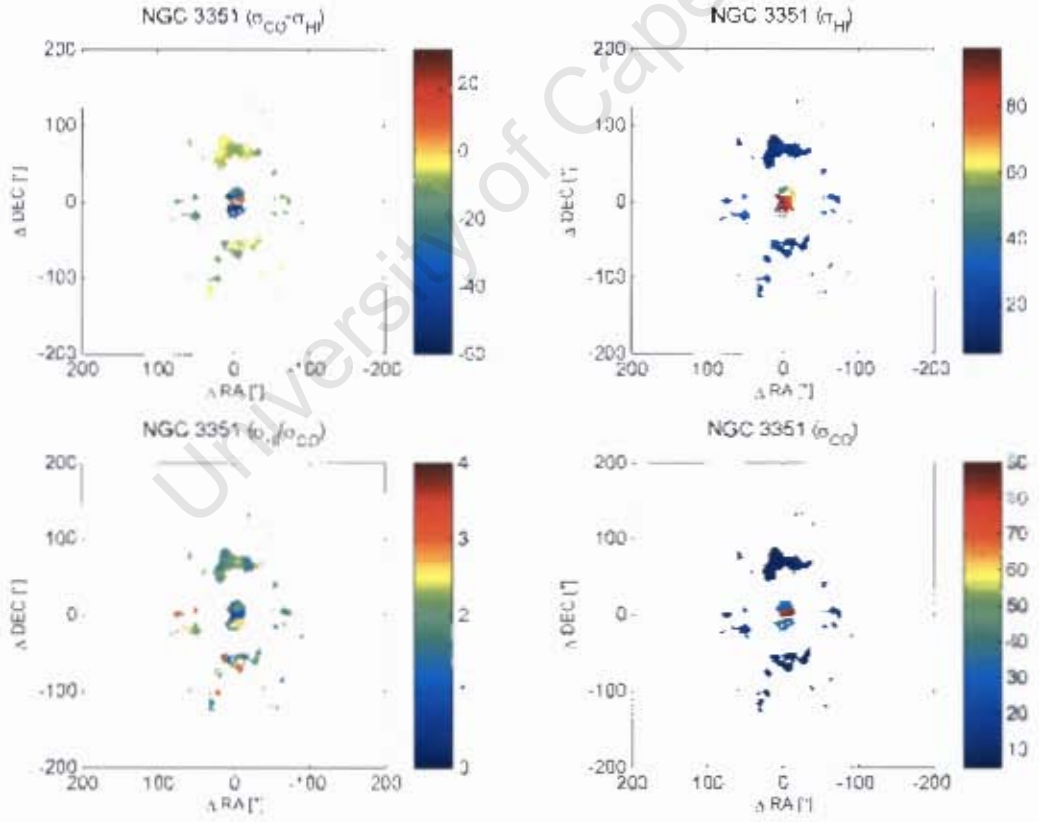

Figure A27: Dispersion difference ($\sigma_{CO} - \sigma_{HI}$) (top left), dispersion ratio (σ_{HI}/σ_{CO}) (bottom left), CO dispersion (bottom right) and HI dispersion (top right) maps of NGC 3351. The colourmap values of the dispersion plots are in units of $\mathrm{km\,s^{-1}}$.

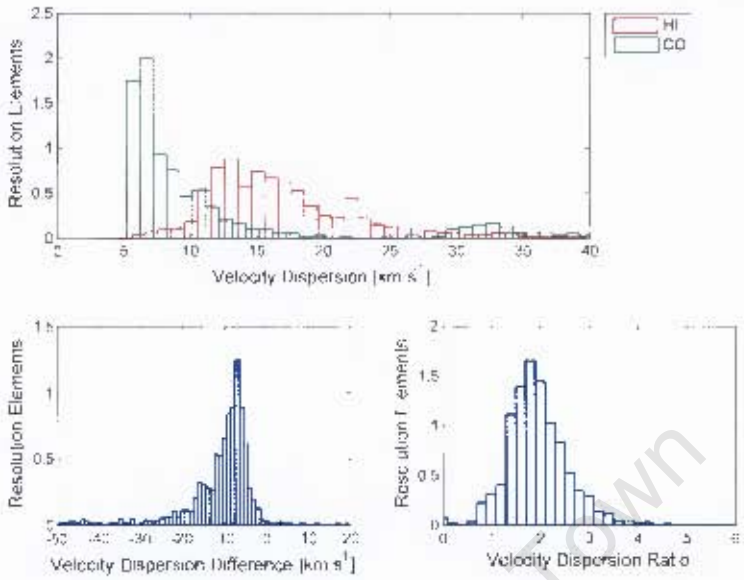

Figure A28: (Top)Distributions of the HI and CO dispersions for NGC 3351. Lower Left and Right figures are plots of the dispersion difference $\sigma_{CO} - \sigma_{HI}$ and dispersion ratio σ_{HI}/σ_{CO} in NGC 3351

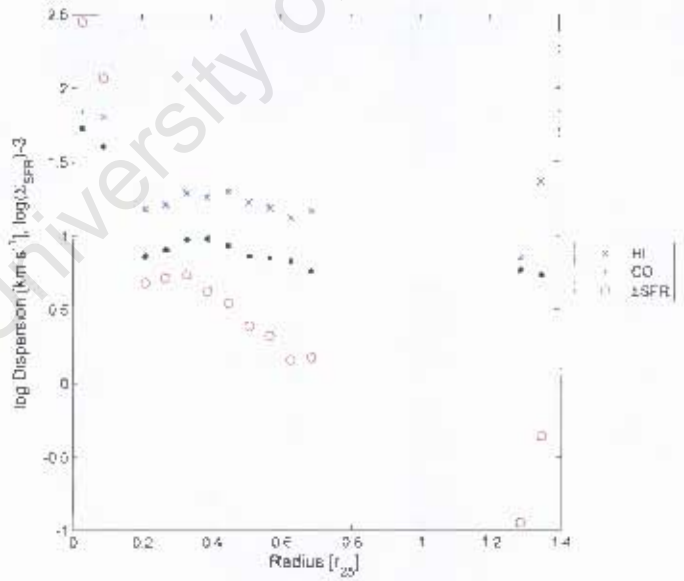

Figure A29: The radially smoothed log CO and log HI dispersions and the log star formation rate density in NGC 3351 versus the radius (in r_{25}). Smoothing was done in annuli of width 13". Log dispersions are plotted and log star formation rate density -3 is plotted (with Σ_{SFR} in the units : $[M_\odot\ Myr^{-1}\ kpc^{-1}]$).

NGC 4214

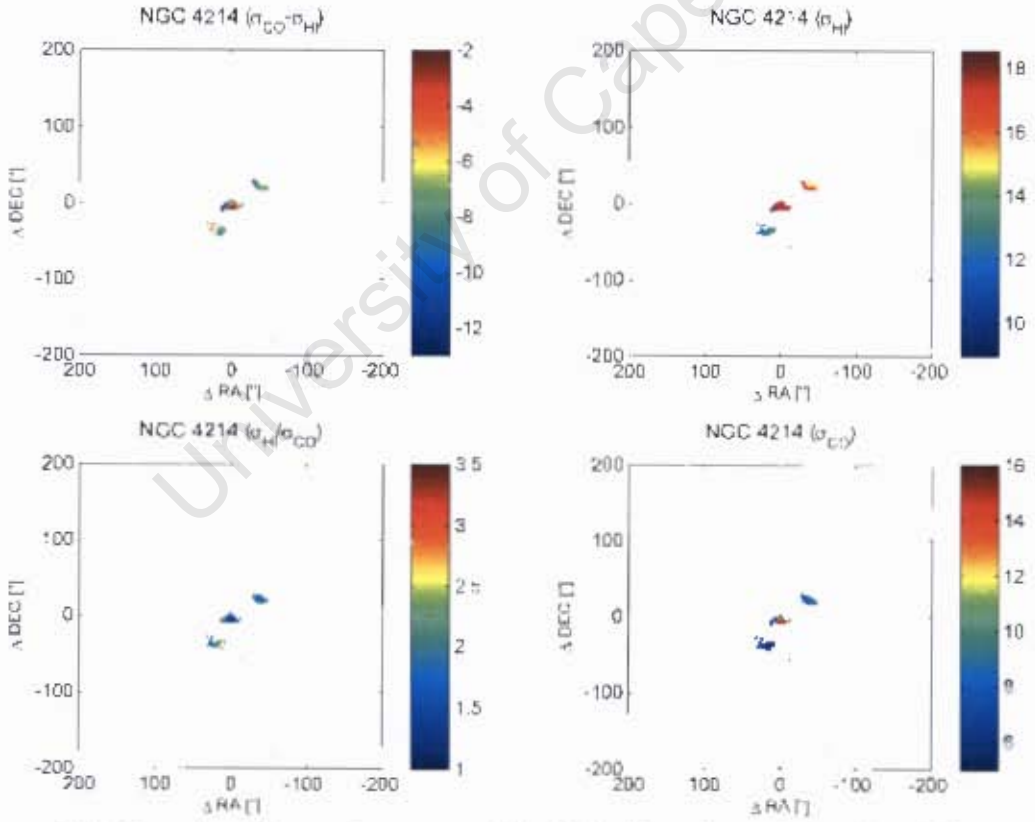

Figure A30: Dispersion difference ($\sigma_{CO} - \sigma_{HI}$) (top left), dispersion ratio (σ_{HI}/σ_{CO}) (bottom left), CO dispersion (bottom right) and HI dispersion (top right) maps of NGC 4214. The colourmap values of the dispersion plots are in units of km s $^{-1}$.

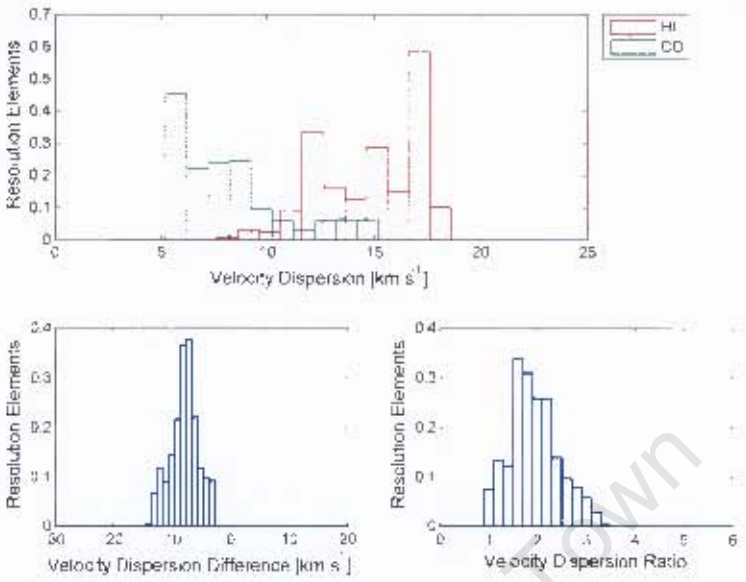

Figure A31: (Top) Distributions of the HI and CO dispersions for NGC 4214. Lower Left and Right figures are plots of the dispersion difference $\sigma_{CO} - \sigma_{HI}$ and dispersion ratio σ_{HI}/σ_{CO} in NGC 4214

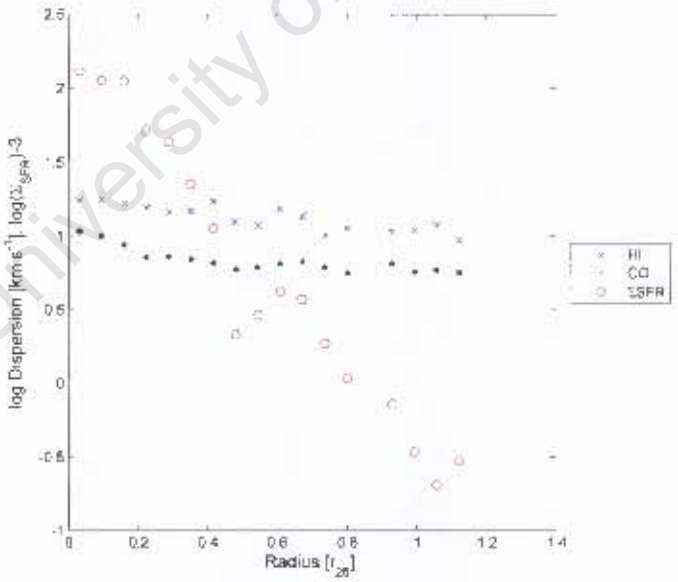

Figure A32: The radially smoothed log CO and log HI dispersions and the log star formation rate density in NGC 4214 versus the radius (in r_{25}). Smoothing was done in annuli of width 13". Log dispersions are plotted and log star formation rate density − 3 is plotted (with Σ_{SFR} in the units : [$M_\odot$ Myr^{-1} kpc^{-1}]).

NGC 4736

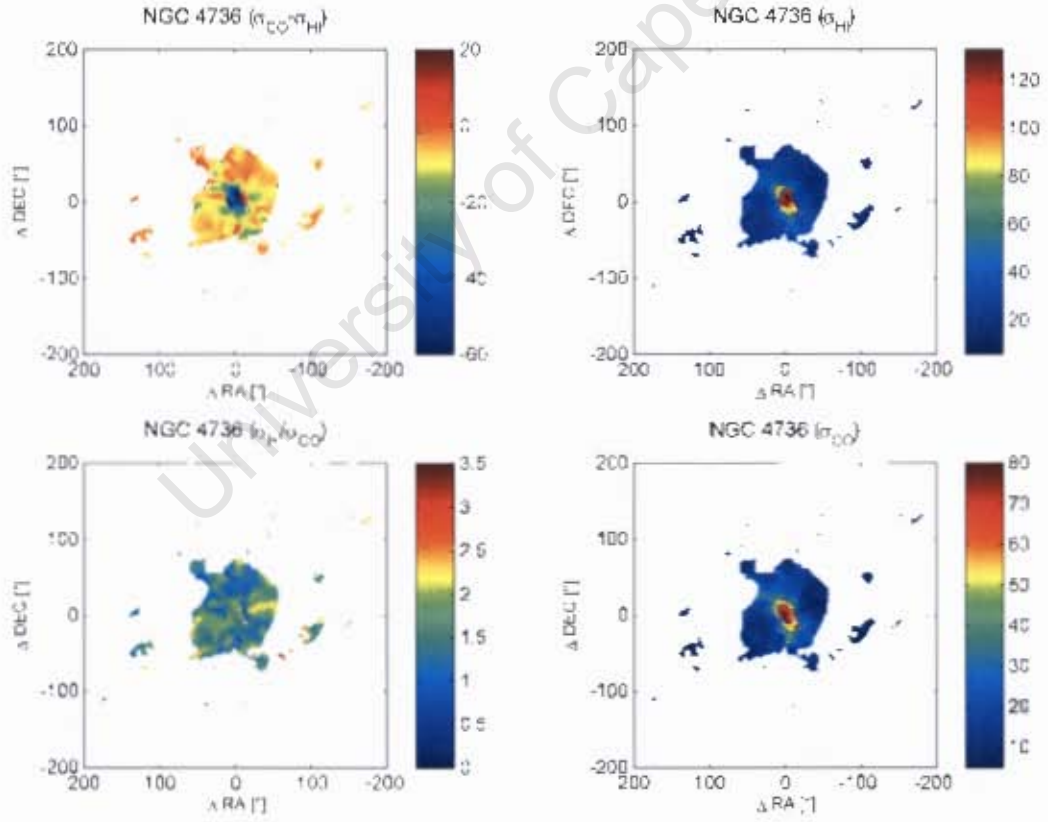

Figure A33: Dispersion difference ($\sigma_{CO} - \sigma_{HI}$) (top left), dispersion ratio (σ_{HI}/σ_{CO}) (bottom left), CO dispersion (bottom right) and HI dispersion (top right) maps of NGC 4736. The colourmap values of the dispersion plots are in units of kms^{-1}.

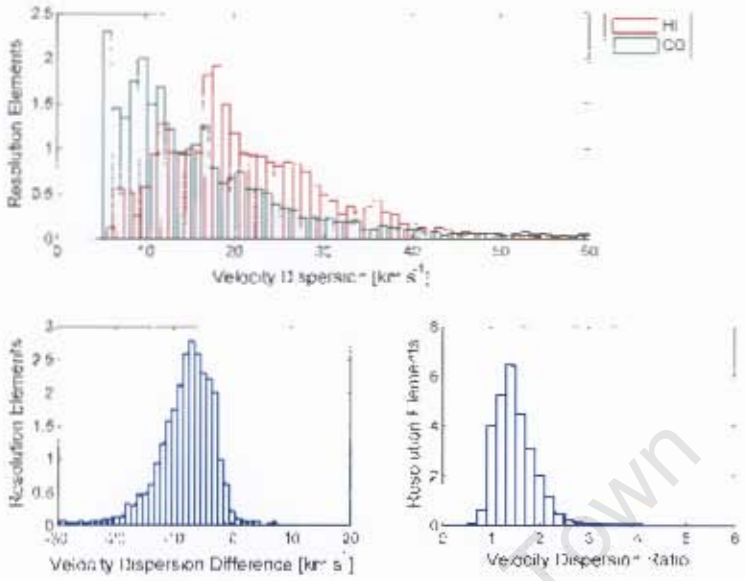

Figure A34: (Top) Distributions of the HI and CO dispersions for NGC 4736. Lower Left and Right figures are plots of the dispersion difference $\sigma_{CO} - \sigma_{HI}$ and dispersion ratio σ_{HI}/σ_{CO} in NGC 4736

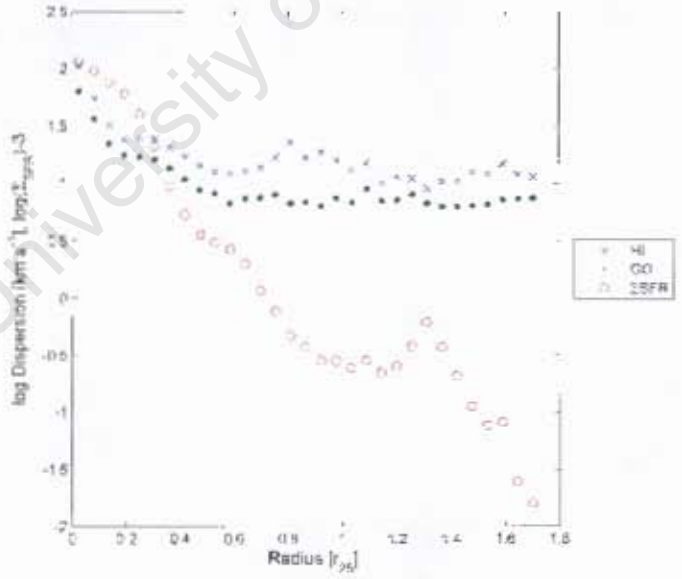

Figure A35: The radially smoothed log CO and log HI dispersions and the log star formation rate density in NGC 4736 versus the radius (in r_{25}). Smoothing was done in annuli of width 13". Log dispersions are plotted and log star formation rate density −3 is plotted (with Σ_{SFR} in the units : [$M_\odot$ Myr^{-1} kpc^{-1}]).

NGC 5055

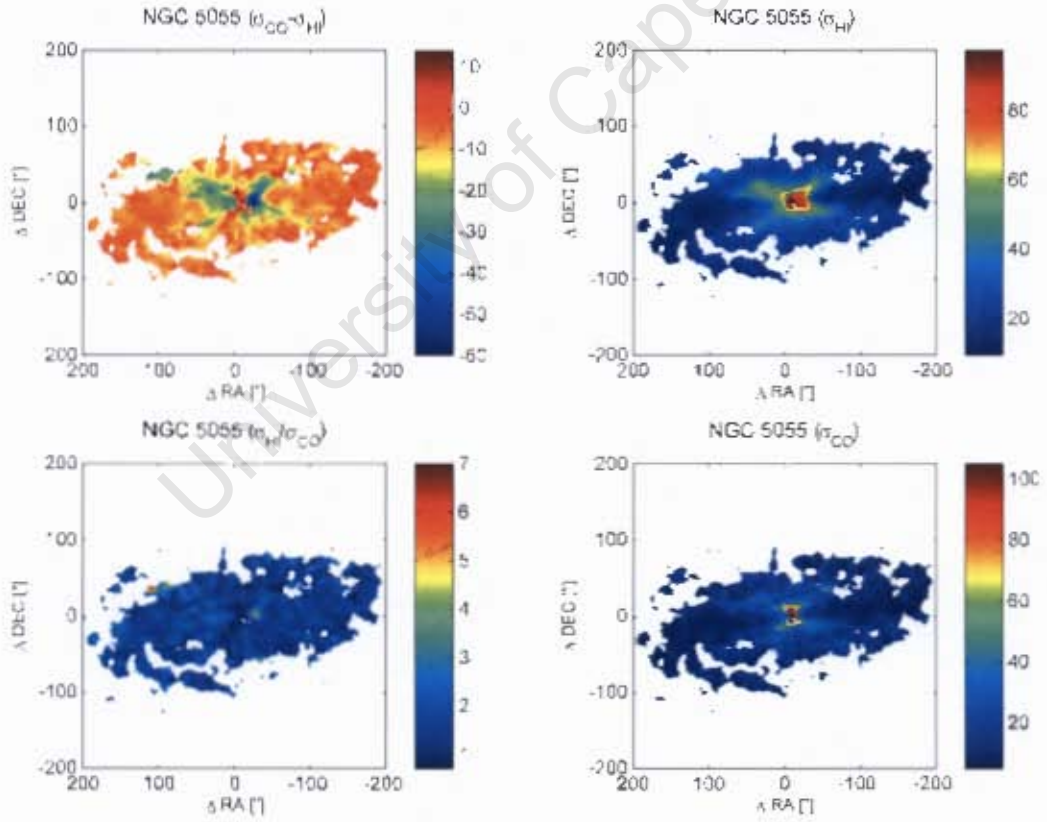

Figure A36: Dispersion difference ($\sigma_{CO} - \sigma_{HI}$) (top left), dispersion ratio (σ_{HI}/σ_{CO}) (bottom left), CO dispersion (bottom right) and HI dispersion (top right) maps of NGC 5055. The colourmap values of the dispersion plots are in units of km s^{-1}.

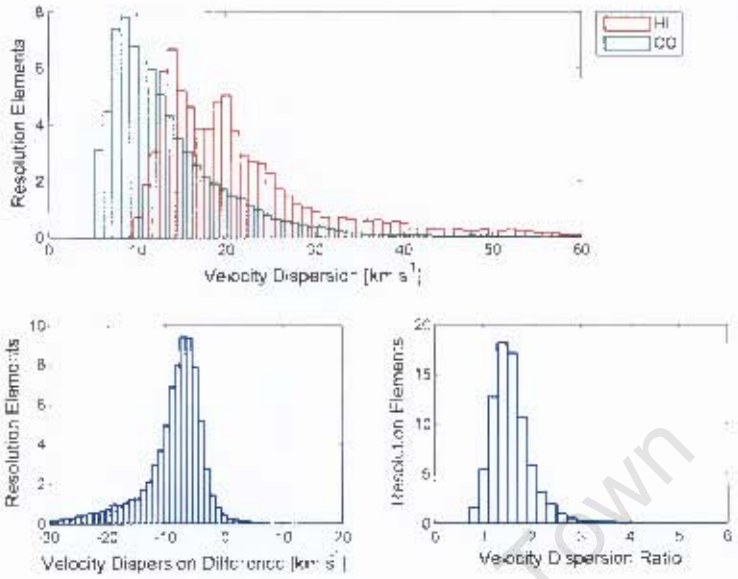

Figure A37: (Top) Distributions of the HI and CO dispersions for NGC 5055. Lower Left and Right figures are plots of the dispersion difference $\sigma_{CO} - \sigma_{HI}$ and dispersion ratio σ_{HI}/σ_{CO} in NGC 5055

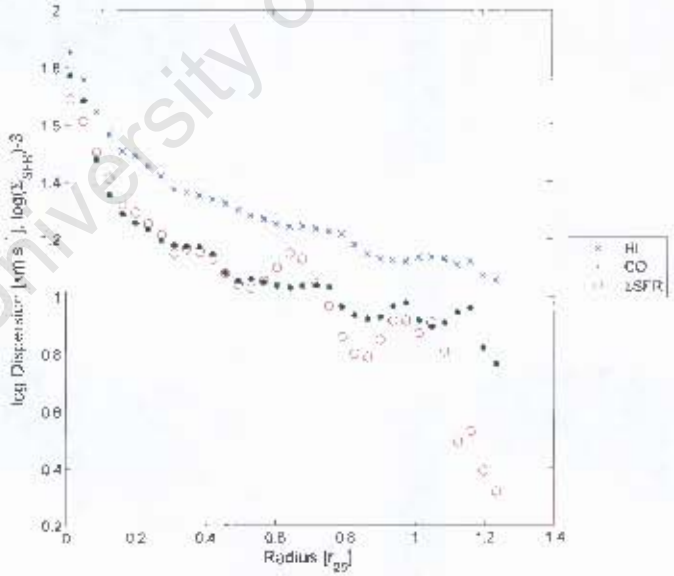

Figure A38: The radially smoothed log CO and log HI dispersions and the log star formation rate density in NGC 5055 versus the radius (in r_{25}). Smoothing was done in annuli of width 13". Log dispersions are plotted and log star formation rate density −3 is plotted (with Σ_{SFR} in the units : $[M_\odot\ Myr^{-1}\ kpc^{-2}]$).

NGC 5194

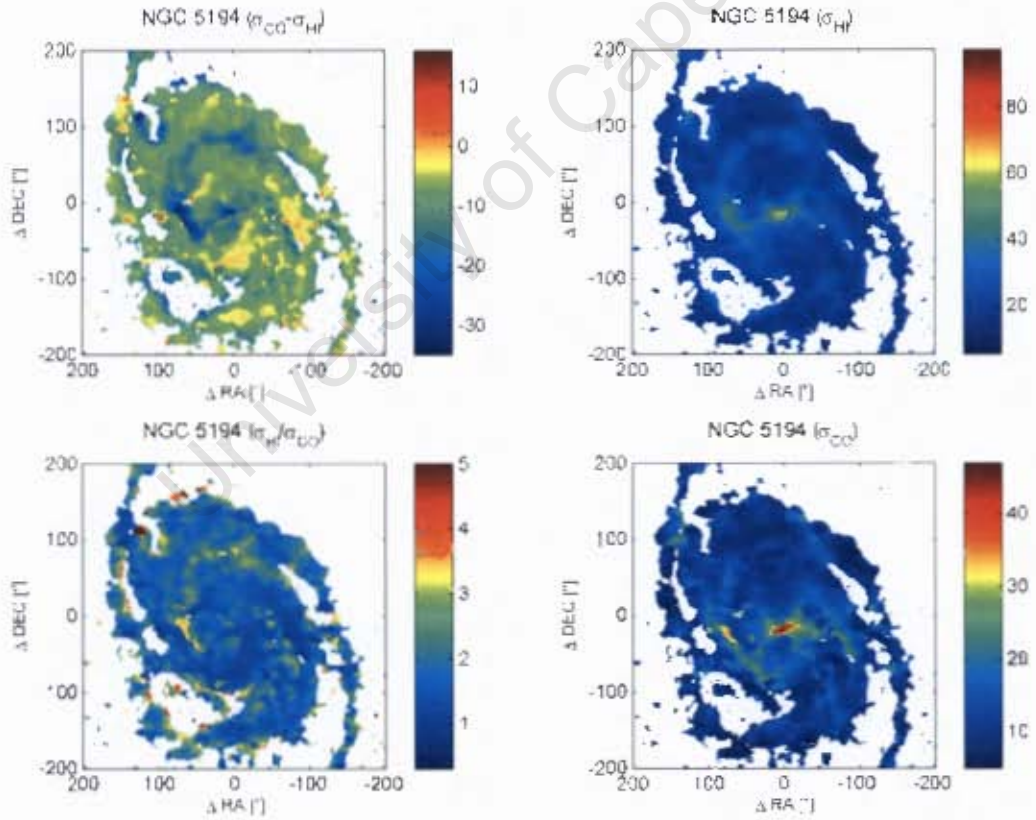

Figure A39: Dispersion difference ($\sigma_{CO} - \sigma_{HI}$) (top left), dispersion ratio (σ_{HI}/σ_{CO}) (bottom left), CO dispersion (bottom right) and HI dispersion (top right) maps of NGC 5194. The colourmap values of the dispersion plots are in units of kms $^{-1}$.

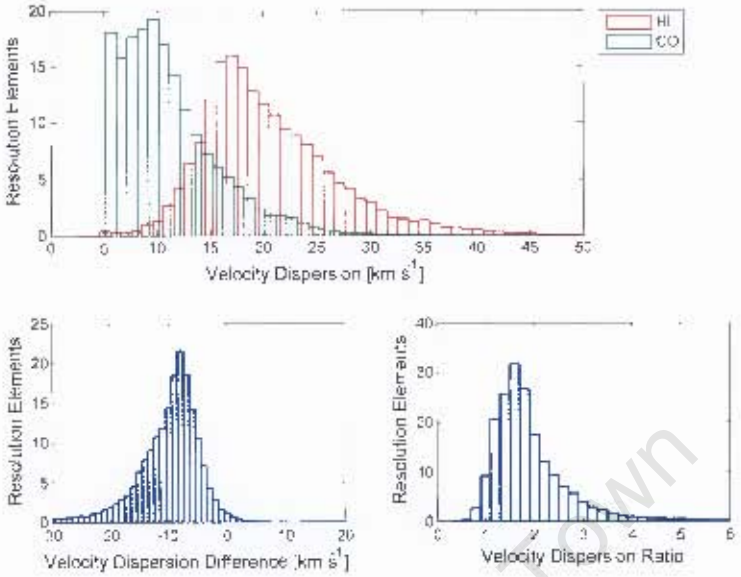

Figure A40: (Top) Distributions of the HI and CO dispersions for NGC 5194. Lower Left and Right figures are plots of the dispersion difference $\sigma_{CO} - \sigma_{HI}$ and dispersion ratio σ_{HI}/σ_{CO} in NGC 5194

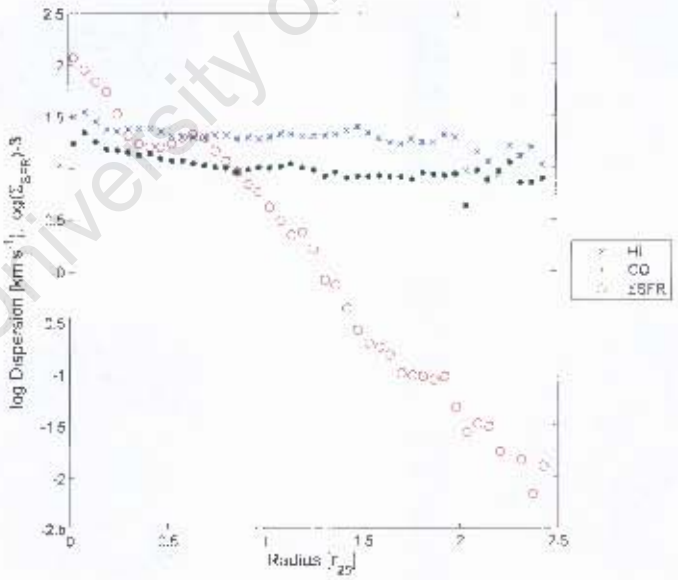

Figure A41: The radially smoothed log CO and log HI dispersions and the log star formation rate density in NGC 5194 versus the radius (in r_{25}). Smoothing was done in annuli of width 13". Log dispersions are plotted and log star formation rate density -3 is plotted (with Σ_{SFR} in the units : [$M_\odot$ Myr^{-1} kpc^{-1}]).

NGC 6946

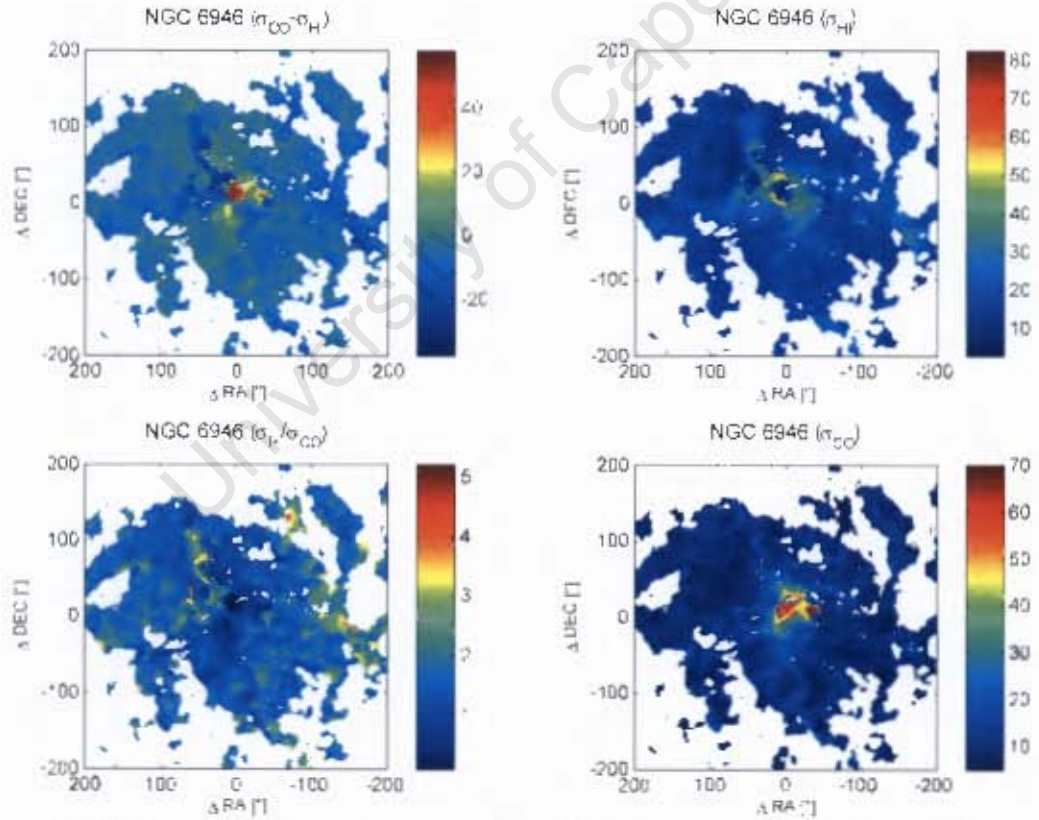

Figure A42: Dispersion difference ($\sigma_{CO} - \sigma_{HI}$) (top left), dispersion ratio (σ_{HI}/σ_{CO}) (bottom left), CO dispersion (bottom right) and HI dispersion (top right) maps of NGC 6946. The colourmap values of the dispersion plots are in units of km s^{-1}.

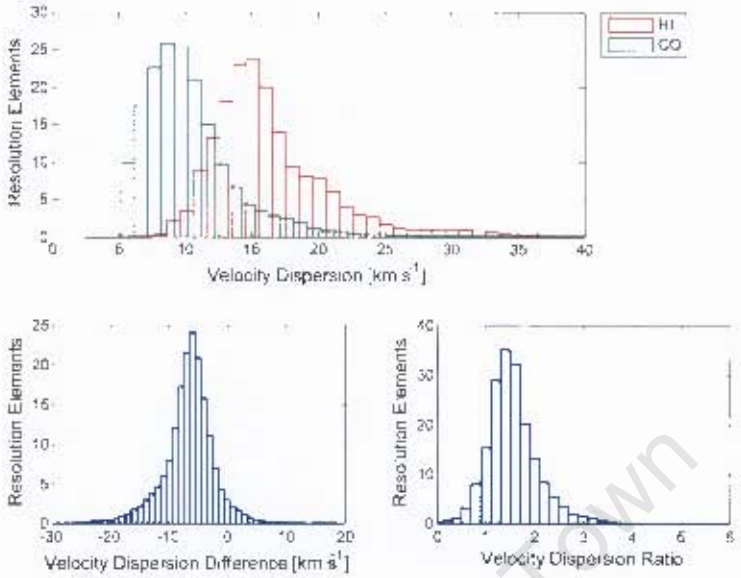

Figure A43: (Top) Distributions of the HI and CO dispersions for NGC 6946. Lower Left and Right figures are plots of the dispersion difference $\sigma_{CO} - \sigma_{HI}$ and dispersion ratio σ_{HI}/σ_{CO} in NGC 6946

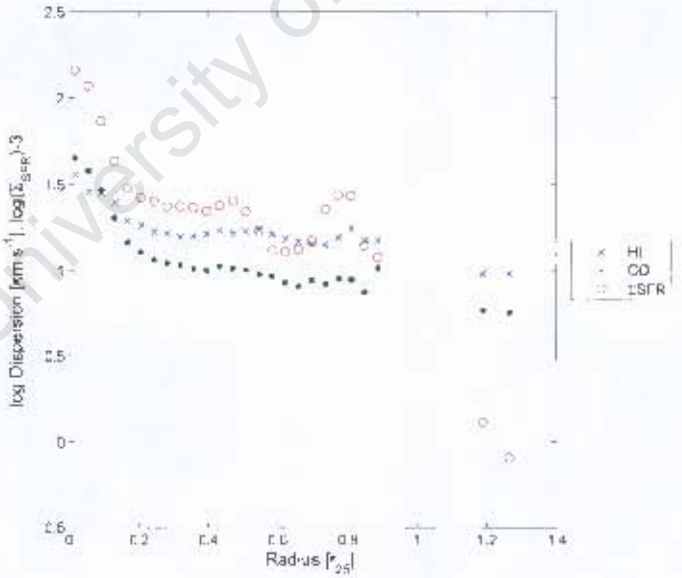

Figure A44: The radially smoothed log CO and log HI dispersions and the log star formation rate density in NGC 6946 versus the radius (in r_{25}). Smoothing was done in annuli of width 13". Log dispersions are plotted and log star formation rate density -3 is plotted (with Σ_{SFR} in the units : [$M_\odot$ Myr^{-1} kpc^{-1}]).

NGC 7331

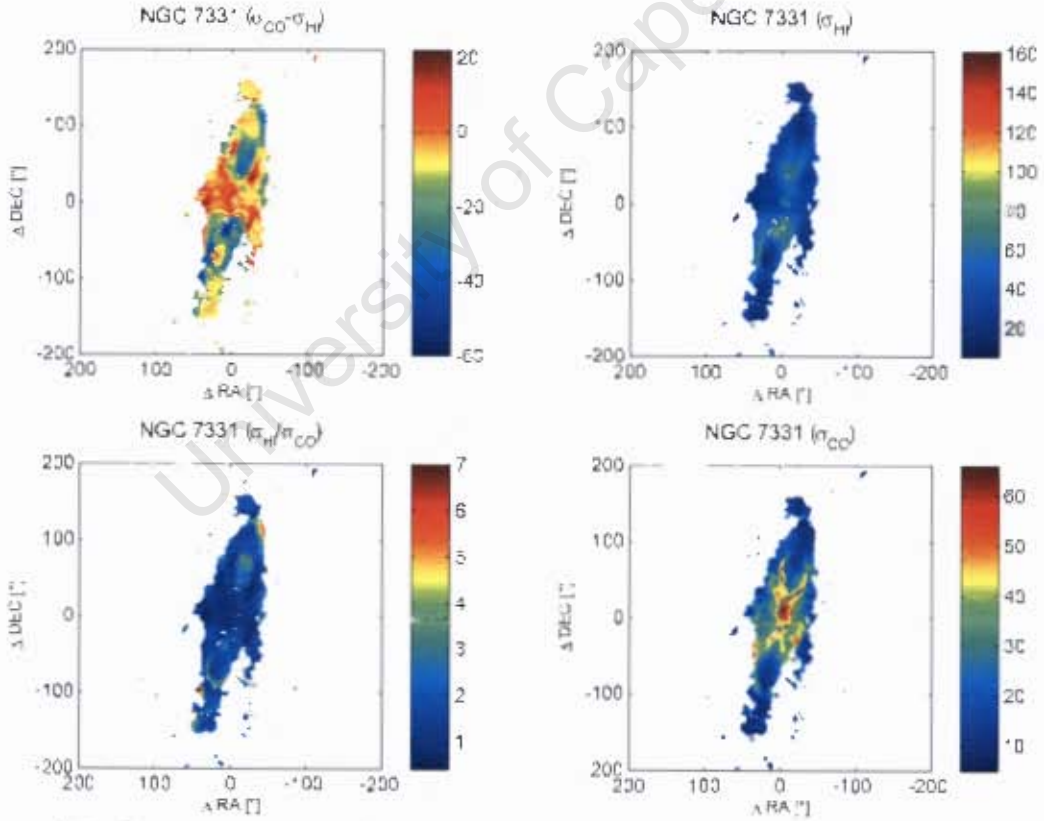

Figure A45: Dispersion difference ($\sigma_{CO} - \sigma_{HI}$) (top left), dispersion ratio (σ_{HI}/σ_{CO}) (bottom left), CO dispersion (bottom right) and HI dispersion (top right) maps of NGC 7331. The colourmap values of the dispersion plots are in units of km s^{-1}.

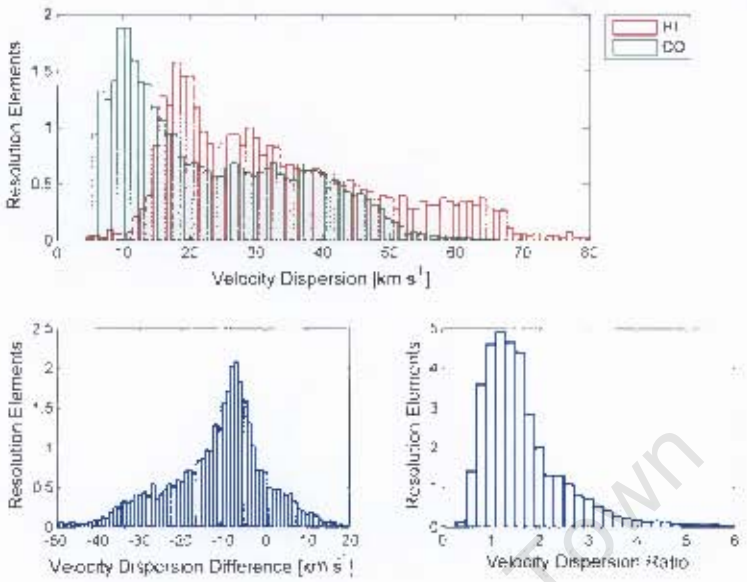

Figure A46: (Top) Distributions of the HI and CO dispersions for NGC 7331. Lower Left and Right figures are plots of the dispersion difference $\sigma_{CO} - \sigma_{HI}$ and dispersion ratio σ_{HI}/σ_{CO} in NGC 7331

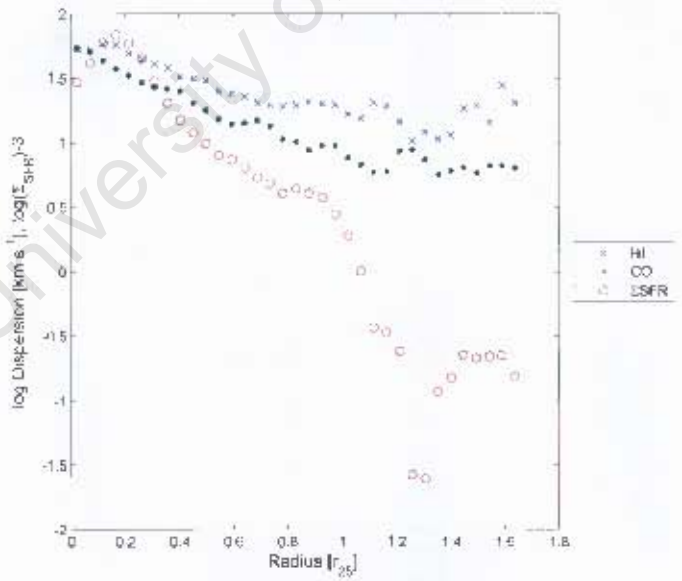

Figure A47: The radially smoothed log CO and log HI dispersions and the log star formation rate density in NGC 7331 versus the radius (in r_{25}). Smoothing was done in annuli of width 13". Log dispersions are plotted and log star formation rate density −3 is plotted (with Σ_{SFR} in the units : [$M_\odot$ Myr^{-1} kpc^{-1}]).